

DISSERTATION

TABLE-TOP, FULL-FIELD, ACTINIC MICROSCOPE FOR EXTREME
ULTRAVIOLET LITHOGRAPHY MASK CHARACTERIZATION

Submitted by

Fernando Brizuela

Electrical and Computer Engineering

In partial fulfillment of the requirements

For the Degree of Doctor in Philosophy

Colorado State University

Fort Collins, Colorado

Fall 2010

COLORADO STATE UNIVERISTY

August 3rd, 2010

WE HEREBY RECOMMEND THAT THE DISSERTATION PREPARED UNDER OUR SUPERVISION BY FERNANDO BRIZUELA ENTITLED TABLE-TOP, FULL-FIELD, ACTINIC MICROSCOPE FOR EXTREME ULTRAVIOLET LITHOGRAPHY MASK CHARACTERIZATION BE ACCEPTED AS FULFILLING IN PART REQUIREMENTS FOR THE DEGREE OF DOCTOR OF PHILOSOPHY.

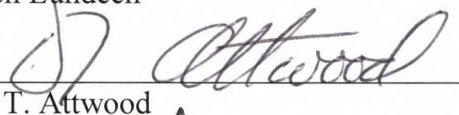
Committee on Graduate Work



Mario C. Marconi



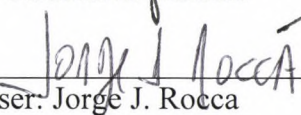
Stephen Lundeen



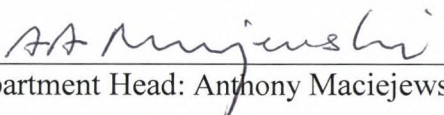
David T. Attwood



Adviser: Carmen S. Menoni



Co-Adviser: Jorge J. Rocca



Department Head: Anthony Maciejewski

ABSTRACT OF DISSERTATION

TABLE-TOP, FULL-FIELD, ACTINIC MICROSCOPE FOR EXTREME ULTRAVIOLET LITHOGRAPHY MASK CHARACTERIZATION

The development of increasingly smaller, faster, and more complex electronic devices that significantly impact everyday life is driven by the ability of printing smaller and smaller components onto semiconductor chips. The number of transistors printed onto an integrated circuit has increased from about one thousand in the 1970 to over a billion in recent years. This exponential growth has been possible thanks to great advances in microlithography processing, and is expected to continue with the implementation of Extreme Ultraviolet Lithography (EUVL) for the printing of the next generation of semiconductor chips.

Although EUVL is conceptually similar to conventional lithography in that a mask is projected onto the wafer with a set demagnification, the unique characteristics of extreme ultraviolet light have generated a myriad of technological challenges in the development of this new lithographic technique, including the availability of bright sources, photoresists, reflective optics, and metrology tools at these wavelengths.

Of these challenges, the need for microscopes capable of characterizing the printability of absorber patterns on the reflective Mo/Si coated lithographic masks, has

risen be to one of the highest priorities for chip manufacturers as they prepare to implement EUVL at high-volume manufacturing.

Currently, only a very limited number of EUV microscopes for mask characterization are available. And although these few synchrotron-based microscopes have significantly contributed to the development of EUVL masks, their building-size illumination source make them unsuited for mask characterization in an industrial setting.

This dissertation describes the development of the first compact, full-field microscope for at-wavelength characterization of EUVL masks. This microscope combines the output of a table-top 13.2 nm wavelength laser with state-of-the-art diffractive optics to render high quality images of the patterns on EUVL masks with 55 nm spatial resolution and acquisition times of less than 90 seconds. From these images we have demonstrated for the first time measurements of line-edge roughness and normalized intensity line slope of an EUVL mask using a compact microscope. This is significant because with this microscope that emulates the imaging conditions of a 4 \times -demagnification stepper it is possible to evaluate the mask quality and printability independently of photoresist response.

It is foreseeable that these microscopes will not only contribute to the development of EUVL mask technology, but will also play a significant role in the path for the realization of convenient stand-alone metrology systems for on-site evaluation of EUVL masks.

Fernando Brizuela
Department of Electrical and Computer Engineering
Colorado State University
Fort Collins, CO 80523
Fall 2010

ACKNOWLEDGEMENTS

I would like to express my gratitude to my advisers Professor Carmen S. Menoni and Professor Jorge Rocca for giving me the opportunity of working in their research group.

I would also like to acknowledge Professor Stephen Lundeen, Professor Mario Marconi, and Professor David Attwood for serving on my committee. I appreciate their thorough review of this dissertation and their insightful comments.

This work presented herein would not have been possible without the support from the National Science Foundation Engineering Research Center for Extreme Ultraviolet Science and Technology under NSF Award No. 0310717.

The imaging group has counted with a number of talented people over the years that have contributed not only to the project but to my growth through grad school. Many thanks to the people at Berkeley with whom I've had the privilege of working, specially Weilun Chao, Yanwei Liu, Erik Andersen, Anne Sakdinawat, Iacopo Mochi, and Kenneth Goldberg.

At Colorado State University I started working on this project with Georgiy Vaschenko and Courtney Brewer. Not only did we work our way through the development of the first microscopes but also shared many, many philosophical talks. Those talks have been replaced by grammar challenges with Sergio Carbajo who will,

with no doubt, continue with the great imaging research of our group and enjoy being boss. I cannot thank them enough for making going to work every day so enjoyable.

I also want to thank all the people that work so hard in the development of the lasers and with whom the imaging projects would not have been possible: Mike Grisham, Dale Martz, Miguel Larotonda, Scott Heinbuch, Yong Wang, David Alessi, Francesco Pedaci, and Brad Luther.

Everyone at the ERC has made my passage through grad school extremely enjoyable. I can't thank you all enough.

Finally I'd like to thank my friends and family for their constant support. I dedicate this dissertation to my wife Luciana and son Federico, the most important people in my life who every day teach me so much and remind me what a wonderful life we have.

TABLE OF CONTENTS

1.1. Introduction.....	3
1.2. EUV full-field microscopes	5
1.3. Optics for EUV/SXR microscopy.....	16
1.4. Spatial resolution with partially coherent illumination.....	19
1.5. Determination of the partial coherence of the illumination.....	26
1.4. Scope of this Dissertation	29
2.1. Introduction.....	31
2.2. Extreme ultraviolet lithography steppers.....	35
2.3. Types of defects on EUVL masks	38
2.4. Metrology tools for extreme ultraviolet lithographic masks	40
2.4.1 Scanning mask inspection microscopes.....	44
2.4.2 Aerial image microscopes.....	48
2.5 Pattern characterization from EUV images	52
3.1. Introduction.....	55
3.2. Table-top EUV-AIM: microscope setup.....	56
3.3. Table-top EUV-AIM: description of the 13.2 nm wavelength laser illumination.	59
3.4. Table-top EUV-AIM: description of the microscope's optics.....	64
3.5. Table-top EUV-AIM: description of the EUV mask samples.....	67
3.6. Table-top EUV AIM: microscope operation	70

3.6.1. Suitability of 13.2 nm radiation for EUVL mask characterization.....	71
3.6.2. Photon budget for image acquisition.	74
3.6.3. Procedure for microscope alignment	76
<u>CHAPTER 4: Results</u>	82
4.1. Introduction.....	82
4.2. Characterization of the microscope	83
4.2.1. Resolution measurements	83
4.2.2. Illumination and coherence characterization of the microscope.....	89
4.3. EUV image analysis for the characterization of patterns	93
<u>CHAPTER 5: Summary and future work.....</u>	96
<u>CHAPTER 6: Papers and presentations</u>	103
<u>Peer-reviewed publications</u>	103
<u>Science news articles</u>	104
<u>Press release articles</u>	104
<u>Conference abstracts or proceedings</u>	105
<u>CHAPTER 7: References</u>	111

CHAPTER 1: Extreme Ultraviolet Microscopy

1.1. Introduction

Extreme ultraviolet (EUV) microscopy has established itself as an important research tool across a variety of fields in the physical and life sciences. EUV microscopes are similar to their visible light-based counterparts, but instead of visible light ($\lambda \sim 500$ nm) they employ radiation in the soft x-ray (SXR) and EUV regions of the electromagnetic spectrum ($1 \text{ nm} < \lambda < 10 \text{ nm}$ and $10 \text{ nm} < \lambda < 50 \text{ nm}$, respectively) for illumination (Fig. 1.1). By exploiting the linear dependence of spatial resolution with illumination wavelength, these photon-based microscopes can render images of structures in the 10 nm range, almost two orders of magnitude smaller than the features observable with a conventional compound microscope [1].

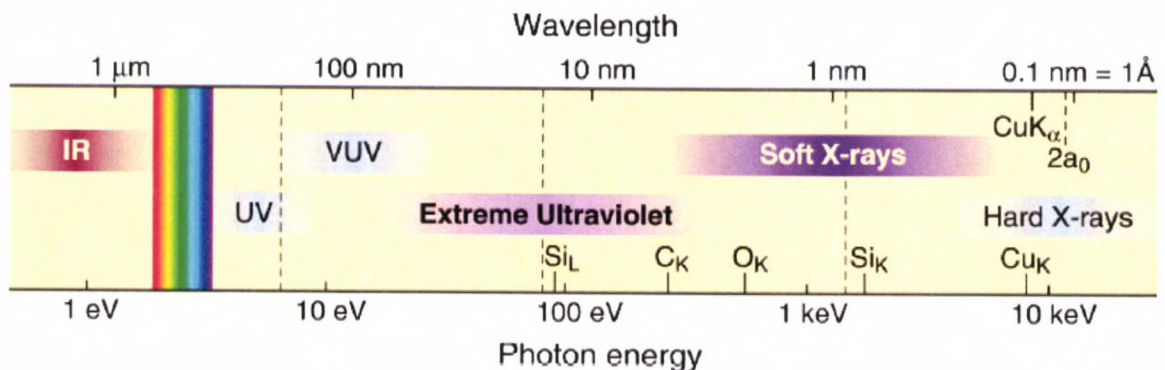


Figure 1.1: Electromagnetic spectrum from infrared to hard x-rays. Radiation in the region of extreme ultraviolet and soft x-ray is well suited for high resolution imaging (figure from [1]).

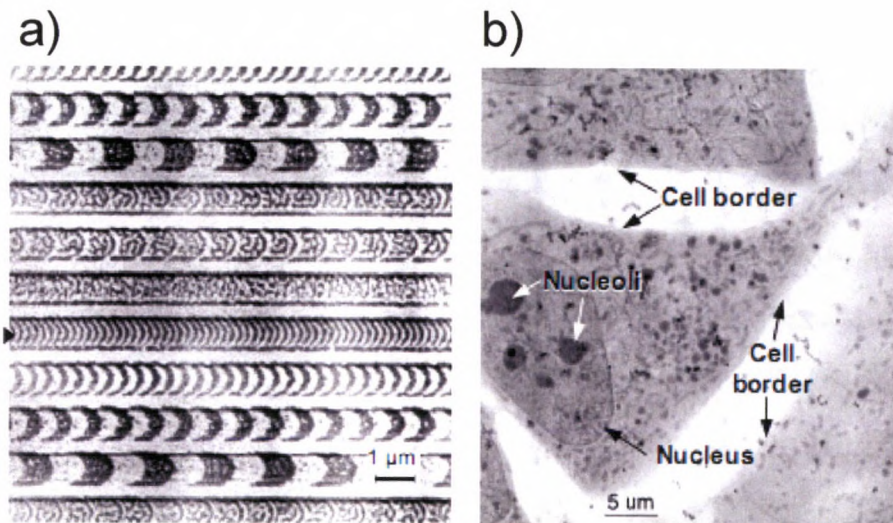


Figure 1.2: EUV images of a) magnetic domains and b) a yeast cell obtained using EUV microscopes (images from [1]).

Extreme ultraviolet microscopes are currently used in a variety of research efforts ranging from material science; for example in the study of magnetic materials or chemical composition of cement, to biology, where high resolution images of cryo-fixed cells allow the study of cell structures [2-10]. These studies not only take advantage of the improved spatial resolution imparted by these microscopes but also exploit the natural contrast that arises from the absorption edges that materials present in this region of the electromagnetic spectrum. In this way, for example, magnetic domains of a single element in a multi-component system can be imaged at the nanometer scale [2]. Also, by imaging at wavelengths between the carbon and oxygen absorption edges, images of biological samples can be obtained with high contrast between water and proteins. If these images are at different planes in the sample, a topographic image of cells can be obtained in which the sub-cell structures can be observed [8, 10]. Figure 1.2 shows some

examples of images of materials and biological systems obtained with SXR/EUV microscopes.

These examples illustrate how, by carefully selecting the wavelength of illumination and the geometry of the optical system, these microscopes can be tailored to address a diversity of scientific and technological problems. The next section presents the different modalities of EUV imaging that are currently available and several examples of imaging using different microscope systems.

1.2. EUV full-field microscopes

Extreme ultraviolet and soft x-ray microscopy are the natural extension of optical microscopes towards higher spatial resolution. The development of high brightness sources of EUV and soft x-ray light accompanied by an equally important development in optics for this region of the electromagnetic spectrum has allowed great progress in the field of optical imaging through a number of specialized microscopes.

Apart from improvement in spatial resolution, there is a second and equally important reason for the development of EUV microscopes. In this region of the electromagnetic spectrum, strong interactions exist between the photons and atoms, providing a natural absorption contrast between different elements. A typical example of this contrast mechanism is the one that exists between oxygen rich water and carbon rich proteins at ~ 3 nm wavelength (Fig. 1.3).

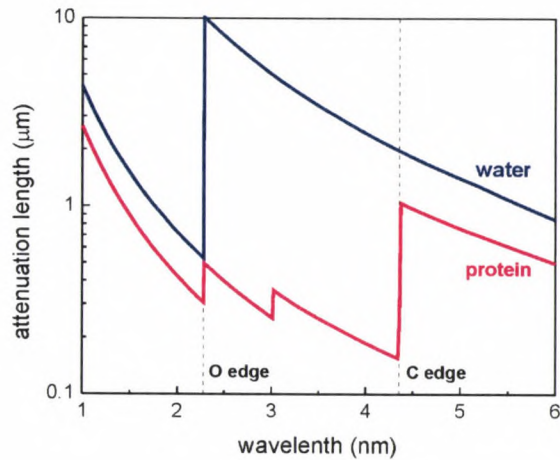


Figure 1.3: Absorption length as a function of wavelength for water and proteins. High contrast between water and proteins can be obtained by imaging with wavelengths between the O absorption edge (2.28 nm) and the C absorption edge (4.36 nm). (data from www-cxro.lbl.gov).

By imaging at wavelengths between the oxygen K absorption edge at 2.28 nm and the carbon K absorption edge at 4.37 nm, it is possible to maximize the contrast between biological tissue and surrounding water. This region of the electromagnetic spectrum is known as the “water window” and it is at these wavelengths that soft-x-ray microscopes for biological imaging operate [1, 3, 8, 9].

As with visible light imaging, several EUV microscopy modalities exist, the most common being scanning microscopy and full-field microscopy. Scanning EUV microscopes generate images by recording the local transmission or reflection of a sample pixel by pixel. In this geometry, the illumination light is focused onto a small area of the sample which, along with the step size of the translation stages, determines the resolution of the image. The light reflected or transmitted by the sample is collected

using a photodiode which records an intensity value for each position. A diagram of the setup of a scanning EUV microscope is shown in Fig. 1.4.

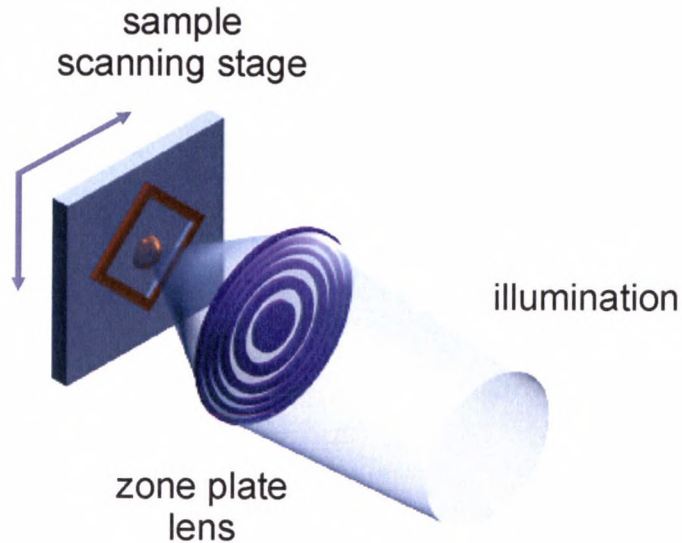


Figure 1.4: Setup of a scanning EUV microscope. The sample is scanned across the focused illumination and the transmitted intensities are recorded to form an image.

Full-field or aerial imaging microscopes use a lens to project a magnified version of an object's illuminated region onto the image plane. Their setup is similar to that of a visible compound microscope. A lens, or a series of optical elements, is used to gather the light onto the sample. The light transmitted through the sample is collected by an objective that projects the image onto a detector. The setup of a typical full-field EUV microscope is shown in Fig. 1.5. This type of EUV microscope was first developed at The Deutsches Elektronen-Synchrotron (DESY) in Hamburg by Niemann, Rudolph, Schmahl, and collaborators to image biological samples in the water window [11, 12].

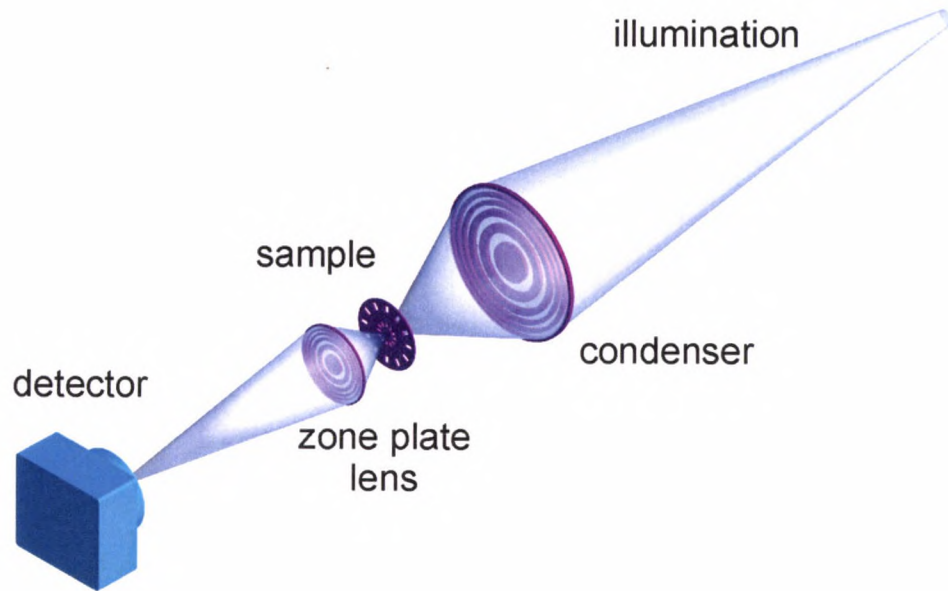


Figure 1.5: Setup of a full-field EUV microscope. A zone plate objective collects the light transmitted through the sample and projects the image onto a CCD device.

Compared to scanning microscopes, full-field microscopes can record an entire image in a shorter amount of time, with a resolution limited by the objective lens and illumination conditions but not the translation stage.

As seen in both cases, the main components of any microscope are the illumination source and the optics employed to manipulate the light. At EUV wavelengths, the selection of the source is particularly important since a limited number of sources exist with sufficient flux for imaging applications.

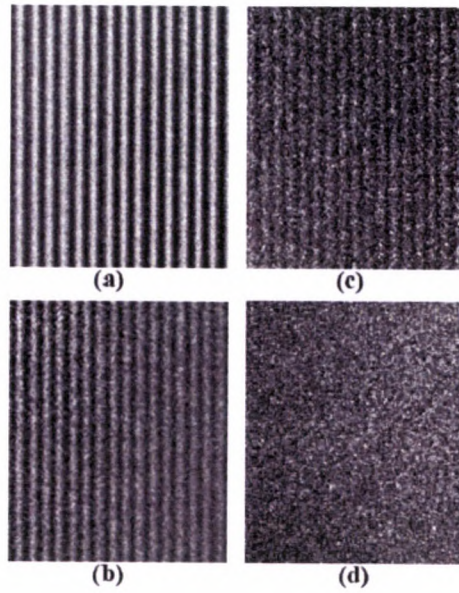


Figure 1.6: Soft x-ray images of Mo/Si test patterns obtained with a 12 nm micro zone plate at 1.75 nm wavelength (707eV). The patterns have half-pitch values of (a) 20 nm, (b) 15 nm, (c) 12 nm, and (d) 10 nm. the lines and spaces can be clearly seen down to 12 nm half-pitch (figure and caption from [13]).

Synchrotrons are widely used and so far have produced the best results in terms of spatial resolution. These sources have several characteristics that make them well suited for imaging. They have high brightness and are tunable over a broad range of wavelengths. Weilun Chao *et al.* at the Advanced Light Source in Berkeley hold the record for spatial resolution [13, 14]. They have achieved a spatial resolution of 12 nm using 1.75 nm radiation in combination with state-of-the-art micro zone plates with outer zones of 12 nm [13]. Figure 1.6 shows images of Mo/Si test patterns of different half-pitch values obtained with this system where the 12 nm lines of Fig. 1.6(c) can be clearly observed.

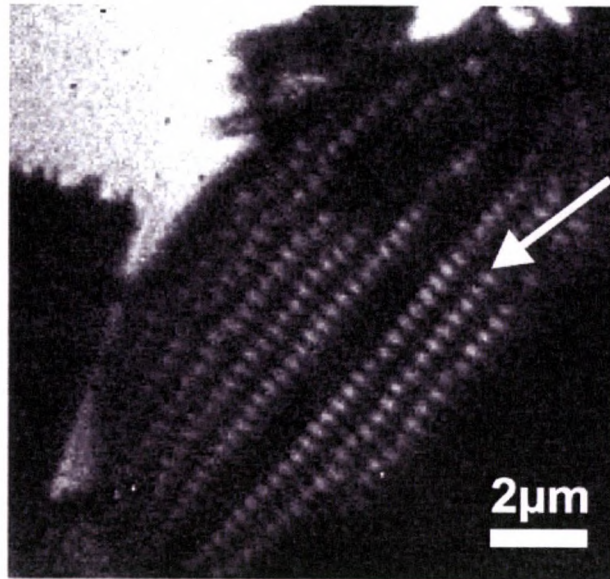


Figure 1.7: EUV image of a diatom using an HHG-based full-field microscope. The image has a spatial resolution of 200 nm as measured from the features indicated by the arrow (image from [15]).

The significant developments in EUV/SXR full-field microscopy using synchrotron illumination have in the last few years been paralleled by the demonstration of microscopes based on laboratory-size sources of EUV wavelength light. Table-top EUV/SXR sources have the advantage of being orders of magnitude smaller while, in the case of EUV lasers, offering comparable spectral brightness. These table-top sources allow EUV/SXR microscopy to be implemented in-house rather than having to take samples to synchrotron facilities. They are also less expensive. Laboratory-size EUV/SXR sources that have been used for microscopy include plasma-based sources, high harmonics and soft x-ray and EUV lasers [15-22].

Full-field imaging using High Harmonic Generation (HHG) was demonstrated in an all-mirror setup with a spatial resolution of a few microns [16]. Also, using 13.6 nm HHG in combination with multilayer coated mirrors and a 100 nm outer zone width zone

plate objective, images of diatoms with a spatial resolution of 200 nm were obtained [15, 22] (Fig. 1.7). More recently, a higher spatial resolution was achieved by Kim *et al.* also using an HHG source at ~ 13 nm [23]. In this case, grating structures with half-pitch values down to 160 nm were observed and a spatial resolution of 130 nm was obtained by analyzing the intensity transition along the imaged features.

Laser plasma-based incoherent EUV sources have also been successfully used in full-field imaging systems. Trail *et al.* achieved 0.5 μm resolution with a 14 nm source in scanning mode using a Schwarzschild as the focusing optics [17]. A full-field microscope based on a Schwarzschild condenser and a laser plasma x-ray source operating at 20 nm wavelength achieved a spatial resolution of ~ 0.2 μm [24].

Sub-100 nm resolution was also achieved in the water window ($\lambda = 2.3\text{-}4.4$ nm), where biological samples can be studied [18, 20]. In these experiments, the setup consisted of a 100 Hz table-top regenerative debris-free droplet-target x-ray source emitting at 3.37 nm in combination with a normal-incidence multilayer condenser and a 30 nm outer zone width zone plate. An image of a diatom obtained with this setup is shown in Fig. 1.8.a. More recently, a record spatial resolution of 25 nm was achieved using this incoherent EUV source and a novel compound zone plate [25]. An image of a resolved 25 nm half-pitch gold grating obtained with this system is shown in Fig. 1.8.b.

The use of SXR and EUV lasers as illumination sources has also been explored. An advantage of using lasers is that they produce highly directional and monochromatic beams, significantly reducing exposure times. Lasers also emit light in short pulses, which would allow for time-resolved imaging of fast reversible processes. The difference between imaging with lasers compared to incoherent sources is that the

coherence of the beam can degrade the quality of the image. However, in some lasers the coherence can be adjusted and in others the degree of coherence is relatively low [26].

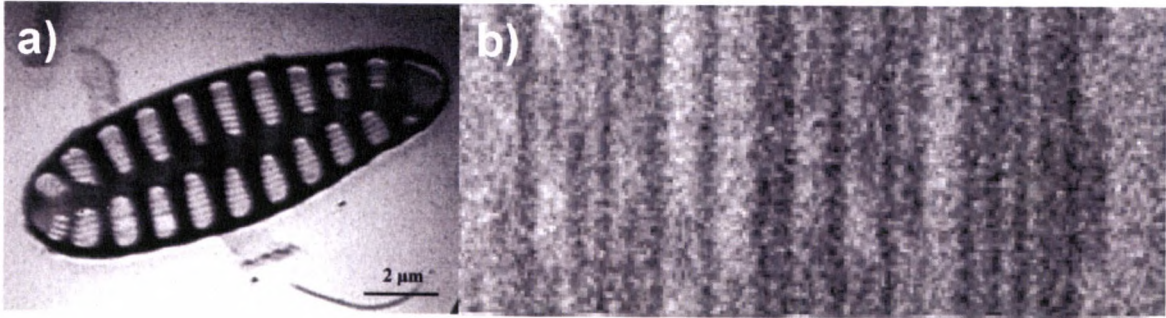


Figure 1.8: a) SXR image of a diatom obtained using a plasma source in combination with multilayer coated mirrors and a 30 nm outermost zone width zone plate (from [3]). SXR image of a 25 nm half-pitch gold grating obtained with a compound zone plate objective (images from [25]).

The earliest imaging experiments with soft x-ray lasers were done in 1992 by two different groups. A spatial resolution of 75 nm was reported by Da Silva *et al.* using a 4.48 nm tantalum x-ray laser pumped by NOVA in combination with a multilayer condenser mirror and a 45 nm outer zone width objective zone plate [19]. In the same year, DiCicco *et al.* reported a spatial resolution of 0.7 μm using a soft x-ray laser operating at 18.2 nm, an ellipsoidal mirror condenser, and a Schwarzschild objective in a proof of principle experiment, not set up for high resolution [27].

More recently, Kishimoto *et al.* reported in 2003 that 200 nm resolution was achieved with single shots from a 13.9 nm Ni-like Ag laser in combination with a Schwarzschild condenser and a objective zone plate with a 100 nm outer zone width [21] (Fig. 1.9). The images however were not of high quality.

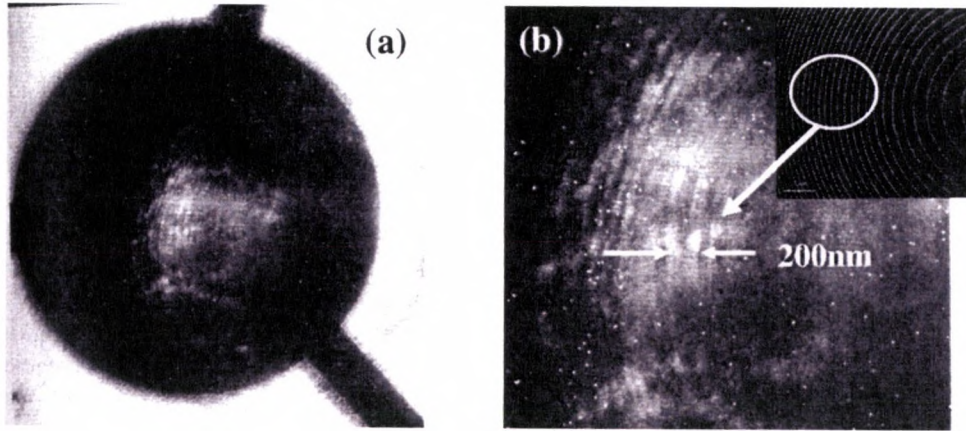


Figure 1.9: Zone structure of zone plate obtained with soft x-ray microscope (picture and caption from [21]).

Reflection mode imaging allows for the study of surfaces and non-transmitting samples. However, imaging with EUV light in this mode presents several difficulties. The reflectivity of materials at small angles of incidence is very low [28]. As shown in Fig. 1.10, only at angles above 70 degrees does the reflectivity become substantial, i.e. greater than $\sim 30\%$. Also, the contrast between different materials is low. For this reason, little progress has been made in terms of reflection mode imaging using EUV and soft x-ray light. Nevertheless, over a decade ago a proof of principle experiment was done to show that reflection mode imaging was possible using 18.2 nm radiation from an x-ray laser [27]. The experiment was done with the laser beam at an incidence angle of 70 degrees with respect to normal to ensure sufficient reflectivity from the gold-patterned sample.

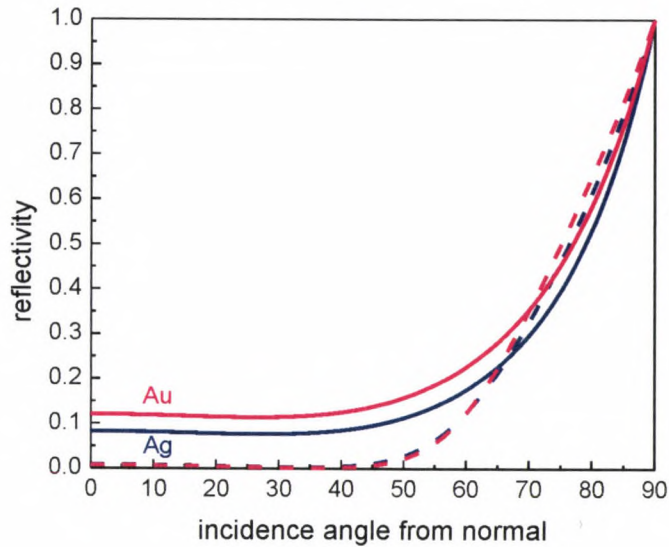


Figure 1.10: Reflectivity curves for gold (red) and silver (blue) surfaces as a function of angle of incidence. Solid line: 47 nm wavelength; dash line: 13.5 nm wavelength (data from www-cxro.lbl.gov).

At Colorado State University, several full-field microscopes have been demonstrated using table-top EUV lasers developed in-house [29-32]. Using a very compact microscope illuminated by an EUV laser emitting at 46.9 nm wavelength, a near-wavelength resolution of 50 nm was achieved with single laser shot exposure in transmission mode [29]. The same system has been demonstrated in reflection mode with measured spatial resolution better than 200 nm [30]. Images obtained with the 46.9 nm wavelength microscope are presented in Fig. 1.11. Figure 1.11(a) shows an entanglement of 50 nm wide carbon nanotubes on a 100 nm thick Si membrane imaged in transmission mode using a single laser shot. In Fig. 1.11(b) a surface of a partially processed semiconductor chip imaged in reflection mode is shown. The dense grating of polysilicon lines silicon in the top region of the image has a half-pitch of 250 nm. The bottom grating is made of 100 nm lines separated by 800 nm spaces.

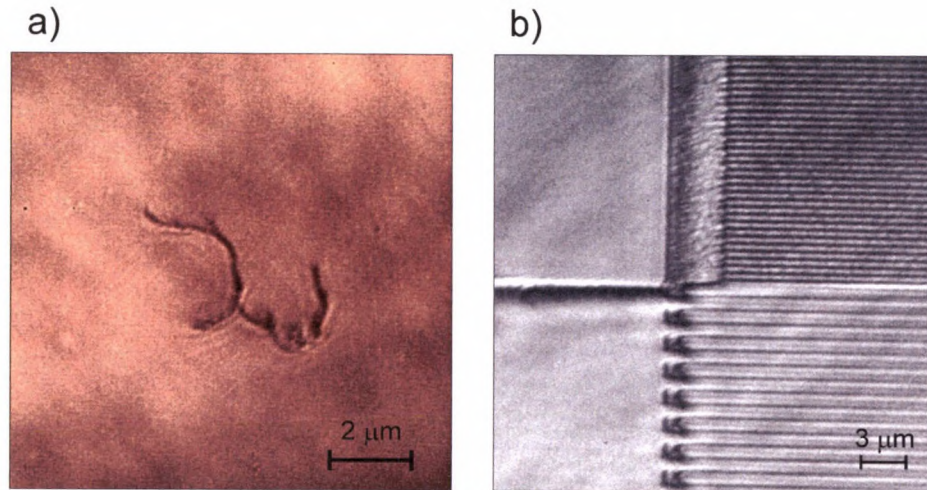


Figure 1.11: EUV images obtained with a 46.9 nm wavelength laser-based, full-field microscope developed at Colorado State University. a) 50 nm wide carbon nanotubes on a 100 nm thick Si membrane imaged in transmission mode and b) partially processed semiconductor chip imaged in reflection mode.

Also at Colorado State University, a full-field transmission mode microscope was demonstrated using an EUV laser emitting at either 13.2 nm or 13.9 nm [31]. Using this system, a spatial resolution of 38 nm was obtained with exposure times of 20 seconds and the laser operating at 5 Hz. An image of a fully resolved transmission grating of 50 nm half-pitch is shown in Fig. 1.12.a. The image was obtained with an exposure time of 20 seconds. An EUV image of 38 nm half-pitch grating is shown in the insert of Fig. 1.12.b. The measured 60% intensity modulation, shown in the figure, indicates that the lines are fully resolved. This is the highest spatial resolution achieved using an EUV laser-based microscope. These results have enabled the development of the microscope presented in this dissertation. The implementation of this microscope in the challenging reflection mode configuration and its application for the specific goal of at-wavelength characterization of extreme ultraviolet lithography masks is covered in Chapters 3 and 4.

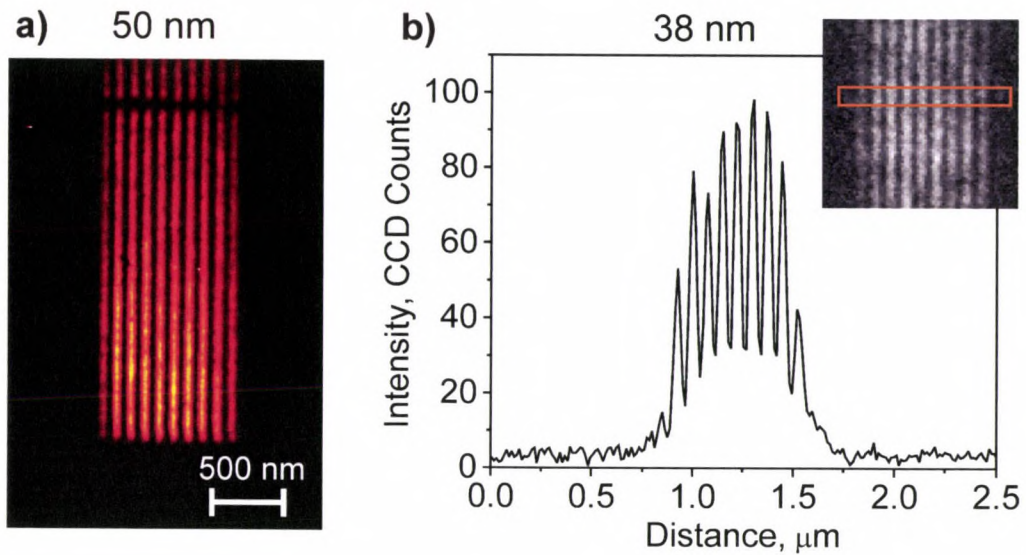


Figure 1.12: EUV images obtained with a 13 nm laser-based, full-field, transmission mode microscope developed at Colorado State University. a) 50 nm half pitch transmission grating and b) intensity cross-section of a 38 nm half-pitch grating. The high modulation indicates that the lines are fully resolved.

1.3. Optics for EUV/SXR microscopy

Besides the illumination source, the other main components of a full-field microscope are the optics employed to illuminate the sample and form the image. There are several ways in which light can be redirected to aid the image formation process: diffraction, reflection, and refraction. The most commonly used methods in visible microscopes are refraction and reflection. In the EUV and soft x-ray region of the electromagnetic spectrum however, most materials show strong absorption, making it necessary to use reflection or diffraction to successfully redirect the light. Furthermore, reflection of simple substrates is only efficient at grazing incidence angles, a geometry that is not

desirable since it introduces aberrations in the image. Diffractive optics and multilayer coated reflective optics provide a good solution for beam manipulation in this region of the electromagnetic spectrum.

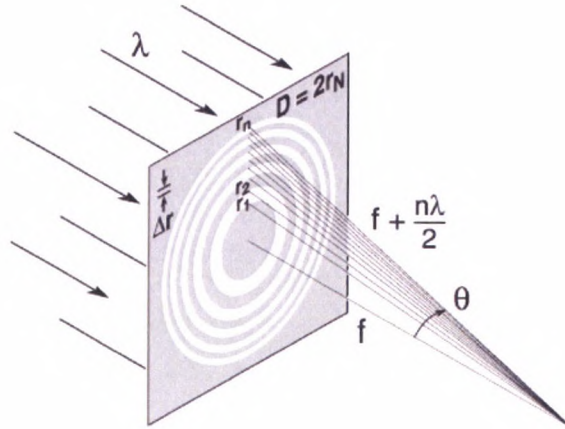


Figure 1.13: Fresnel zone plate lens with plane wave illumination, showing only the convergent 1st order of diffraction. Sequential zones of radius r_n are specified such that the incremental path length of the focal point is $n\lambda/2$. Alternate zones are opaque in the simple transmission zone plate (figure from [1]).

High resolution images in a full-field EUV microscope can be obtained using a zone plate objective. A zone plate is a circular diffraction grating of alternating transparent and opaque zones with a radial variation in pitch as shown in Fig. 1.13. This unique geometry allows for a fraction of the light incident on the lens to focus into real focal spots given by the different diffraction orders. Typically the 1st order is the one employed for focusing and imaging. Relatively low diffraction efficiencies and strong absorption at EUV wavelengths greatly limit the amount of light focused by the lens. If completely absorptive opaque zones and completely transparent openings are considered, the light impinging on the zone plate is distributed as follows: 50% is absorbed by the

opaque zones; 25% is transmitted undiffracted through the lens in the 0th order; 10% of the light is focused into the 1st order; 10% goes to the -1st order; and the remaining 5% is distributed into the positive and negative higher orders. The amount of light transmitted into each order is further reduced by any absorption of the supporting membrane of the zone plate, which can be about 50% for typical 100 nm thick silicon nitride membranes at 13.2 nm wavelength.

The formulae that characterize a zone plate are summarized in Table 1.1. The main parameters of a zone plate can be found by specifying the wavelength of the illumination (λ), the width of the outer most zone (Δr), and the number of zones (N).

radius of nth zone	$r_n^2 = n\lambda f + \frac{n^2\lambda^2}{4}$
diameter of zone plate	$D = 4N\Delta r$
focal length	$f = \frac{D\Delta r}{\lambda}$
numerical aperture	$NA = \frac{\lambda}{2\Delta r}$
depth of focus	$DOF = \pm \frac{1}{2} \frac{\lambda}{(NA)^2} = \pm \frac{2(\Delta r)^2}{\lambda}$

Table 1.1: Focusing properties formulae for the first diffraction order of a Fresnel zone plate. The properties of a zone plate are fully characterized given the diameter of the lens, the width of the outermost zone, and the wavelength of the illumination.

The microscope described in this thesis employs a zone plate condenser and a specialized zone plate objective to obtain full-field images of the surface of EUVL masks. The design and parameters of these optics will be covered in Chapter 3. The

selection of the optics is critical in ensuring high photon throughput as well as for minimizing aberrations and providing high spatial resolution. This selection also plays a significant roll in the quality of the resulting images since the optics can modify the spatial coherence properties of the imaging system. The relationship between spatial resolution and illumination coherence will be discussed in the next section.

1.4. Spatial resolution with partially coherent illumination

The coherence properties of the illumination of a microscope have a pronounced effect on the fidelity of the resulting magnified image. In an ideal case, a microscope would reproduce an exact copy of the object in the image plane, modified only by the magnification factor. One can think of a microscope as a transmission line in which information is transferred from the object plane to the image plane in the form of spatial frequencies. Limitations in physical elements, i.e. lenses, limit the frequencies that can be transmitted, resulting in a blurring of the system. Also, the coherence of the propagating light affects the way the light interacts in the image plane, creating changes in the intensity distribution of the final image.

The formulation for imaging with partial coherence illumination was elaborated by Hopkins [33] in 1952 and extensively discussed by J. Goodman [34] and Born and Wolf [35]. The theory proposes a solution to the propagation of light for image formation that is a generalized case of the well known coherent and incoherent cases. The theory derives the intensity distribution at the image plane as the propagation of the

mutual intensity at the object plane through an imaging system and is expressed in terms of the coherence function in the object plane (i.e. coherence length of the illumination at the object plane, l_{coh}), the diffraction distribution function of the imaging system (i.e. point spread function of the objective lens, PSF_{obj}), and a function describing the structure of the object.

For the limiting cases of coherent and incoherent illumination, analytical solutions exist in which one finds that imaging is linear in amplitude and in intensity respectively. However, in the general case where the illumination of the sample is partially coherent, numerical methods must be employed to calculate the intensity in the image plane. A computer program named SPLAT (Simulation and Projection Lens Aberrations via TCCs) uses this generalized theory to calculate the image intensity pattern from the Fourier transform of a transmission mask [36]. The inputs necessary to perform the simulation are the illumination (in terms of the coherence parameter m and the illumination wavelength), the characteristics of the sample (dimensions and transmission of the different features), and the numerical aperture of the objective lens.

Using this program, images of a simple pattern were simulated under different coherence conditions as shown in Fig. 1.14. The object imaged is shown in Fig. 1.14.a. It consists of a 250 nm transmissive square centered on a thin cross. The object was imaged with 13.5 nm light and an objective numerical aperture of $\text{NA}=0.28$. The resulting image for coherent illumination ($m=0$) is shown in Fig. 1.14.b while Fig. 1.14.c corresponds to the incoherent case ($m>1$).

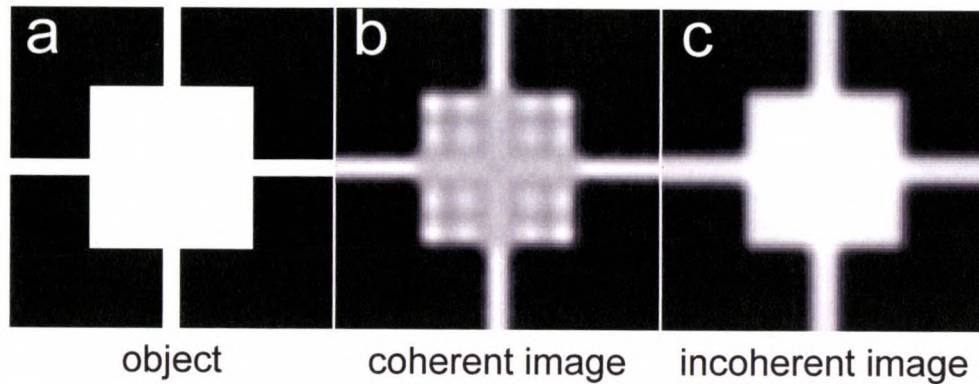


Figure 1.14: Simulated images using SPLAT: a) transmission object, b) coherent image ($m=0$), and c) incoherent image ($m=1$).

The image of the coherent case shows diffraction and interference effects affecting the uniformity of the intensity, especially in the large square. At the other end, the incoherent image shows a more uniform intensity but a wider spread across the thin lines. This example illustrates how the amount of spatial coherence affects the sharpness of the features, or spatial resolution, of an image.

The spatial resolution of a microscope is the size of the smallest feature on a sample which the system can clearly reproduce. This definition is fairly ambiguous because it lacks a measure based on basic principles. Hence, several criteria are currently used to characterize the performance of optical systems. Of these, the Rayleigh resolution criterion is the most widely referenced throughout the literature.

The intensity distribution of the image of a small object is called the point spread function (PSF). For the case of a point source, the PSF corresponds to an Airy pattern that originates from the intersection of spherical waves with the image plane. According to the Rayleigh resolution criterion, the mutually incoherent Airy patterns of two point sources are just resolved when the first null of one overlaps the peak of the other (Fig. 1.15). When this occurs, the corresponding intensity distribution has a modulation of

26.5%. In this case, the resolution limit is then given by the radius at which the first null in the Airy pattern occurs:

$$\Delta r_{Rayl.} = r_{null} = k \frac{\lambda}{NA} \quad (\text{Eq. 1.1})$$

where NA is the numerical aperture of the objective, λ is the wavelength of the light, and k is a dimensionless constant that depends on the coherence of the illumination and the resolution test. This criterion assumes incoherent illumination of the object, for which k takes the value of 0.61. As mentioned above, samples are generally illuminated by partially coherent light. For this reason, a different measure must be used to determine spatial resolution that relates to the Rayleigh criterion but is still valid when imaging with partially coherent illumination.

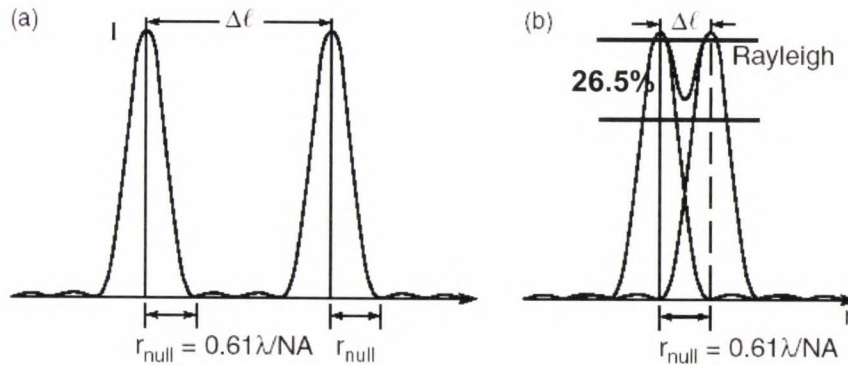


Figure 1.15: Airy intensity patterns due to mutually incoherent, quasi-monochromatic point sources at the image plane of a lens of numerical aperture NA. In (a), the two are well separated and easily resolved. In (b), the two are just resolved by the Rayleigh criterion, corresponding to a intensity modulation of 26.5%. (figure from [37]).

There are three common ways to define resolution for any case of coherence: two-point resolution, knife-edge resolution and grating resolution [38]. All three are based in the Rayleigh criterion for incoherent illumination and are expressed in terms of λ/NA .

The Two-point resolution is defined as the separation d , in λ/NA , at which the modulation of the image of two points is 26.5%. The Knife-edge resolution is taken as the width of the 10% to 90% intensity transition, in λ/NA , of an image of a sharp edge. It relates to the Rayleigh criterion since for totally incoherent illumination the 10% to 90% transition occurs at $k = 0.61$ [38]. Finally, the Grating resolution is defined as the period in λ/NA of the smallest grating for which the modulation intensity is 26.5%. It is also common to express the resolution as the half-pitch of the grating in which case the value of k must be taken as half of the value used for the period. Heck *et al.* [38] have calculated the theoretical resolution as a function of coherence for the three tests described above (Fig. 1.16).

For all three cases, the value of k reaches ~ 0.61 for coherence parameters larger than 1 when the illumination can be considered completely incoherent. However, for lower values of m there is significant difference in the value of k obtained for the different measurements.

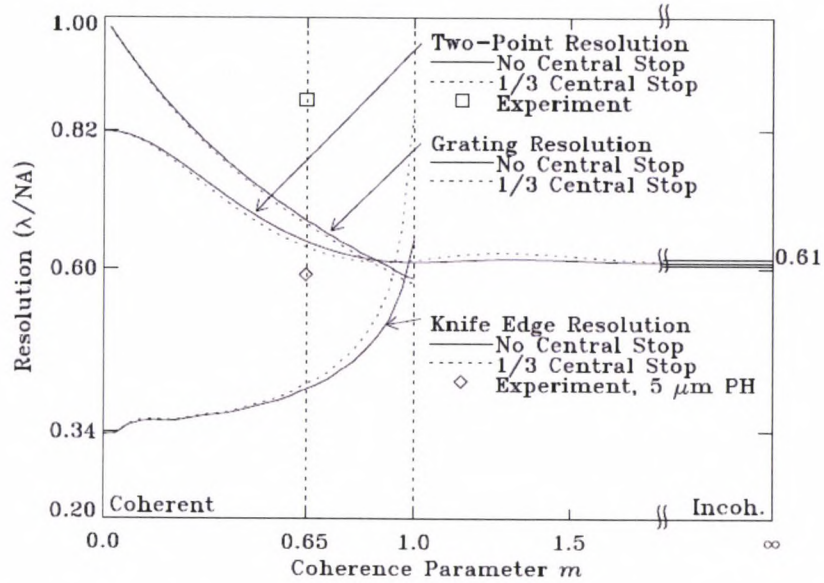


Figure 1.16: Theoretical resolution as a function of coherence, assuming monochromatic illumination. For each case, the dashed and solid lines represent the resolution with and without a central stop in the condenser zone plate, respectively. The diamond and square represent the experimental knife-edge and two-point resolution achieved with the XM-1 microscope at ALS (figure from [38]).

The effect of the parameter k on the spatial resolution of the system can be seen by taking intensity cross-sections along the edges of the simulated images of Fig. 1.14 as shown in Fig. 1.17. The figure shows that although the image obtained under incoherent illumination has better uniformity across the illuminated feature, the 10% to 90 % transition is not as steep as for the coherent illumination case, indicating that the spatial resolution is lower according to the stated criterion. This is in agreement with the plot of Fig 1.16 that indicates that a knife-edge test provides a higher spatial resolution under coherent illumination.

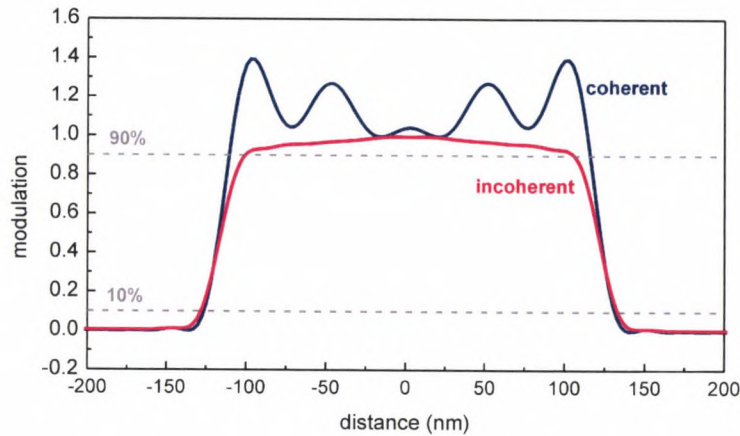


Figure 1.17: Intensity cross section of a knife-edge obtained from Fig. 1.12 for the extreme cases of coherent and incoherent illumination. As the illumination becomes more coherent, the resolution increases if performing a knife-edge test.

Experimentally, the most accurate method for establishing the spatial resolution of the system is using gratings of different periods. In this way, one can obtain not only the value of the spatial resolution of the system but can also obtain the modulation transfer function (MTF) of the system by plotting the maximum intensity modulation values as a function of grating distance or its inverse, the spatial frequencies. Similar measurements could be done using the two-point test; however, because of the small size of the pinholes used, little flux passes through them, significantly reducing the signal-to-noise ratio and compromising the quality of the data. Regarding knife-edge tests, knife edges are simple to manufacture and image. However, as shown in Fig 1.14, strong diffraction effects occur close to the edge when using coherent illumination, making the determination of the 10% to 90% transition harder, especially when the illumination is non-uniform or not very intense. Furthermore, the method does not provide information

to build the MTF. The data presented in Chapter 4 of this dissertation was obtained using a combination of the methods described in this section.

1.5. Determination of the partial coherence of the illumination

The amount of spatial coherence has a profound effect on the resolution of a microscope. Therefore, the characterization of this parameter is of great importance. The spatial coherence of an optical system can be evaluated using the Talbot effect.

The Talbot effect, discovered in the 1830s by H. F. Talbot, is a self-imaging phenomenon in which, under coherent illumination, a periodic pattern produces replicas of itself at known distances [39]. The distance between these 1:1 replicas, the Talbot distance, is given by the period of the grating (p) and the wavelength of the illumination (λ) as:

$$t = 2 \frac{p^2}{\lambda} \quad (\text{Eq. 1.2})$$

At half the Talbot distance, the replica of the grating also appears, but shifted by half a period.

An example of the Talbot effect is shown in Fig. 1.18, where Isoyan et al. used the output of an EUV laser to print replicas 1:1 of a transmissive mask in a non-contact fashion [40]. Fig. 1.18.a is an SEM image of a region of a transmission pattern consisting of an array of 500 nm half pitch elbow structures. The period of the patterns on the mask is 4.845 μm . The mask was illuminated with the 46.9 nm wavelength light of a coherent EUV laser, resulting in a Talbot distance of 1 mm. The intensity distribution at the three

first Talbot planes was recorded using PMMA. Figures 1.18.b through 1.18.c show the resulting high resolution replicas of the mask after developing the PMMA as observed using an atomic force microscope. If the illumination were partially coherent, these replicas would degrade as Talbot planes further from the mask are considered. For incoherent light, no replicas of the mask exist.

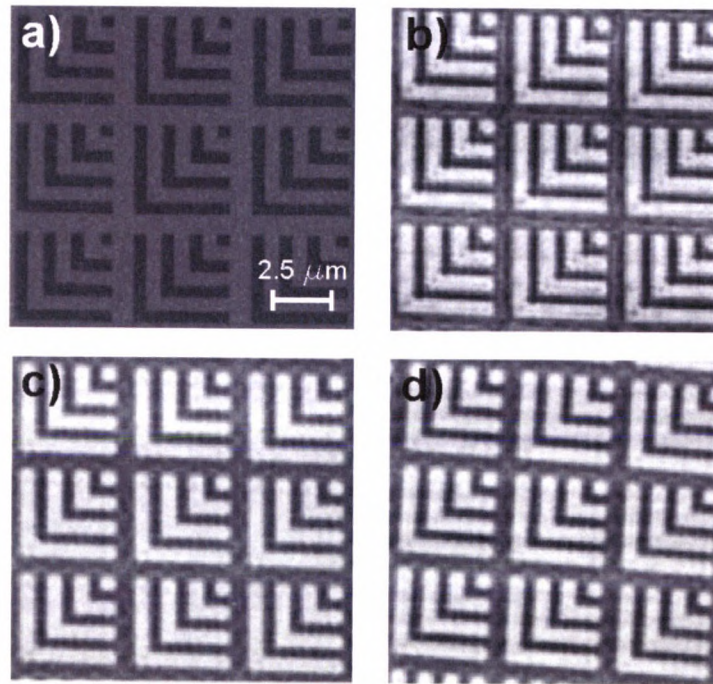


Figure 1.18: a) SEM image of a periodic transmission mask. 1-1 replicas of the mask appear at different planes Talbot planes when illuminated with coherent light. b), c), and d) are the resulting intensity distributions as recorded with PMMA and images with AFM for the first three Talbot planes (from [40]).

The Talbot effect can be used to evaluate the spatial coherence of the imaging system. This is achieved by taking a series of images of a periodic sample at different focal distances. If the through-focus scan is selected such that several Talbot planes around the sample are imaged, the modulation of the intensity in the images reveal the coherence of the microscope. This can be better seen in the plot of Fig. 1.19. This plot

shows through-focus modulation simulations of a 120 nm half-pitch grating imaged with a 0.061 NA objective and 13.2 nm light with different coherence values varying from completely incoherent to completely coherent. The Talbot distance for this grating is $\sim 8.8 \mu\text{m}$. The through-focus scan is $\pm 20 \mu\text{m}$ from the sample, thus including 2 Talbot planes on each side of the mask.

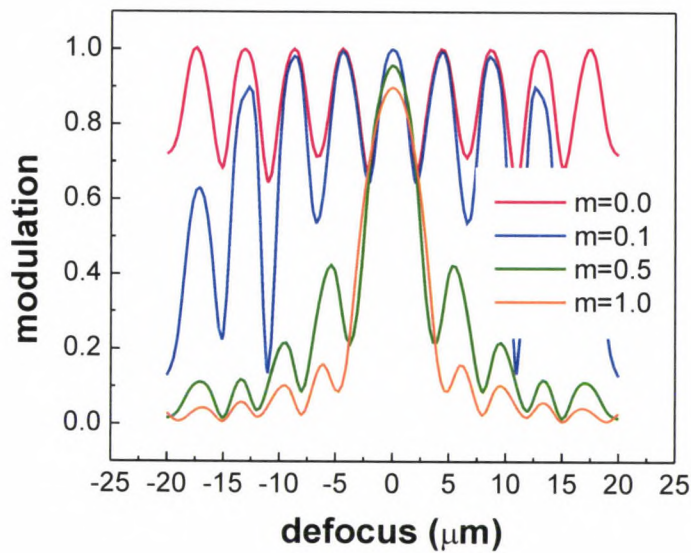


Figure 1.19: Through-focus simulations of a 120 nm half-pitch grating imaged with a 0.061 NA objective and 13.2 nm wavelength light performed using SPLAT [41]. As the coherence of the optical system increases (decrease in m), modulation of out-of-focus maxima increases.

The simulation shows that, for a completely incoherent system ($m=1$), the modulation of the grating has a maximum at the focal plane and decays to zero modulation for out-of-focus planes. As the light becomes more coherent ($m \rightarrow 0$), several secondary modulation maxima appear in out of focus planes. For fully coherent

illumination, the secondary maxima reach full modulation at all half-Talbot and full-Talbot distances.

To obtain an m value for a microscope, measured through-focus data can be compared to simulations performed using the SPLAT simulator in which the spatial coherence can be varied. This approach was employed to measure the spatial coherence parameter of the actinic EUV microscope described in this dissertation and is presented in Chapter 4.

1.4. Scope of this Dissertation

In this dissertation, the development and characterization of a compact, full-field, actinic (at-wavelength) microscope for characterization of extreme ultraviolet lithography (EUVL) masks is described. As will be discussed in the next chapter, the characterization of EUVL masks remains one of the most pressing challenges for the implementation of this new lithographic technique for the printing of the next generation of semiconductor chips at high-volume manufacturing.

The unique aerial image microscope (AIM) presented in this dissertation combines the output of a table-top EUV laser ($\lambda=13.2$ nm) with a zone plate-based optical system to mimic the imaging conditions of a 0.25 NA, 4 \times -demagnification EUVL stepper. This compact microscope provides an excellent alternative to synchrotron-based mask characterization tools since, due to its performance and smaller footprint, it can be employed on site at mask shops and chip-printing facilities.

The performance of this microscope, presented in Chapter 4, parallels that of the best performing synchrotron based systems. Using this microscope, images of EUVL masks with a spatial resolution of 55 nm can be obtained with exposure times as short as 5 seconds. Longer exposures of up to 90 seconds are used to perform critical measurements on EUVL masks, such as the characterization of the quality of the patterns located on the masks.

This dissertation is structured in the following manner. A brief introduction to EUV lithography is presented in Chapter 2 along with different approaches for inspection and characterization the EUVL masks. The design and development of the table-top, full-field, actinic microscope at Colorado State University is covered in Chapter 3, with the characterization of the system and examples of its capabilities presented in Chapter 4. Finally, a summary of the work and a brief discussion on future work are presented in Chapter 5. The work presented here has resulted in the publication of two peer-reviewed articles and in numerous presentations at international conferences. This work builds on the extensive work in the field of EUV microscopy carried out at CSU. A list of the publications and conference proceedings that have resulted from our efforts in advancing EUV microscopy are presented in Chapter 6.

CHAPTER 2: Inspection tools for extreme ultraviolet lithographic masks

2.1. Introduction

Since the 1960s the semiconductor industry has grown into a more than \$250 billion market [42]. The products of this industry have found their way into virtually every human activity, transforming the way we shop, travel, teach, and even spend our leisure time. Common gadgets that people take for granted would not have been possible without the ability to shrink transistors to the nanometer scale. Since 1965, when Gordon Moore first noted that the number of transistors that could be inexpensively placed on an integrated circuit was increasing exponentially, doubling approximately every two years, the semiconductor industry has been pushing to keep this trend. Figure 2.1 shows a plot of the number of transistors per chip for different processors over the last decades. The trend follows Moore's 1965 prediction.

The International Technology Roadmap for Semiconductors (ITRS), implemented by a global consortium of chip manufacturers, equipment suppliers, academic institutions, and government laboratories, annually sets short and long term goals to ensure cost-effective advancements in the performance of integrated circuits and the products that employ such devices [43]. The goals are set in terms of technological half-pitch nodes, which indicate the size or critical dimension (CD) of features on a chip, which translates to the number of transistors printed per unit area.

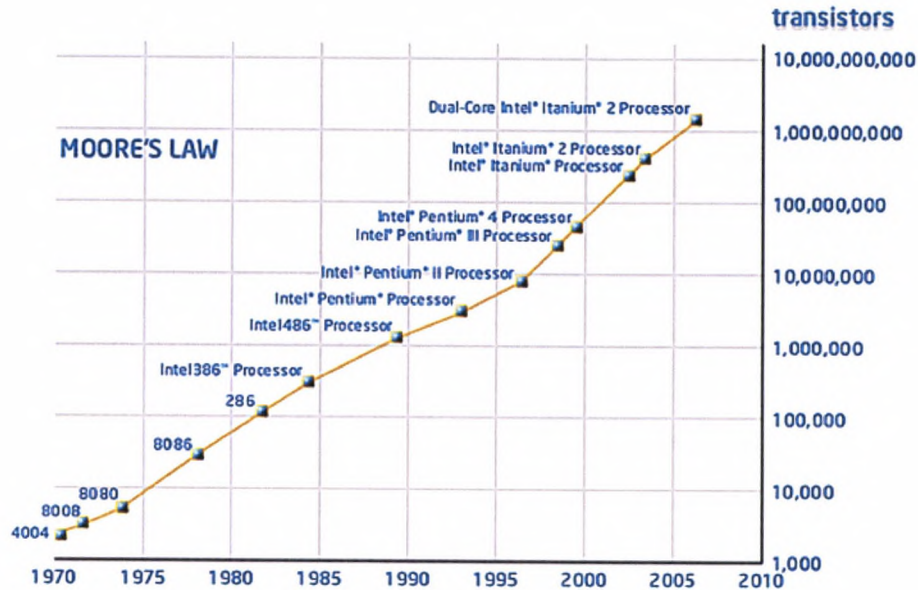


Figure 2.1: Number of transistors per chip for different processors over the last several decades. The trend follows Moore's law, doubling the number of transistors every two years (Figure from web.sfc.keio.ac.jp).

The dominant patterning process used by the semiconductor industry is Reduction Optical Lithography (ROL), in which a reduced image of a mask or reticle is printed directly onto a wafer. In this lithographic method, the minimum printable CD follows a scaling law similar to that of spatial resolution of a microscope: $CD = k\lambda / NA$, being directly proportional to the wavelength of the illumination, λ , and inversely proportional to the numerical aperture, NA , of the printing system being employed; the proportionally constant in this case includes the characteristics of the illumination, the chemistry of the lithographic resist, the development thresholding, etc [43].

Different techniques have been used and are being developed to keep up with the trend set by Moore's law. Lithographic techniques have moved from visible light

towards shorter wavelengths in the deep ultraviolet (deep UV) region of the electromagnetic spectrum by using the 248 nm and 193 nm spectral lines of krypton fluoride and argon fluoride excimer lasers, respectively, for illumination. By using techniques to improve the numerical aperture of the printing systems, such as in immersion lithography ($NA > 1.2$), systems with CD values of less than 50 nm are currently available [43].

All these advances in the optical systems have been accompanied by equally important advances in lithographic photoresist, the medium onto which the patterns are transferred. Nevertheless, to continue beyond the 22 half-pitch technological node, even shorter printing wavelength than the ones currently used will be required.

Over the past decade there has been consensus to develop a lithographic process employing extreme ultraviolet (EUV) light. The availability of highly reflective Mo/Si multilayer-coated mirrors and the potential for generating sufficiently bright EUV sources around 13.5 nm wavelength have set the parameters for EUV lithography (EUVL) [44]. Ideally, during the life-time of a current lithographic technique, the next generation would be developed and optimized to continue improving semiconductor components. However, due to of the difficulty in the generation and control of EUV light, the development of EUV lithography has extended beyond the initial estimations, increasing the pressure for the current 193 nm technology to keep up with the roadmap to achieve smaller printed features.

Meanwhile, great efforts are underway to improve the reliability and throughput of EUVL to the point where high-volume manufacturing (HVM) will be feasible. The current technology roadmap expects the 193 nm technology to extend beyond the year

2013, producing integrated circuits at the 32 nm half-pitch node using double-patterning and immersion lithography, and EUVL to start at the 22 half-pitch node in the year 2016 [43].

Although EUVL is conceptually similar to ROL techniques involving visible and deep UV radiation, several of the technological aspects regarding EUVL have hindered its development. Early in the development of EUVL, four key elements were identified as technological challenges for the successful implementation of this technology for manufacturing of semiconductors, namely: the development of a sufficiently bright and reliable EUV source; the availability high resolution photoresists sensitive to EUV radiation; production of high quality multilayer mirrors for the stepper's reduction system; and high quality, defect-free, EUVL masks..

Even though the first three key issues have been mostly resolved, the development of practical tools aimed to study the quality of EUVL masks for HVM remains one of the most critical problems. Several tools for mask inspection are being developed by transferring technology from UV lithography, but the reflective-resonant characteristics of EUVL masks present new challenges that must be met with new and unique systems. The development of imaging systems that can truly assess the printability of EUVL masks under EUV illumination has been ranked as the most pressing issue for the viability of EUVL at the 2009 Symposium held in Prague by SEMATECH, a leading consortium of semiconductor companies.

This chapter is structured as follows. First, a description of the tools employed to print wafers with extreme ultraviolet lithography is given. This is followed by a

description of EUVL masks and the different defects that can affect them. Finally, the current techniques for evaluating these defects using EUV light are analyzed.

2.2. Extreme ultraviolet lithography steppers

Although EUVL is conceptually similar to ROL involving visible and deep UV radiation, the optical system employed in the printing steppers must be based on reflective optics due to the strong absorption of 13.5 nm light in most materials.

Figure 2.2 shows the setup of an all reflective stepper for EUVL comprised of 6 Mo/Si multilayer coated mirrors. The light from an EUV source is collected by a set of mirrors in the illuminator. At this stage the light is filtered and, if needed, debris mitigation is added. The light illuminates the Mo/Si multilayer coated EUVL mask at near-normal incidence. The reflected light is then collected by a projection system that produces a demagnified image of the mask pattern on a photoresist-coated wafer. The number of mirrors in the projection system is optimized to increase the theoretical throughput of the system.

The theoretical throughput is given by the product of the transmittance of the optics and the *étendue*, defined as the product of the illuminated area of the wafer and the solid angle of the imaging cone:

$$\text{étendue} = \text{Area} \times \text{sr} \quad (\text{Eq. 2.1})$$

Initial “ α -tool” steppers have been designed with a 0.25 numerical aperture on the wafer side and a 4 \times -demagnification printing. Although initial designs were based on 4-mirror projectors, current setups use a 6-mirror system which provides a 3-fold increase in theoretical throughput due to the larger *étendue*, despite the loss of transmissivity [45].

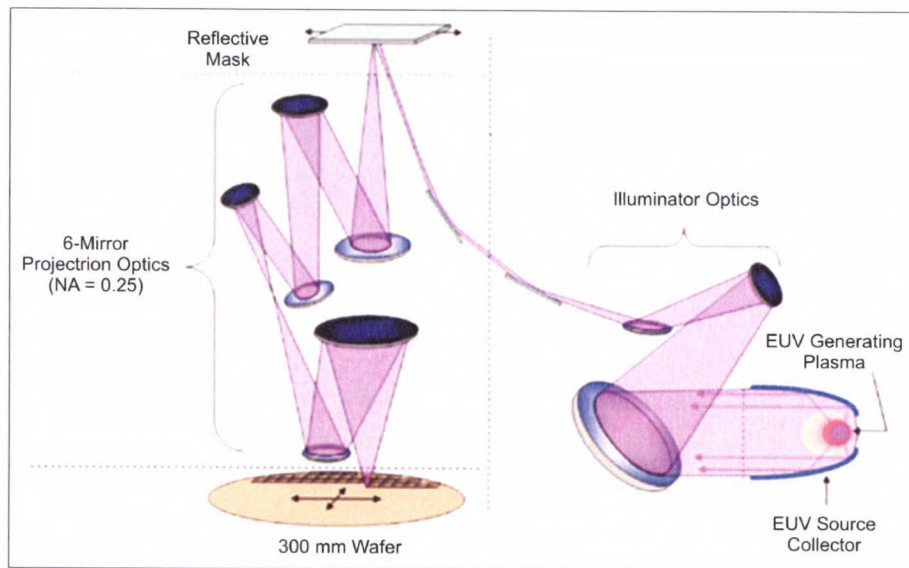


Figure 2.2: Schematic representation of an EUV lithographic stepper. A set of 6 Mo/Si multilayer coated mirrors image the mask onto a wafer with a reduction factor of 4 \times (from [46]).

The optical design determines the total throughput of the stepper which in turn dictates the illumination source requirements. The operational requirements of the stepper in terms of printing speed and lifetime of the optics also impose source requirements. These requirements, as evaluated at the 2009 International Workshop on EUV Lithography, are summarized in Table 2.1.

Today, the main manufacturers of light sources for EUVL are slowly reaching the requirements of in-band power. Using lower power systems, companies such ASML have successfully employed their alpha steppers to print critical layers, such as contact holes on electrically functional devices [47]. Nevertheless, the development of defect-free masks and mask blanks remains a critical roadblock for the extension of EUVL to HVM.

wavelength	13.5 nm
in-band EUV power	115 W @ 5mJ/cm ² - 180 W @ 10 mJ/cm ²
repetition rate	>7-10 kHz
integrated energy stability	±0.3%, 3σ over 50 pulses
source cleanliness	10% reflectivity degradation after 30.000 light-on hours
étendue of source output	3.3 mm ² sr
max. solid angle input to illuminator	0.03 - 0.2 sr
DUV/UV (130-400 nm) spectral purity	<1% at wafer
IR/VIS (>400 nm) spectral purity	<10 - 100% at wafer

Table 2.1. Source requirements for EUVL steppers (table from Dr. Vivek Bakshi's presentation at the 2009 International Workshop on EUV Lithography [48]).

2.3. Types of defects on EUVL masks

Extreme ultraviolet lithographic masks consist of a $6 \times 6 \text{ in}^2$ low thermal expansion glass substrate onto which a Mo/Si multilayer coating is deposited. The multilayer structure is optimized to have maximum reflectivity at 13.5 nm wavelength, providing a theoretical maximum reflectivity of approximately 70%. The pattern to be printed is deposited on top of the multilayer structure using an absorbing material, generally a metal such as chromium.

The defects encountered in EUVL masks can be grouped in two categories: absorption or amplitude defects, and phase defects (Fig. 2.3.a and Fig. 2.3.b respectively). Absorption defects arise from particles located on the surface of the mask that reduce the local intensity of the reflected light, thus printing as a defect on the wafer. This type of defects includes particles on the surface or inclusions in the top layer of the coating. Techniques have been developed to remove debris from the mask without causing damage to the structures [49]. They may also arise from imperfections in the absorber pattern written on the mask as schematically shown in the top region of Fig. 2.3.c.

The second category, phase defects, is comprised of defects in the Mo/Si multilayer structure arising from buried particles or pits in the substrate. As the multilayer is deposited onto the substrate, it conforms over the particles and pits, changing the structure of the multilayer and affecting the phase of the reflected light [50].

Either type of defect can potentially be transferred onto the printed wafer, rendering the components defective. As shown in Fig. 2.3c, the location of these defects with respect to the absorption pattern on the mask is critical. Both types of defects can,

for example, create bridges between exposed lines or disrupt the continuity of a line, affecting the performance of the final device. Figure 2.4 shows an example of a pattern that prints incorrectly because of a defect in the vicinity of the pattern structure. Because of this, great effort has been made in decreasing the number of defects introduced in EUVL masks during production and handling. Currently, the number of defects present on finished masks is ~ 0.3 defects/cm², or equivalently, 70 defects per mask. The goal for masks for high-volume-manufacturing is ~ 0.003 defects/cm², or less than 1 defect per mask, although current research shows that more defects might be acceptable if they are not printable.

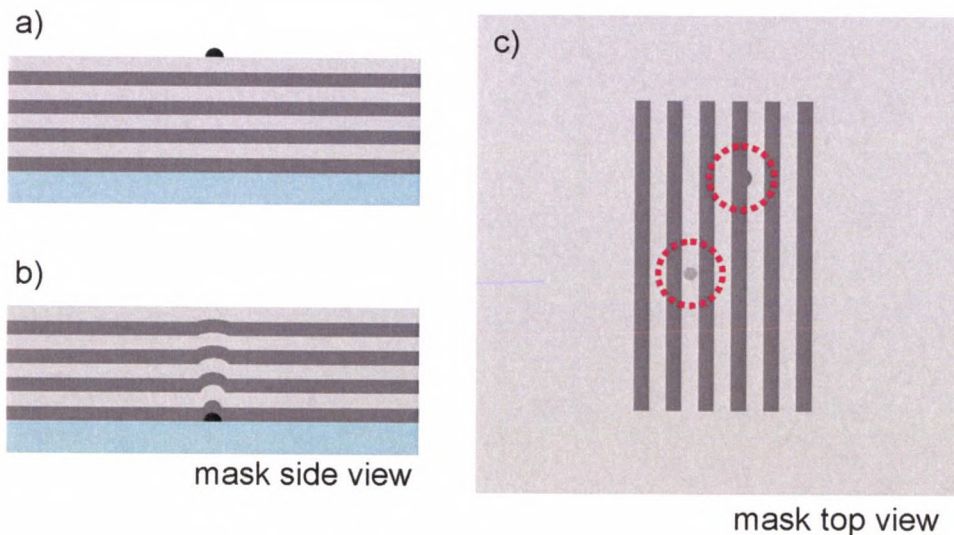


Figure 2.3: Schematic representation of a) amplitude or absorption defects and b) phase defects. c) The position of the defects relative to patterns on the mask is critical.

To reach this stringent limit on number of defects on EUVL masks, new tools are needed to inspect the masks and review their printability. The nature of the phase defects require these tools to operate at the same wavelength used for wafer printing. Tools that

operate at the printing wavelength, ~ 13.5 nm, are often referred to as ‘actinic’, a term that was coined from early photography where it was used to distinguish light that would expose a film from light that would not.

In the next section, the different options for EUV mask metrology are explored, with emphasis on the characteristics of each tool.

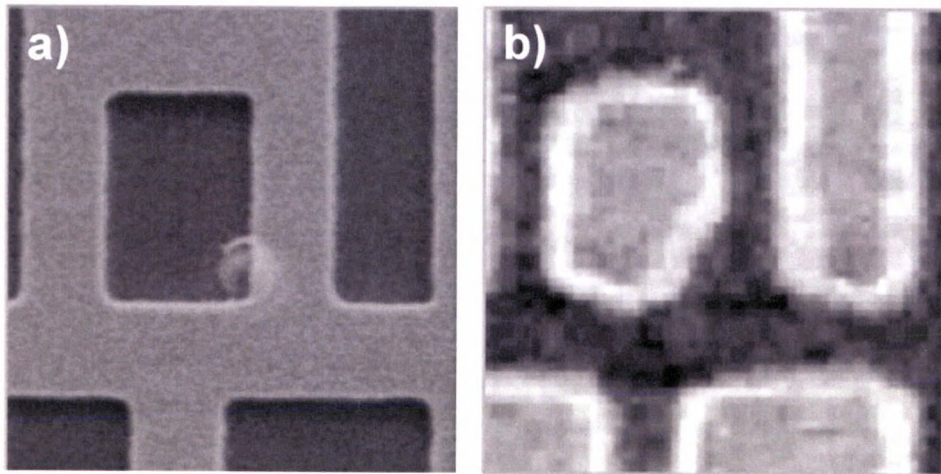


Figure 2.4: a) SEM image of a defect on a pattern of an EUVL mask. b) SEM of the printed wafer produced by the mask, in which the effect of the defect is seen (images from [51]).

2.4. Metrology tools for extreme ultraviolet lithographic masks

As mentioned in the previous section, the availability of reliable metrology tools for EUV masks is currently one of the main concerns for the successful implementation of EUV lithography at high-volume-manufacturing. Tools for EUVL mask inspection can be divided in three categories:

- **Mask blank inspection tools:** capable of scanning a mask before pattern deposition in search of defects on or under the Mo/Si multilayer coating.
- **Aerial image microscopes (AIM):** capable of acquiring images of regions of interest on a patterned mask to evaluate defect and feature printability.
- **Patterned mask inspection tools:** capable of scanning a patterned mask in search of defects and pattern errors.

Although some of these tools can potentially operate at wavelengths outside the bandwidth of Mo/Si multilayers and some companies are successfully developing them using deep-UV sources, the consensus is to have these tools operate around 13.5 nm to better evaluate phase defects and proper printability of patterned features. Figure 2.5 shows the calculated light penetration intensity into an ideal EUV multilayer coating centered at a wavelength of 13.5 nm for the two wavelengths currently used in optical lithography, 248 nm and 193 nm, and for the printing wavelength, $\lambda=13.4$ nm [52]. The multilayer consists of forty 6.94 nm periods of Mo/Si bi-layers with a Mo to Si ratio of $r=0.394$. The EUV light penetrates deeply into the multilayer structure producing a standing wave due the resonant characteristics of the multilayer stack. On the other hand, the other wavelengths, 488 nm and 266 nm, rapidly decay within the first tens of nanometers of the structure.

Each actinic inspection tool has different requirements regarding illumination source, illumination brightness, system throughput, imaging area, etc. Because these

requirements are less demanding than those needed by EUVL steppers, especially regarding the illumination brightness, different sources with lower cost of ownership can be used.

The main requirement in mask inspection systems is the illumination source's average brightness given in terms of average power divided by the *étendue* of the system and generally expressed as $W/(mm^2 \text{ sr})$. The brightness specifications for each type of mask inspection system, as evaluated at the 2009 International Workshop on EUV Lithography organized by EUV Litho, Inc. in Hawaii, are presented from the perspective of the tools suppliers and the masks suppliers in Table 2.2 and Table 2.3 respectively.

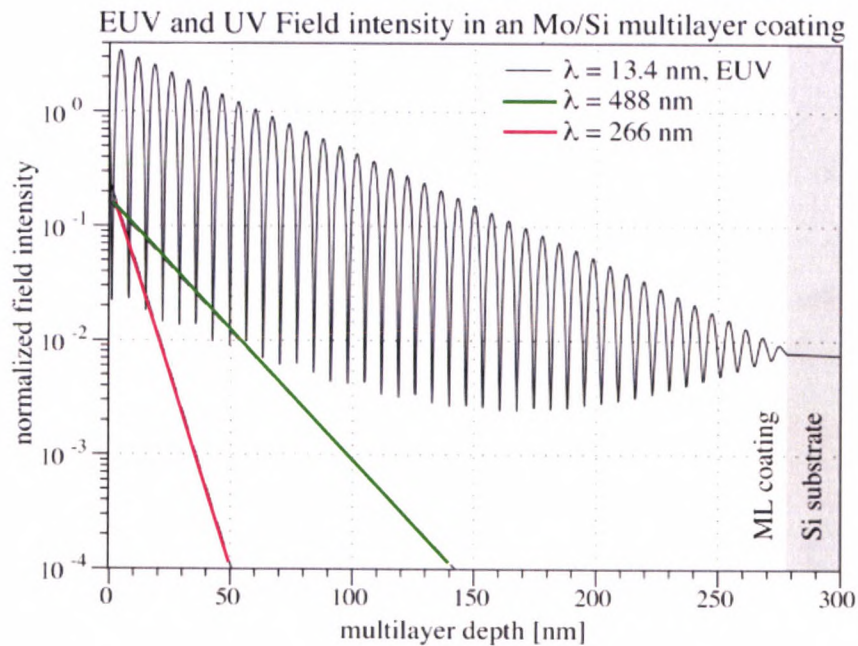


Figure 2.5: Calculated light penetration intensity into an ideal EUV multilayer coating for three different wavelengths at normal incidence. The coating period $d = 6.940 \text{ nm}$, and $\Gamma = 0.394$ (figure from [52]).

Tool / Supplier	Zeiss	Selete	KLA Tencor
Actinic Blank Inspection	50 W/(mm ² sr) After foil	14 W/(mm ² sr) Before foil	
AIM	100 W/(mm ² sr) After foil		
Actinic Patterned mask Inspection			300-2500 W/(mm ² sr) Before foil

Table 2.2: Tool suppliers requirements for source brightness (table from Debbie Gustafson's presentation for Energetiq at the 2009 International Workshop on EUV Lithography [48]).

Tool	Source brightness
Actinic Blank Inspection	>500 W/(mm ² sr)
AIM	>200 W/(mm ² sr)
Actinic Patterned mask Inspection	>2000 W/(mm ² sr)

Table 2.3: Mask suppliers requirements for brightness of mask inspection tools (table from Dr. Vivek Bakshi's presentation at the 2009 International Workshop on EUV Lithography [48]).

To date, a limited number of actinic mask blank inspection tools and aerial image measurement systems are available for EUV masks metrology. Furthermore, these systems generally rely on using synchrotron radiation for illumination, limiting the access of mask suppliers to valuable inspection tools. In the next sections the current status of these tools, with emphasis on AIM, is presented.

2.4.1 Scanning mask inspection microscopes

Standard inspection tools for transmission mask blanks used in today's chip manufacturing scan the mask with visible-UV laser light in order to detect the scattered light from imbedded defects in the quartz substrate that, during the printing process, would induce intensity changes on the photoresist, resulting in printing errors. This methodology has been adapted to inspect the reflective EUVL masks, with the Japanese corporation Lasertec leading the way with two inspection tools operating at 488 nm and 266 nm wavelength [52-55]. These tools, developed in coordination with SEMATECH, can inspect a 6 × 6 inch square EUVL mask in approximately one hour with a detection sensitivity of 30 nm.

The main concern with these non-EUV inspection techniques is the uncertainty in determining the rate at which false positives and false negatives appear in commercial masks [56]. A false negative occurs when the inspection tool is not sensitive enough to all printable EUV defects. If this occurs and the mask is sent to production, the defects could appear in the printed wafers resulting in costly production losses. On the other hand, false positives, where masks are discarded due to wrongly classified anomalies

which would not print at EUV wavelengths, are also highly undesirable due to the high cost of mask production.

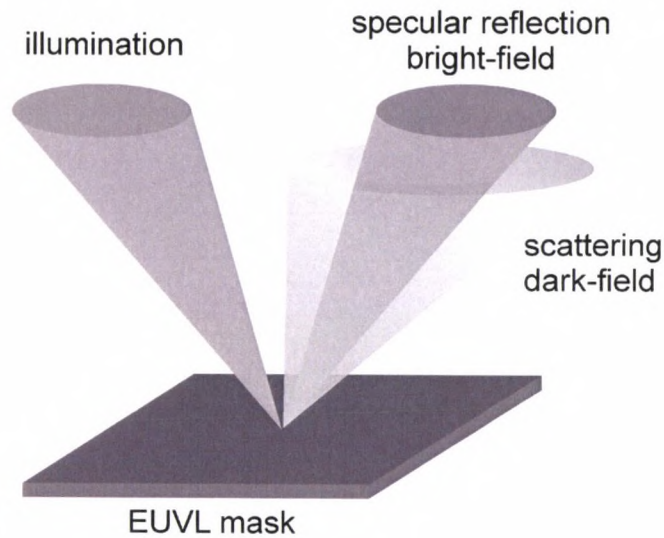


Figure 2.6: Defects on a mask are located by monitoring the specular reflection and/or the light scattered from defects.

Actinic scanning inspection tools operate in a similar manner as their non-EUV or non-actinic counterparts. Light of a wavelength that falls within the reflectivity bandwidth of Mo/Si multilayers is focused onto the surface of a mask at an angle close to normal. As shown in Fig. 2.6, this produces two different signals that can be monitored to search for defects on the mask.

The specular reflection or ‘bright-field’ is generally monitored to detect amplitude or absorption defects due to particles or contamination on the surface of the multilayer. The detection is achieved straightforwardly by collecting the reflected beam with a photodiode detector large enough to capture the entire cone of reflected light. On the other hand, the ‘dark-field’ is monitored to detect phase defects. As the incoming light

interacts with a defect on the EUVL mask, the amount of scattered light increases. By collecting the light outside of the specular reflection, in the ‘dark-field’, the changes in scattered light can be measured and the defects located. Because the light scatters in all directions, selecting a detector with a sufficiently high numerical aperture that also avoids the specular reflection is crucial [52].

The first actinic scanning microscope was developed at the Advanced Light Source (ALS) synchrotron in Berkeley, California in 1998 [50, 57-59]. This scanning microscope, which operates around $\lambda=13.4$ nm, could simultaneously measure the dark-field and bright-field signals, detecting defects in the 100 nm range.

In 2003, Tezuka and collaborators introduced a new concept for dark-field microscopy. They developed a microscope based on a Schwarzschild objective to produce a magnified image of the light scattered off a mask [60-62]. This system was illuminated using a laser-produced plasma (LPP) source operating at 10 Hz and producing 8 ns pulses of 380 mJ energy at 13.5 nm wavelength. The instrument produced large field-of-view dark-field images in which the scattered light from programmed defects appears as a bright pixel or group of pixels on the detector. With this system, all of the programmed phase defects in the mask, down to 70 nm in width and 2 nm in height, could be detected with a statistical estimate of less than one false defect.

While progress was being made in Japan with the dark-field imaging tool, a new scanning microscope for bright-field and dark-field detection at 13.5 nm wavelength was built at the Advanced Light Source in Berkeley, California, USA [56]. This tool, together with the one in Japan, was used to perform cross-comparison measurements of a

programmed defect mask [54]. In this test, both EUV microscopes were compared to the Lasertec non-EUV inspection instruments using a single programmed defect EUVL mask with a range of buried bump-type defects. The main conclusions drawn from this study were that, although the non-actinic tools had high sensitivity to large defects and could scan the mask at a much faster rate than the EUV microscopes, the sensitivity to smaller defects was poor. On the other hand, the EUV tools were able to detect all of the programmed defects but at a lower scan rate. At this point, it is still debatable which technique will be employed for commercial mask inspection, but the benefits of having actinic tools, though slow in scanning, has been demonstrated.

Although these actinic scanning microscopes have shown great potential for locating irregularities on EUVL masks, there are still open questions regarding the impact of these defects in the printing process. By simply recording the reflected intensity or the scattered light, no insight is gained regarding the printability of the defects. One way to overcome this is to use a prototype printer to evaluate the mask after inspection. This approach is particularly useful if the printer simulates the operation conditions expected for a commercial EUVL stepper. The down side of this approach is that it is extremely time-consuming since a wafer must be printed, processed, and finally scanned using a technique such as atomic force microscopy or scanning electron microscopy. Furthermore, decoupling the effects of the EUV-sensitive photoresist from the performance of the mask is not trivial, specially considering that at this point the resists are still under development.

To overcome these issues, a different tool is needed for pattern and defect characterization. Aerial Image Microscopes (AIM), or actinic full-field reflection

microscopes can directly obtain images of selected regions of the EUVL mask where defects have been identified. These tools are reviewed in the next section.

2.4.2 Aerial image microscopes

Full-field actinic microscopes or aerial image microscopes (AIM) are currently needed for the realization of high-volume-manufacturing EUV lithography. The need for these actinic microscopes for defect and pattern printability evaluation was observed early on by both leading groups in Japan and the United States, which started developing them in parallel with the actinic scanning inspection tools.

In Japan, a full-field microscope was developed using a set of mirrors in a Schwarzschild configuration. The Schwarzschild was used simultaneously as condenser and objective [63-69]. In this microscope, as shown in Fig. 2.7, light from the NewSUBARU storage ring is focused by the Schwarzschild onto the sample. The reflected light is collected by the same optics and, using a beam splitter designed for 13.4 nm wavelength light, the image is projected onto a CCD detector. Using this system, gratings with 300 nm half-pitch were successfully resolved and programmed phase defects smaller than 100 nm were clearly observed.

At the Advanced Light Source, a full-field actinic microscope was incorporated to the scanning microscope, resulting in a dual mode imaging system. Using the same instrument, an EUVL mask can be scanned in bright-field or dark-field to locate defects that can then be imaged with a high resolution full-field microscope [49, 56, 70, 71]. The setup of this microscope is shown in Fig. 2.8.

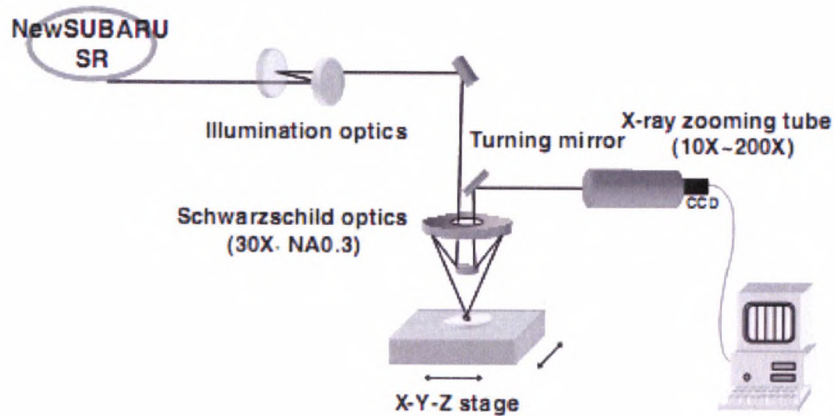


Figure 2.7: Full-field actinic microscope at NewSUBARU. A Schwarzschild is used simultaneously as condenser and objective to obtain aerial images of EUVL masks. (figure from [69]).

A unique characteristic of this full-field microscope is that it is designed to emulate the illumination and imaging conditions of an EUVL stepper. The main advantages of the microscope and the design parameters were described by Barty in 2002 [70]. According to Barty, by mimicking an EUVL stepper the printability of multilayer and pattern defects could be evaluated; success after a defect repair process could be assessed; the effects of illumination and numerical aperture on the printed image could be studied; and by characterizing defects and defect printability, a lithography process window could be established. To emulate a stepper, the NA of the projection system facing the mask in the stepper must be matched by the NA of the microscope's objective.

The first generation production tools have a numerical aperture of 0.25 NA with a demagnification of 4 \times , although more recently numerical apertures as high as 0.30 and demagnifications of 5 \times are also being considered. Since 0.25 NA corresponds to the wafer side, from the mask's perspective the optical system sees a numerical aperture of

0.0625 NA in a 4 \times -demagnification stepper. Thus, an actinic microscope designed to mimic the stepper should have an objective lens with a numerical aperture close to 0.0625.

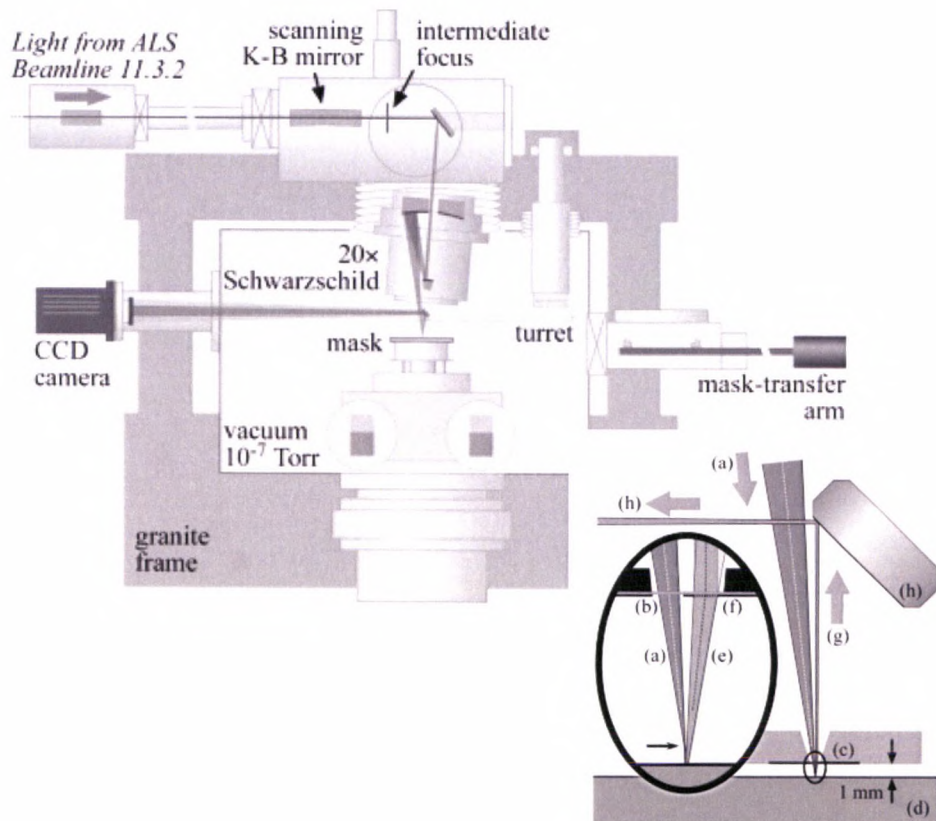


Figure 2.8: SEMATECH-Berkeley full-field actinic microscope design. This microscope uses a Schwarzschild condenser to focus the light onto the mask. An off-axis zone plate is used as the objective. The insert shows the path of the light through the zone plate design. A 45 degree Mo/Si multilayer coated mirror is used to project the image onto the CCD camera. (figure from [71]).

The full-field microscope developed at the ALS was designed according to these considerations [71]. The condenser is the same Schwarzschild used to focus the light in scanning mode. The objective is a specially designed off-axis zone plate with 0.0625 NA

and a focal distance of 1 mm. The microscope produces magnified images of the mask that render information on the printability of patterns and defects.

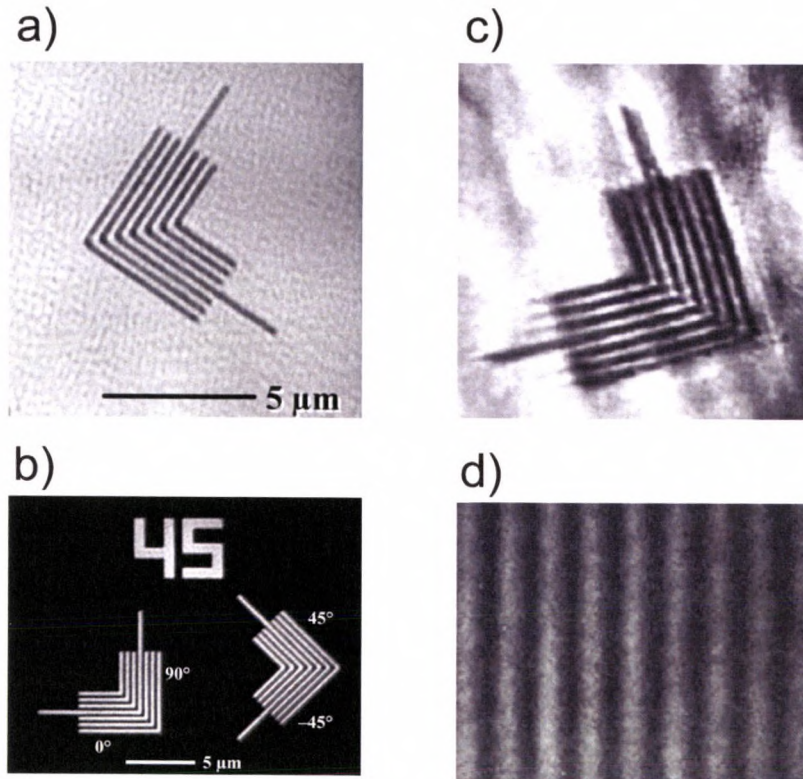


Figure 2.9: EUV images of a) 175 nm half-pitch elbow pattern, and b) 225 nm half pitch elbow pattern obtained with the AIT at Berkeley. EUV images of c) 500 nm half-pitch elbow pattern, and d) 300 nm half-pitch elbow pattern obtained with the EUVM at NewSUBARU (Images a) and b), and c) and d) from [69, 71] respectively).

Both the ALS and the NewSUBARU full-field microscopes have been instrumental in the development of EUVL. As shown in Fig. 2.9, they can readily obtain images of patterned EUVL masks and assess the printability of patterns and defects. The microscope at NewSUBARU can obtain images with exposures of approximately two minutes with a spatial resolution of less than 200 nm. The AIT at ALS uses exposure

times of a few seconds for pattern location and of 90 seconds for high quality images. This microscope has a spatial resolution better than 80 nm and produces images with sufficient quality for pattern characterization.

One of the main limitations of these tools is that they employ light from large synchrotron facilities which limits their accessibility to the industrial community. The implementation of actinic full-field microscopes that can be used for on-site EUVL mask inspection and development in an industrial setting requires the availability of compact light sources that provide sufficient flux near 13.5 nm wavelength. The next chapter describes the details of the development of an actinic full-field microscope for AIM imaging of EUVL masks using a tabletop EUV laser. The results obtained with this system are reviewed in Chapter 4.

2.5 Pattern characterization from EUV images

One of the main functions of the table-top actinic AIM microscope is to characterize the printability of mask patterns before the masks go into chip production. Errors in the absorption layer of the mask or high roughness of the Mo/Si multilayer coating can greatly affect the printability of lines, rendering the printed chip non-functional [72, 73]. One way of analyzing the pattern printability is to evaluate parameters such as normalized image log-slope (NILS) and line-edge roughness (LER) from images of the mask, such as those obtained from a microscope described in this dissertation. These parameters can also be obtained from mask patterns printed using an EUVL stepper. However, in this case the results are a convolution of the mask and the resist responses.

Normalized image log-slope (NILS), measured as the derivative of the logarithmic of the image's intensity, assesses the steepness of the intensity slope along the imaged features:

$$\text{NILS} = \frac{\partial \ln I}{\partial x} \quad (2.2)$$

where I is the intensity of the image and x is the direction perpendicular to the feature's edge.

Line edge roughness (LER) is a statistical measure of the variation in position of the edge of a feature along the features' extent. When the LER, measured as three times the standard deviation of the position, is below 10% of the CD value for the specific line, the features, and consequently the mask, are considered acceptable. Both parameters are related and are inversely proportional.

$$\text{LER} = 3 \times \sigma_{st} \quad (2.3)$$

By analyzing these values on an aerial image, the quality of the pattern on the surface of the mask can be determined independently of the response of the photoresist on the printed wafer which generally degrades these values.

The values obtained for NILS and LER on a mask depend on the coherence of the illumination of the microscope and on the focus or defocus of the features being analyzed. The effects on these parameters were analyzed experimentally and extensively through simulations by P. Naulleau [72, 73]. The interaction of partially coherent light with the roughness of the multilayer structure determines the level of speckle present in the image, which in turn dictates the contrast in the features. This effect can be seen in Fig. 2.10 where LER measurements were obtained from simulated 90 nm half-pitch grating images assuming an ideal 0.1 NA stepper [72]. As shown in the figure, the effect

of the spatial coherence is minimal at best focus and becomes apparent as out-of-focus images are considered.

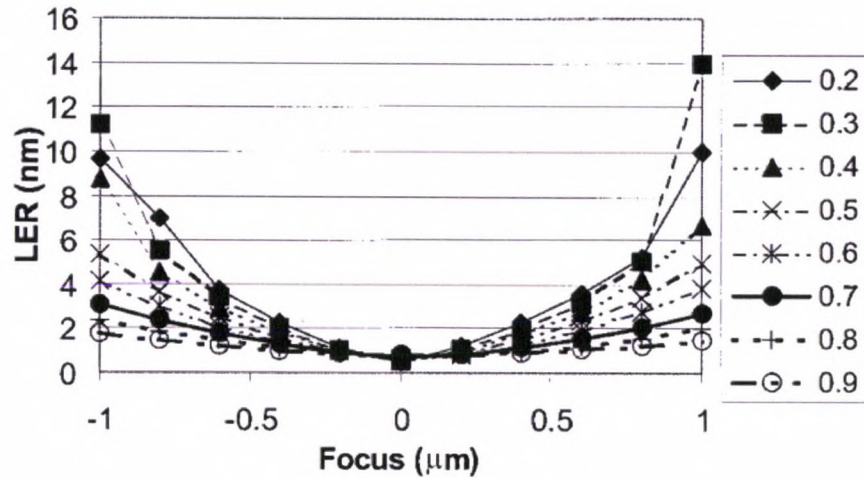


Figure 2.10: Simulated LER measurements on a 90 nm half-pitch grating assuming an ideal 0.1 NA stepper (image from [72]).

The determination of these parameters aids in the development of new designs for mask patterning, crucial for the extension of EUVL to smaller feature printing capabilities. The EUV microscope presented in this dissertation was used to evaluate these parameters on an EUVL mask. This analysis is presented in Chapter.

CHAPTER 3: Actinic table-top microscope for EUVL mask characterization

3.1. Introduction

In this chapter, the realization of the first laser-based, table-top, actinic aerial microscope for EUVL mask inspection is presented. This microscope has been enabled by the development of table-top EUV lasers at Colorado State University and optics by the Center for X-Ray Optics at Berkeley through the NSF Engineering Research Center for Extreme Ultraviolet Science and Technology.

The developments presented in this chapter have resulted in the publication of two articles in peer-reviewed journals, as well as several conference presentations and proceedings which are listed in Chapter 6.

The chapter is structured as follows: first, the microscope's design is described; this is followed by a detailed description of the illumination laser source and the optics employed. Finally, some considerations on the acquisition of images are reviewed along with an analysis of the throughput of the system and a comparison between probing the multilayer masks with 13.2 nm light and 13.5 nm where the reflectivity reaches its maximum. The characterization of the performance of the microscope, along with measurements of EUVL masks, is presented in Chapter 4.

3.2. Table-top EUV-AIM: microscope setup.

As shown in the previous chapter, several choices of systems exist for the development of an actinic mask inspection microscope. Different system setup designs have been extensively investigated several years ago by SEMATECH and recently reviewed by Feldman *et al.* at Carl Zeiss [74]. Each system has advantages and disadvantages in terms of design and expected performance. In this review, three configurations are considered:

- **EUV mirror system with secondary magnification** in which a low magnification EUV image is created using a Schwarzschild objective and then magnified using either a visible microscope and a scintillator crystal or an electron microscope.
-
- **Zone plate based system** in which a high magnification image is generated using an off-axis Fresnel zone plate.
-
- **All EUV mirror system** where the high magnification image is created using curved Mo/Si coated mirrors.

The microscope developed at Colorado State University is based on an EUV laser that emits at 13.2 nm wavelength, well within the reflectivity band-pass of the Mo/Si multilayer coatings of EUVL masks. The microscope was designed to mimic the

imaging conditions of a 0.25 NA, 4×-demagnification EUVL stepper like the one described in the previous chapter (Fig. 2.1).

The zone plate based system approach was used in the design of the microscope. This approach is best suited based on the illumination employed since the laser provides highly monochromatic light. This design also allows for increased simplicity of the optical system and reduction of optical aberrations while still providing sufficient photon flux due to high brightness of the laser. The microscope can accommodate standard EUVL masks, imaging any area within their central one square inch region.

The microscope is housed in a $70 \times 45 \times 40 \text{ cm}^3$ vacuum chamber connected to the exit port of the laser chamber by a manual isolation valve. The operating pressure is $<2 \times 10^{-5}$ torr. The foot-print of the whole system is determined by the size of the laser system which, including its amplification stages, occupies four standard optical tables.

A 100 nm thick Zr filter located at the exit port of the laser eliminates unwanted visible plasma light from reaching the microscope chamber. After filtering, the output of the laser is guided by a flat Mo/Si multilayer coated mirror to a condenser zone plate which focuses the light onto the sample at an angle of incidence of six degrees. The reflected light is collected by an off-axis zone plate objective, forming the image on a back-illuminated CCD detector along the normal direction to the sample.

A schematic representation of the microscope setup along with a picture of the interior of the microscope is shown in Fig. 3.1.

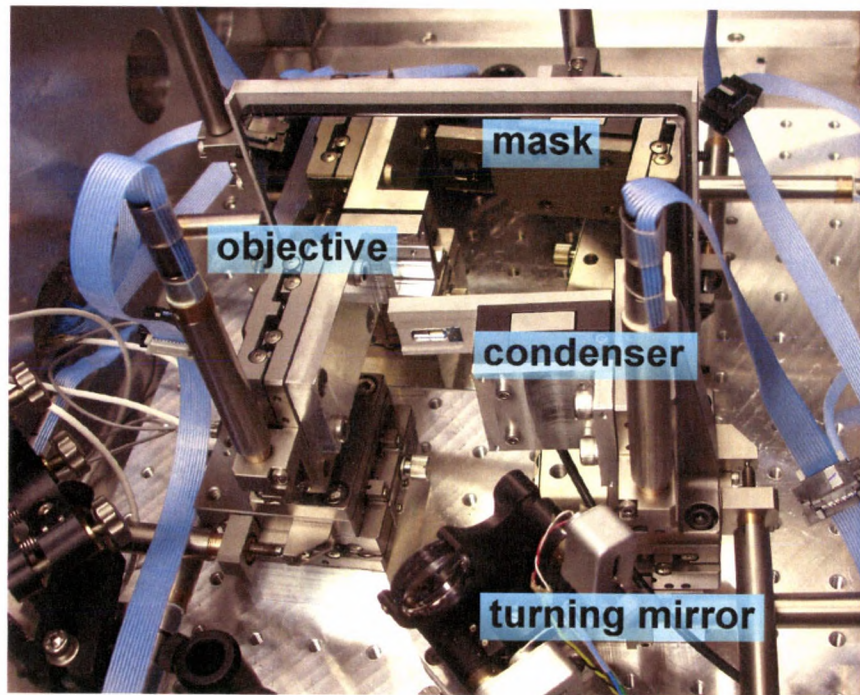
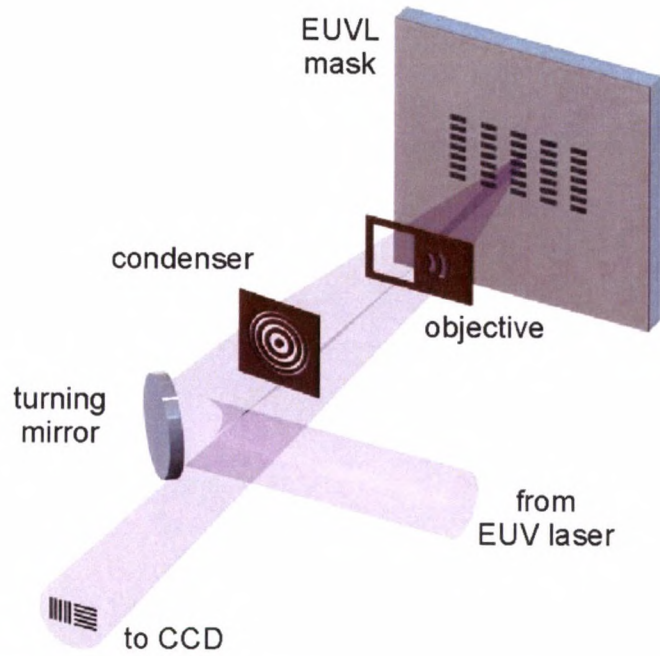


Figure 3.1: Schematic of the compact actinic mask inspection tool, and picture of the microscope chamber.

Precise control of the microscope's components is required during system alignment and image acquisition. To this end, 14 motorized actuators with a travel of 25 mm, a minimum repeatable increment of $0.2\mu\text{m}$, and a backlash of $12\mu\text{m}$ are used to control the turning mirror, the condenser, the sample, and the objective which are mounted on XYZ translation stages of equal travel. A linear piezoelectric stack with feedback mounted on the stage of the objective is used to optimize the focus to acquire sharp EUV images. An XY piezoelectric stage is also used to move the condenser during image acquisition to improve the illumination of the image.

The optical design of the microscope along with motion control systems employed makes the microscope simple to use. Furthermore, an alignment procedure has been developed to expedite the initial alignment of the microscope. This procedure will be explained in section 3.5.3.

The characterization of the microscope and the results presented in this dissertation were obtained over two time periods or imaging campaigns. After the first demonstration of the microscope, some modifications were made to the system to address issues encountered in the quality of the images. These changes followed the valuable input of several chip manufacturing companies and will be discussed in the corresponding sections.

3.3. Table-top EUV-AIM: description of the 13.2 nm wavelength laser illumination

A high repetition rate laser operating at wavelengths in the EUV region down to 10.9 nm has been developed at Colorado State University [75]. This laser is capable of generating

single line emission at different wavelengths from 32.6 - 10.9 nm, corresponding to $3p^1S_0-3s^1P_1$ transitions in Ne-like ions and $4d^1S_0-4p^1P_1$ transitions in Ni-like ions. The laser wavelength is selected by choosing the appropriate target material as shown in Fig. 3.2.

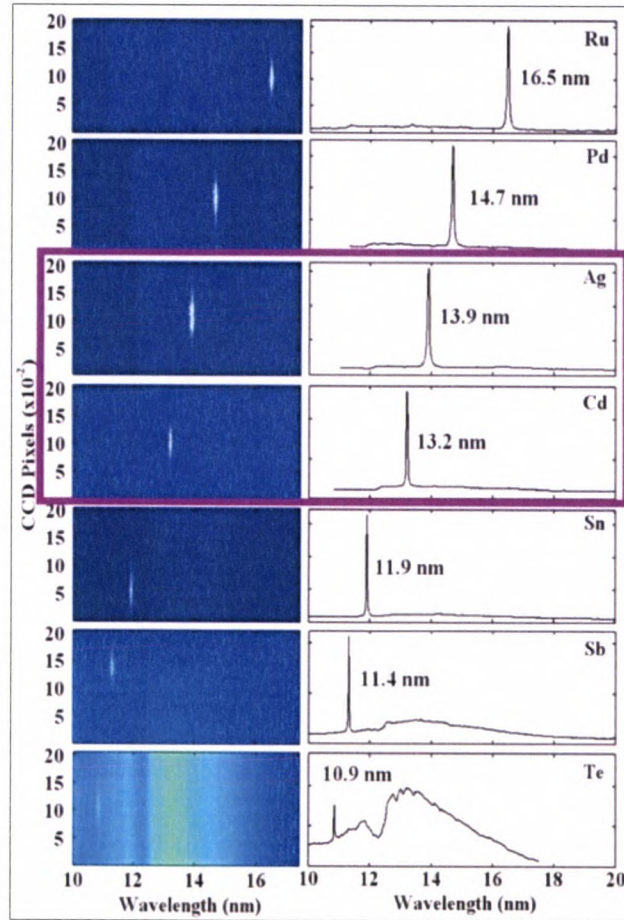


Figure 3.2: On-axis spectra of wavelengths between 16.9 nm and 10.9 nm, corresponding to the $4d - 4p$ transitions in Ni-like ions in plasma formed from 4 mm long targets of Ru ($Z=44$), Pd ($Z=46$), Ag ($Z=47$), Cd ($Z=48$), Sn ($Z=50$), Sb ($Z=51$) and Te ($Z=52$) (figure from [76]).

Of these lasers, there are two that operate in the saturated regime around the wavelength required for EUV Lithography, 13.5 nm, that are potential candidates for table-top actinic microscopy (highlighted in Fig. 3.2) [75, 77]. Nickel-like silver ($Z = 47$)

lases at a wavelength of 13.9 nm, while Ni-like cadmium ($Z = 48$) produces picosecond pulses at 13.2 nm wavelength.

Although Mo/Si multilayer mirrors used in EUVL steppers are designed to have peak reflectivity at 13.5 nm with a typical bandwidth of approximately 0.7 nm, their asymmetric reflectivity curves result in higher reflectivity at 13.2 nm (~55% compared to ~10% at 13.9 nm). This makes the Ni-like Cd laser better suited for the implementation of table-top EUVL mask inspection microscopes.

The $\lambda=13.2$ nm laser beam is generated by amplification of spontaneous emission in a transient population inversion produced by electron impact excitation of nickel-like cadmium ions in a plasma column [75, 77]. The plasma column results from the ablation of a 4 mm long Cd target slab with a 120 picosecond pulse from a chirp-pulse-amplification Ti:Sapphire laser system. The population inversion is achieved by heating the plasma with a second 8 picosecond pulsewidth pulse incident at a grazing angle of $\theta = 23$ degrees. In this way, highly monochromatic ($\Delta\lambda/\lambda < 1 \times 10^{-4}$) EUV pulses of up to 200 nJ energy are produced.

Generally, the laser is operated at a repetition rate of 5 Hz resulting in approximately 1 μ W average power. The pulse-to-pulse output of the laser is shown in Fig. 3.3 for a series of 150 contiguous pulses in which lasing is observed for each shot with an intensity variation characterized by a standard deviation of 23%.

An optimum electron density in the plasma exists for amplification by transient collisional excitation. For Ni-like Cd, this density is equal to 2.8×10^{20} cm³. The grazing incidence scheme allows effective coupling of the energy of the heating pulse with the

correct electron density as $n_e = \theta^2 \times n_{ec}$, where n_{ec} is the critical electron density at the wavelength of the pump, in this case $5.3 \times 10^{17} \text{ cm}^{-3}$ at 800 nm wavelength.

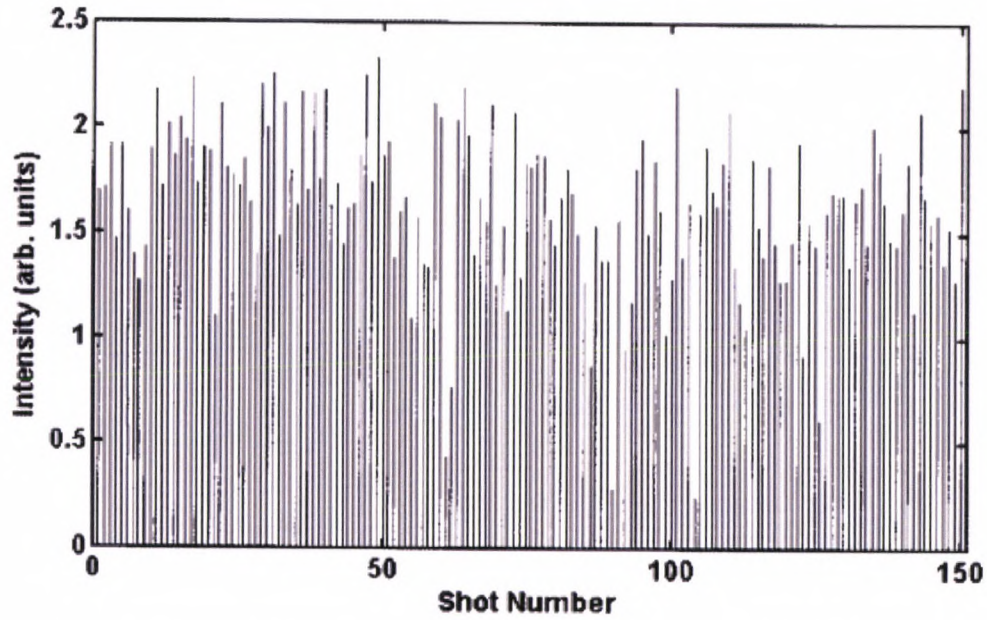


Figure 3.3: Sequence of 150 contiguous laser pulses of the 13.2 nm Ni-like Cd laser acquired at a 5 Hz repetition rate. The grazing angle of incidence of the short pulse was 20 degrees (figure from [77]).

The output of the laser has a divergence of ~ 14 mrad in the direction parallel to the metal target and ~ 7 mrad in the perpendicular direction, as measured by looking at far-field images of the beam [77].

The coherence properties of the illumination source play an important role in the spatial resolution and the quality of the images obtained with full-field EUV microscopes. The spatial coherence of the laser was measured by means of a Young's double slit experiment [78]. Figures 3.4 (a), (b), and (c) show the interferograms obtained for 5 μm slits separated by 30 μm , 50 μm , and 75 μm and placed 105 cm from the laser output. From the measurements, a transverse coherence length of about 1/20 of

the beam diameter was obtained. This moderate spatial coherence makes the laser well suited for matching the illumination coherence requirements of the EUVL stepper.

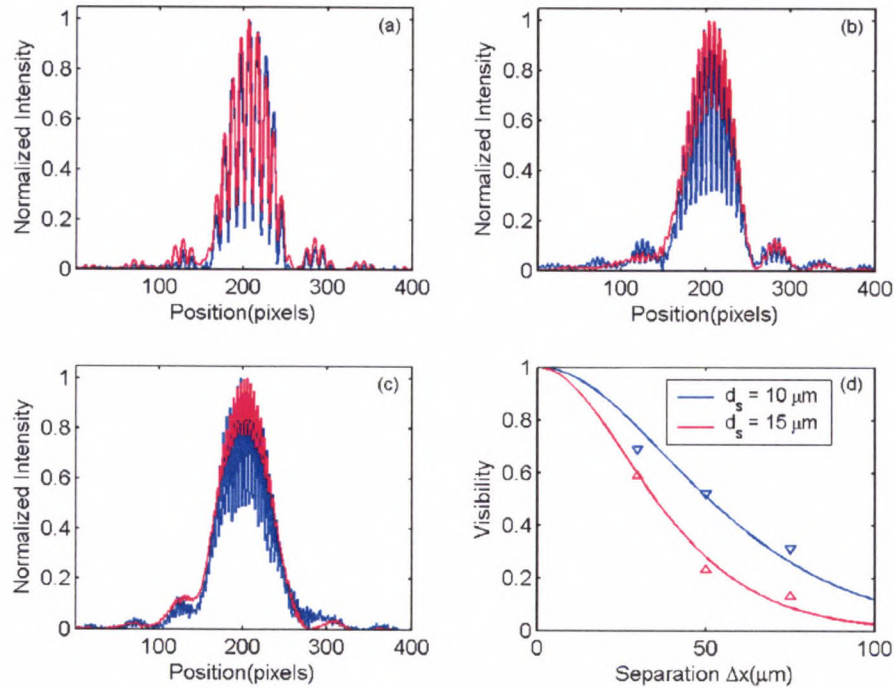


Figure 3.4: Interference fringes with average visibility (red), obtained by integrating the whole interferograms, and fringes with highest visibility (blue), picked by manually scanning the interferograms. The slit separations are (a) $30 \mu\text{m}$, (b) $50 \mu\text{m}$, and (c) $75 \mu\text{m}$. (d) Experimental data of fringe visibilities at different slit separations and theoretical predictions based on the van Cittert-Zernike theorem. The source size is $10 \mu\text{m}$ (blue, corresponding to highest visibilities) and $15 \mu\text{m}$ (red, corresponding to average visibilities) (figure from [78]).

The laser has recently been operated at repetition rates of up to 2.5 Hz producing an average power of approximately $20 \mu\text{W}$ at 13.9 nm wavelength using a Ag target [79]. To obtain the results of the second imaging campaign, the laser was operated at 1 Hz repetition rate to produce an average power of a several μW . The new laser system had a

divergence of 9 ± 0.5 mrad FWHM parallel to the slab target and 10 ± 0.5 mrad in the perpendicular direction.

3.4. Table-top EUV-AIM: description of the microscope's optics

The majority of EUV microscopes are based on Fresnel diffraction optics because, albeit their relatively low throughput, they allow for manipulation of beams with low aberrations, approaching the diffraction limit at a relatively low cost. The EUV-AIM developed at CSU employs not only a zone plate objective, but also a zone plate condenser. The use of a zone plate condenser, possible due to the directionality and small divergence of the EUV laser, significantly simplifies the optical design of the microscope.

The condenser zone plate used in the microscope has a diameter of 5 mm, an outer zone width of 100 nm, and a focal distance of 38 mm at 13.2 nm wavelength. At the condenser plane, the laser beam slightly overfills the zone plate, optimizing the amount of light transmitted through the system. Because of geometrical constraints, the condenser had to be fabricated next to an aperture to avoid blocking the image formed by the objective onto the CCD. This was achieved by writing the zone plate onto a Si wafer with a 2×2 array of 5mm wide silicon nitride windows. The membrane on the window adjacent to the condenser was removed forming the aperture. A schematic of the condenser design and aperture is shown in Fig. 3.5.a.

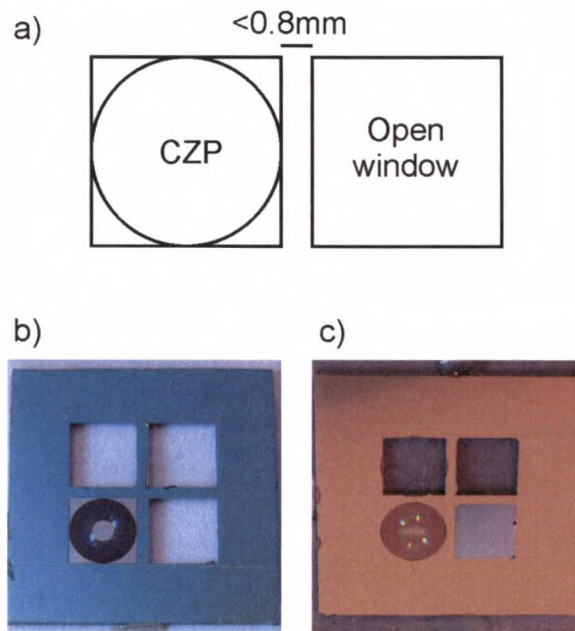


Figure 3.5: a) Schematic and picture of the condenser zone plates used in the microscope. The open window next to the lens is needed to allow the transmission of the image formed by the 1st order of the objective zone plate. The distance between the condenser and the window needs to be less than 0.8 mm. b) Zone plate condenser with central stop. c) Zone plate condenser without central stop.

The picture shown in Fig. 3.5.b corresponds to the condenser used during the first imaging campaign. As seen in the picture, it has a central stop of 1.7 mm, which blocks a portion of the 0th order light from reaching the sample. For the second campaign, the condenser was upgraded to a similar zone plate but with zones written down to the center of the lens (Fig. 3.5c). This new design was instrumental to achieve improved illumination uniformity as will be described more extensively in the next chapter.

The objective zone plate used in the microscope has an off-axis design similar to the one used at the SEMATECH Berkeley Actinic Inspection Tool (AIT) for mask inspection. It has diameter of 120 μm and a focal distance of ~ 1 mm at this wavelength. Its numerical aperture, $\text{NA}=0.0625$, was chosen to emulate the imaging characteristics of a typical 4 \times stepper, $\text{NA} = 0.25$ at wafer, used for EUV lithography.

An SEM micrograph of the off-axis objective zone plate is shown in Fig. 3.6. The off axis zone plate was designed from a regular ‘parent’ zone plate 0.33 mm in diameter (dashed line in the figure) with an outer zone width of 40 nm onto which a smaller pupil is overlapped. The pupil, ~0.12 mm in diameter, is placed ~0.10 mm from the axis of the parent zone plate, tangent to its edge. This pupil defines the numerical aperture of the objective, 0.0625NA, while the focal distance, 1 mm is defined by the outer zone width of the parent zone plate. The image is formed parallel to the surface of the zone plate because within the pupil the zones are written with their radius defined by the parent zone plate. A rectangular window next to the off-axis objective zone plate is left uncoated. This window allows the transmission of the condenser illumination to the mask at an angle of incidence of 6 degrees. The reflected light from the mask efficiently fills the pupil of the off-axis zone plate.

Since the light travels through the off axis objective twice (first through the window and then through the zone plate) the Si_3N_4 membrane onto which the objective was patterned was thinned down from 100 nm to 40 nm, significantly improving its throughput. The design of the zone plate structure enables normal incidence imaging of the mask surface, minimizes aberrations, and helps reduce the coherence of the illumination by matching the NA of the condenser [80].

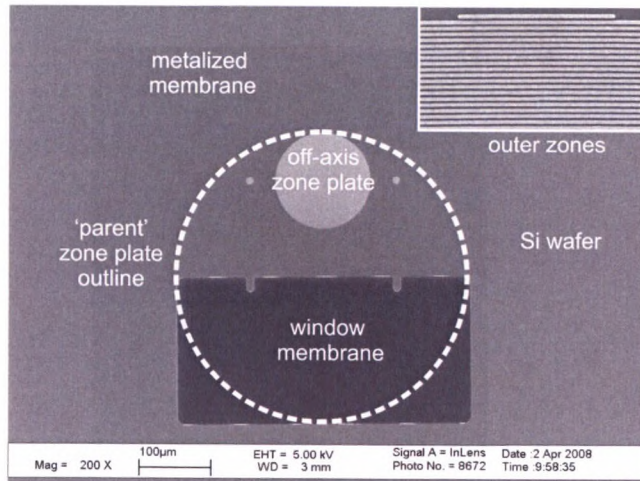


Figure 3.6: SEM image of the off-axis objective zone plate. The position of the ‘parent’ zone plate is indicated with dashed lines. The insert in the upper right corner shows the 40 nm outer zones.

3.5. Table-top EUV-AIM: description of the EUV mask samples

Extreme ultraviolet masks are made of a 6×6 in² low-thermal expansion glass substrate coated with a Mo/Si multilayer. The coatings on the masks are designed to have the highest reflectivity at a wavelength of $\lambda = 13.5$ nm with a typical bandwidth of approximately 0.6 nm.

These coatings consist of a stack of alternating high and low Z materials with a periodicity of $d = \lambda / (2 \sin \theta)$ where λ is the illumination wavelength and θ the angle between the surface and the incident radiation. The structure is usually composed of 30 to 60 layer pairs deposited by DC magnetron sputtering [81]. The resulting reflectivity of the multilayer is highly dependant on surface roughness and interdiffusion of the layers. For this reason, much work has been done to address these issues [82-86].

Figure 3.7 shows a simulated reflectivity curve for a typical Mo/Si multilayer structure centered at $\lambda=13.5$ nm consisting of 60, 25.3 nm thick pairs of Mo and Si. These multilayers can achieve reflectivity values over 70% at $\lambda=13.5$ nm and over 50% at the microscope's working wavelength, $\lambda=13.2$ nm. The reflectivity curve was calculated using tabulated data from CXRO.

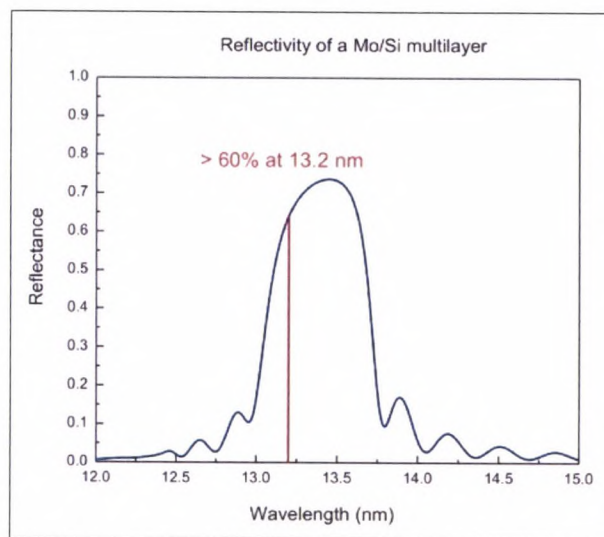


Figure 3.7: Theoretical reflectivity of a Mo/Si multilayer. Number of layers: 60, period: 25.3 nm, Sc/Si ratio: 0.66. Calculated using the scattering factors from CXRO. The red line identifies the laser emission wavelength of $\lambda=13.2$ nm.

Two different samples were available during the imaging campaigns. The first sample consisted of a Mo/Si multilayer coated 500 μm thick Si wafer onto which an absorption test pattern was written. The Mo/Si multilayer was centered at 13.5 nm wavelength to properly simulate an EUVL mask. A CAD diagram of this test pattern is shown in Fig. 3.8. In this sample, the lines consist of Ni has 0.1% reflectivity at 13.2 nm wavelength. The regions in between the lines consist of the Mo/Si multilayer structure,

producing an image of dark features imbedded in a bright field. The sample contained features of different size, from 300 nm half pitch down to 80 nm half-pitch. Vertical and horizontal 1:1 and 2:1 lines were available at each half pitch. Also, a series of elbow patterns of the same half pitches were available. These structures are especially useful in characterizing the amount of aberration present in the EUV images since they provide information in two orthogonal directions within the same field of view. The numbers located at the end of the features can be used to identify the pitch size under observation. The mask was printed by magnifying the pattern by a factor of two. Thus, in SEM image of Fig 3.8, the elbow pattern shown, labeled “.2”, corresponds to a half-pitch structure of 0.4 μm . The smallest features shown in the CAD drawing correspond to 50 nm and 60 nm. These patterns were not correctly developed during the manufacturing process and could not be used in the assessment of performance of the microscope, leaving the 80 nm half-pitch gratings and elbows as the smallest features.

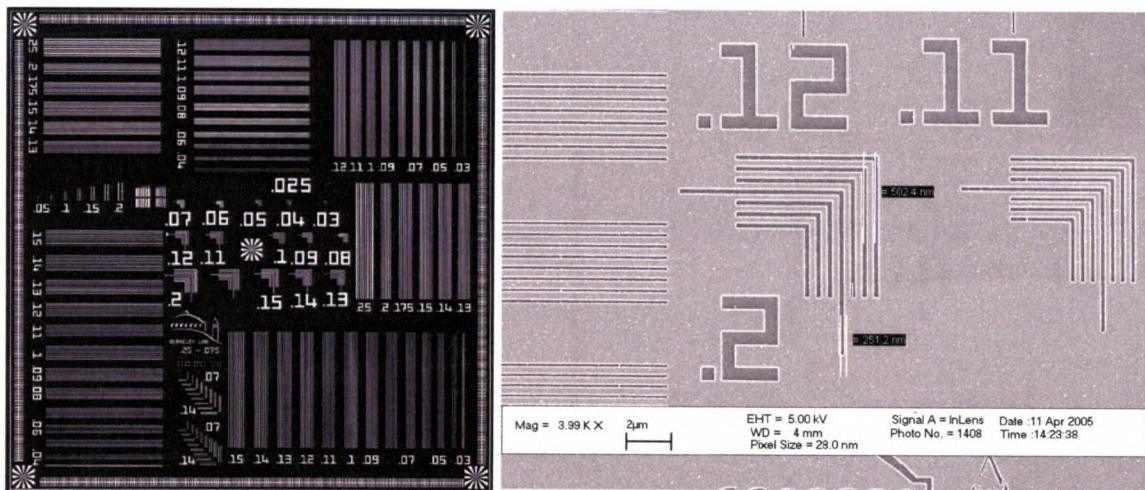


Figure 3.8: CAD drawing and SEM image of the mask test pattern. The pattern consisted of absorber pattern on a Mo/Si multilayer coated structure.

The second sample was an EUVL mask from GLOBALFOUNDRIES, Inc. It consisted of a Mo/Si coated, 6×6 in², low thermal expansion glass that contained a series of dark-field and bright-field regions with a variety of test features and extended line patterns. The features of these samples were slightly larger than the smallest features of the previews sample. The smallest grating available had a half-pitch of 125 nm. Figure 3.9 shows a picture of the mask in which the subfield can be seen in the center.

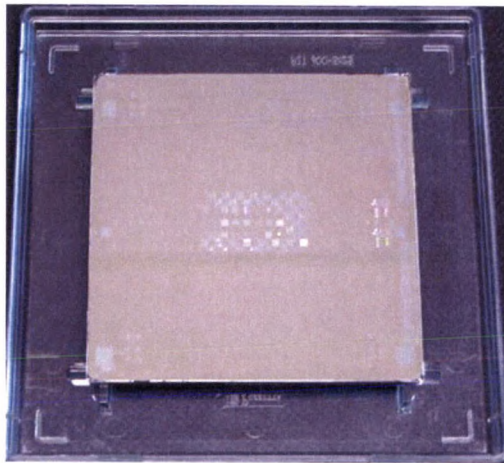


Figure 3.9: Picture of an EUVL mask. The subfields can be seen in the center of the mask.

3.6. Table-top EUV AIM: microscope operation

In this section, several aspects of the viability of the laser-based AIM microscope as well as a procedure for the microscope alignment and operation are covered. The suitability of 13.2 nm wavelength illumination for imaging Mo/Si multilayer structures centered at 13.5 nm and the throughput of the system which determines the exposure time needed for recording high quality EUV images are analyzed.

3.6.1. Suitability of 13.2 nm radiation for EUVL mask characterization

As mentioned previously, the multilayer Mo/Si mirrors that form the reflective surface of EUVL masks are designed to have peak reflectivity at $\lambda=13.5$ nm, with a bandwidth of approximately 0.6 nm. The selection of this system for EUV lithography was based the fact that Mo/Si multilayers have the highest (~70%) reflectivity of all EUV coatings. In turn, the characteristics of the optical coatings have driven the development of incoherent illumination sources at 13.5 nm wavelength based on plasmas of Sn, Li and Xe. Fig. 3.10 shows the spectra for the different prospective EUV sources compared to the total maximum theoretical reflectivity of a 11-mirror projection system [44].

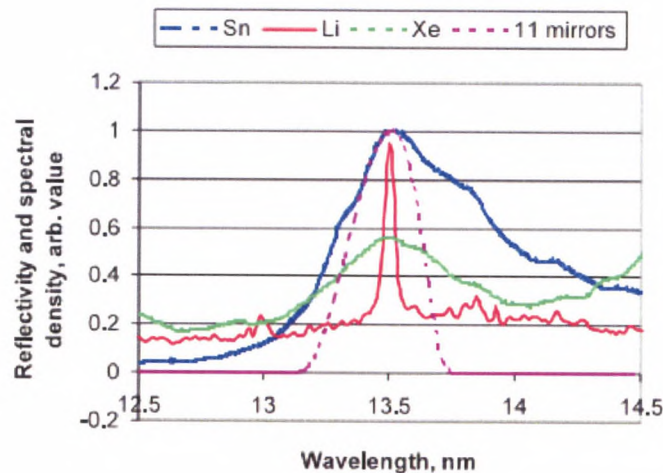


Figure 3.10: Calculated near normal incidence reflectivity of the 11 mirror system, based on the model of CXRO [11] versus spectra of Sn, Li and Xe, as acquired in a joint investigation by ASML-ISAN (figure and caption from [44]).

The multiple reflections in the optical system of an EUVL stepper produce a natural narrowing of the total bandwidth transmitted through the system. From this analysis, EUVL steppers only efficiently use a 2% bandwidth of the illumination spectrum centered at 13.5 nm, cutting out light at 13.2 nm. However, in the actinic zone plate-based microscope only the reflection off the sample's multilayer is centered at 13.5 nm for which the narrow bandwidth Cd laser has a reflectivity of about 55%.

The implications of using a monochromatic source centered at 13.2 nm for actinic mask characterization need to be thoroughly investigated to justify the validity of the EUV images for mask characterization. In EUVL masks, defects are detected by changes in the amount of reflected light or changes in the reflected phase introduced by variation of the pitch of the multilayer structure. An analysis of the effects on reflectivity and reflected phase change for multilayers of different period size is shown in Fig 3.11. This analysis shows that for a large variation of multilayer stack thickness ($\pm 10\%$ of nominal value) the reflectivity of 13.2 nm wavelength light remains sufficiently high for imaging, albeit having a greater variation compared to 13.5 nm wavelength light. This behavior shows that 13.2 nm wavelength light should have significantly higher sensitivity to detect small changes in the multilayer thickness. Regarding the reflected phase, which also contributes to intensity fluctuations due to buried defects, the simulations show that for 13.5 nm and 13.2 nm wavelength, the shifts are comparable in amplitude, suggesting that phase shifts resulting from defects in the multilayer can be efficiently picked up by the 13.2 nm wavelength light.

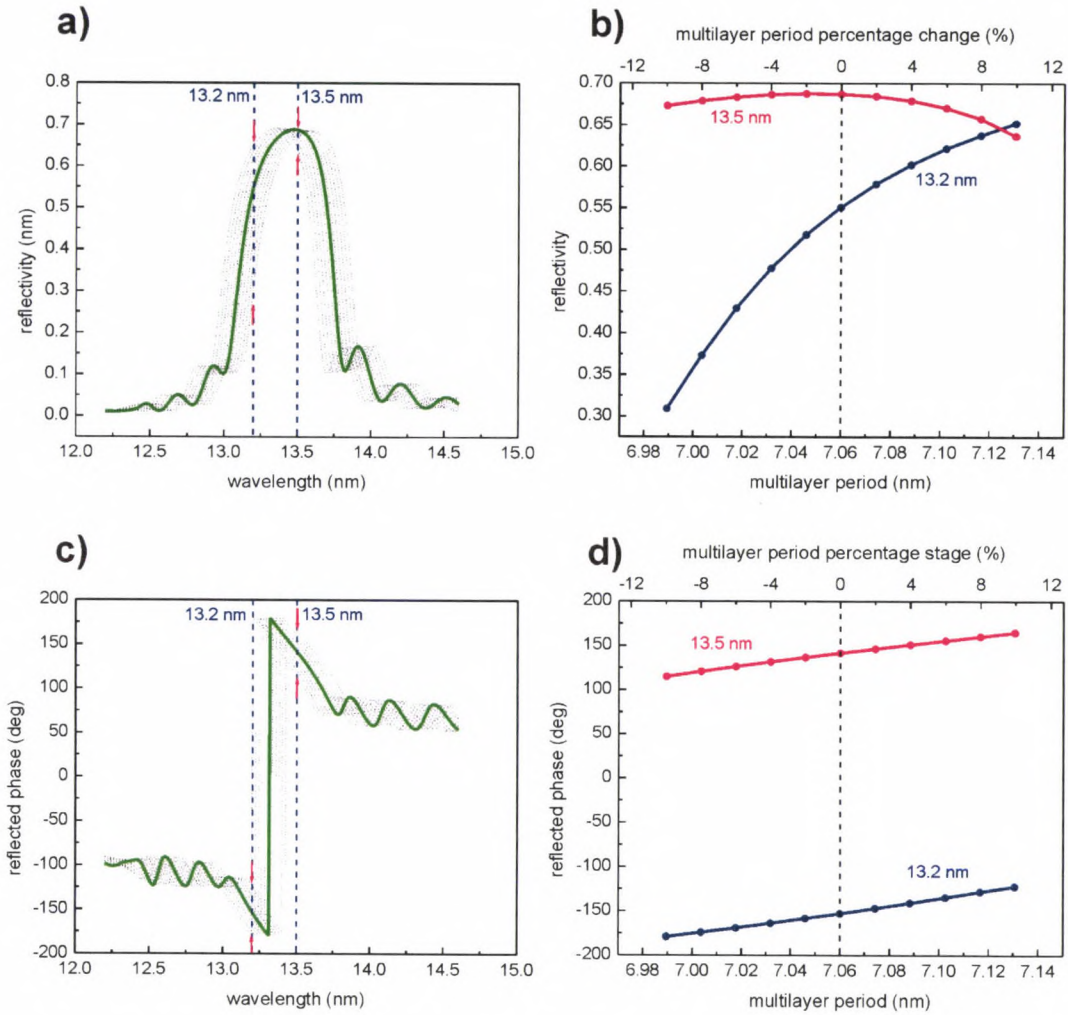


Figure 3.11: Variation of reflectivity and reflected phase as a function of multilayer period change for a typical Mo/Si reflector (calculations based on CXRO data).

3.6.2. Photon budget for image acquisition.

The image acquisition time for the $\lambda=13.2$ nm AIM microscope can be estimated by means of a photon-budget that takes into account the output of the laser and efficiencies of the different optical elements and sample. The photon budget for the microscope is presented in Table 3.1. The calculation assumes complete collection of the laser beam by the condenser and no losses arising from misalignment of the system.

Laser Power (μW)	0.5
Throughput of 0.1 μm Zr filter	0.7
Throughput of Mo/Si turning mirror	0.5
Throughput of condenser	0.05
Sample reflectivity	0.5
Throughput of (objective+window)	0.05
Total throughput of the system	4.4E-4
Output power (nW)	0.21875
Number of photons/sec	1.5E7
Diameter of beam at sample plane (μm)	20
Magnification	1080
Diameter of beam at image plane (μm)	21600
Area of the beam at image plane (μm^2)	3.7E+08
CCD pixel size (μm)	13.5
area of CCD pixel (μm^2)	182
Number of illuminated pixels	2.0E+06
Number of photons/(sec*pixel)	7
Number of counts/photon	4.4
Number of counts/(sec*pixel)	32
Exposure time for 600 counts/pixel (sec)	19

Table 3.1. Photon budget for the full-field actinic microscope for EUVL masks.

The acquisition time of an image must be such that sufficient contrast is obtained between the bright, transmissive areas and the opaque, absorptive ones. Although measurable features can usually be distinguished with count differences as little as 100, generally higher values are desired to improve the signal-to-noise ratio in the image. The photon budget suggests that the acquisition time needed to obtain a good quality image with approximately 600 counts per pixel, equivalent to 68 photons per pixel impinging on the CCD, is roughly 20 seconds.

This photon-budget assumes an average power of $0.5 \mu\text{W}$. Higher outputs of approximately $1 \mu\text{W}$ can be obtained with the laser when precise alignment conditions and high surface quality of the Cd metal target conditions are achieved.

As will be shown in the next chapter, the actual acquisition time for an image with 600 counts per pixel is approximately 90 seconds, roughly 4 times more than expected according to the photon budget. The photon budget is calculated assuming maximum theoretical efficiency values of the different components involved which may degrade with time. Also, the intensity of the beam is considered to be uniform across the condenser's diameter though in reality the beam's intensity profile is not flat. Furthermore, the budget does not take into account the motion of the condenser during image acquisition which could cut the edges of the beam and extend the illuminated area, reducing the number of counts per pixel. Nevertheless, actual exposure times are comparable to the ones used in the synchrotron-based microscopes.

3.6.3. Procedure for microscope alignment

The initial alignment of the microscope is the most time consuming. Uncertainties in the path of the EUV light can make this initial alignment challenging. To minimize setup time, a procedure for the alignment of the system was developed based on the knowledge acquired during different imaging campaigns.

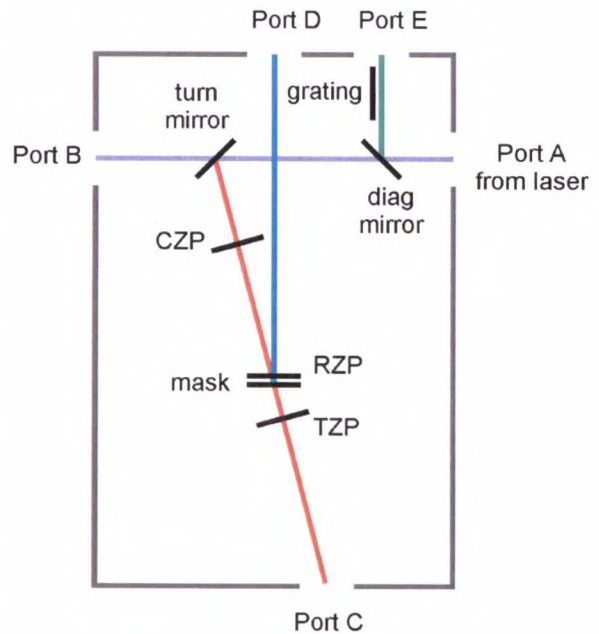
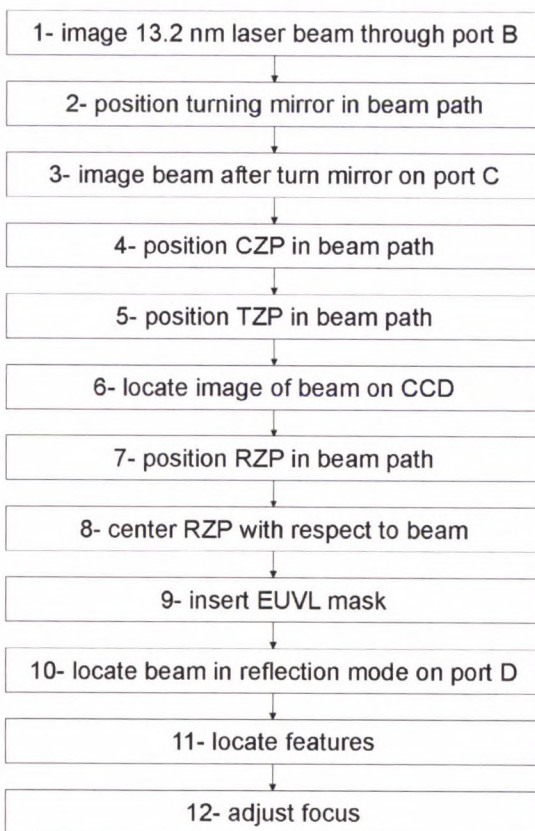


Figure 3.12: Alignment procedure chart and schematic of the microscope chamber indicating the different components and viewing ports.

Prior to fine alignment of the microscope, the entire setup is pre-aligned using a HeNe laser. This visible laser is first centered to the entrance port of the microscope chamber (Port A in Fig. 3.12) and to a port located on the opposite wall of the vacuum chamber (Port B in Fig. 3.12). Then, all the optical components are placed inside the chamber and aligned to the visible laser, starting with the turning mirror, and continuing with the other elements along the beam path. Once the system is pre-aligned, the optical elements are removed from the beam path using encoded steppers and the fine alignment is done using the EUV laser following the steps enumerated in the flow chart shown in Fig. 3.12.

The first step is to check the output of the EUV laser. By installing the EUV-sensitive CCD in the side port of the microscope's chamber (Port B in Fig. 3.12), a far field image of the beam can be obtained. The location of the beam with respect to the center of the CCD, and thus the center of the port, can be controlled by moving a grazing incidence mirror located at the output of the laser in the laser chamber. Figure 3.13.1 shows the far field image of the beam obtained with a single laser shot. Due to the high intensity of the beam, filtering might be needed to avoid saturation of the CCD. Once the beam has been located and centered on the CCD, the microscope's turning mirror (*turn mirror*) can be placed in the beam path (step 2).

The following steps take advantage of the simplicity of aligning a microscope for transmission imaging. With the CCD located in the port for transmission imaging (Port C in Fig. 3.12), first a far field image of the beam must be obtained to ensure adequate positioning of the turning mirror (step 3). The picomotors on the turning mirror's mount can be used to center the beam on the CCD.

Step 4 is to place the condenser zone plate (*CZP*) in the beam path. Figure 3.13.2 shows a projection of the condenser located in the beam path. In this image some beam structure can be seen along with a bright spot in the center of the lens that will be the reference point on the CCD for the next steps.

In step 5, the transmission mode zone plate (*TZP*) must be placed in the beam path by positioning the center of its projection onto the reference point determined in the previous step. If the projection can not be easily located, the *CZP* can be moved out of the way to increase the light on the *TZP*. Figures 3.13.3 and 3.13.4 show the *TZP* positioned in front of the beam. Depending on the amount of light available, the 0th order light from the condenser can be seen, as shown in Fig. 3.13.4, obtained with a condenser zone plate with a large central stop.

If the imaging beam is not immediately found in step 5, the location of the *TZP* must be scanned until the beam appears on the CCD (step 6). The size of the beam depends on *CZP-TZP* distance and can be adjusted as needed. Images of the beam are shown in Fig. 3.13.5 and 3.13.6.

If the microscope is going to be used for transmission mode imaging, the only further steps are to introduce the sample in the object plane and adjust the focus. For reflection mode imaging, the next step (step 7) is to introduce the reflection mode zone plate (*RZP*) in the path of the beam as shown in Fig. 3.13.7. The off-axis *RZP* has a semitransparent area of approximately 0.5 mm × 0.5 mm and its unique design creates a distinct far field pattern as can be seen in Fig. 3.13.7. The *RZP* should be adjusted until the beam is centered in this region as shown in Fig 3.13.8 (step 8).

In step 9, the reflection mask is inserted in the beam path as close to the object plane of the system as possible. Due to the high magnification of the microscope, the object plane is very close to the focal plane of the *RZP*, approximately 1 mm. The positioning of the mask can be done by looking at the system from above with a magnifying viewer. Once the sample is in place the CCD should be relocated to the port for reflection mode imaging (Port D in Fig. 3.12).

The off-axis design of the zone plate removes most of the 0th order of the condenser from the field of view of the CCD. However, depending on the alignment, some of the 0th order might be visible on the edge of the CCD. If available, this can be used as an indication that the alignment is not far off.

To find the beam, the *RZP* should be scanned within a 0.5 mm × 0.5 mm area in steps of approximately 30 μm (step 10). Usually, the beam is found very close to the initial position but this will vary with the accuracy used in step 8. An image of the beam in reflection mode is shown in Fig. 3.13.9. If the beam is not found, the output of the laser should be checked and steps 8 and 9 might need to be repeated.

Once the beam is located it should be straight forward to locate features on the mask (step 11) and adjust the focus (step 12). The microscope should produce an image like the one shown in Fig 3.13.10 in which a set of focused features can be seen. In this case the image was obtained with 30 laser shots.

Once the system is aligned, the output of the EUV laser can be monitored by inserting the diagnostic mirror (*diag mirror*) in the beam path. This Mo/Si mirror guides the EUV laser onto a grating that allows seeing the spectrum of the light on a CCD

detector located on port E. This diagnostic arm is useful to evaluate the output energy of the laser at any time during the experiment.

The results presented in the next chapter were obtained after aligning the microscope using this procedure.

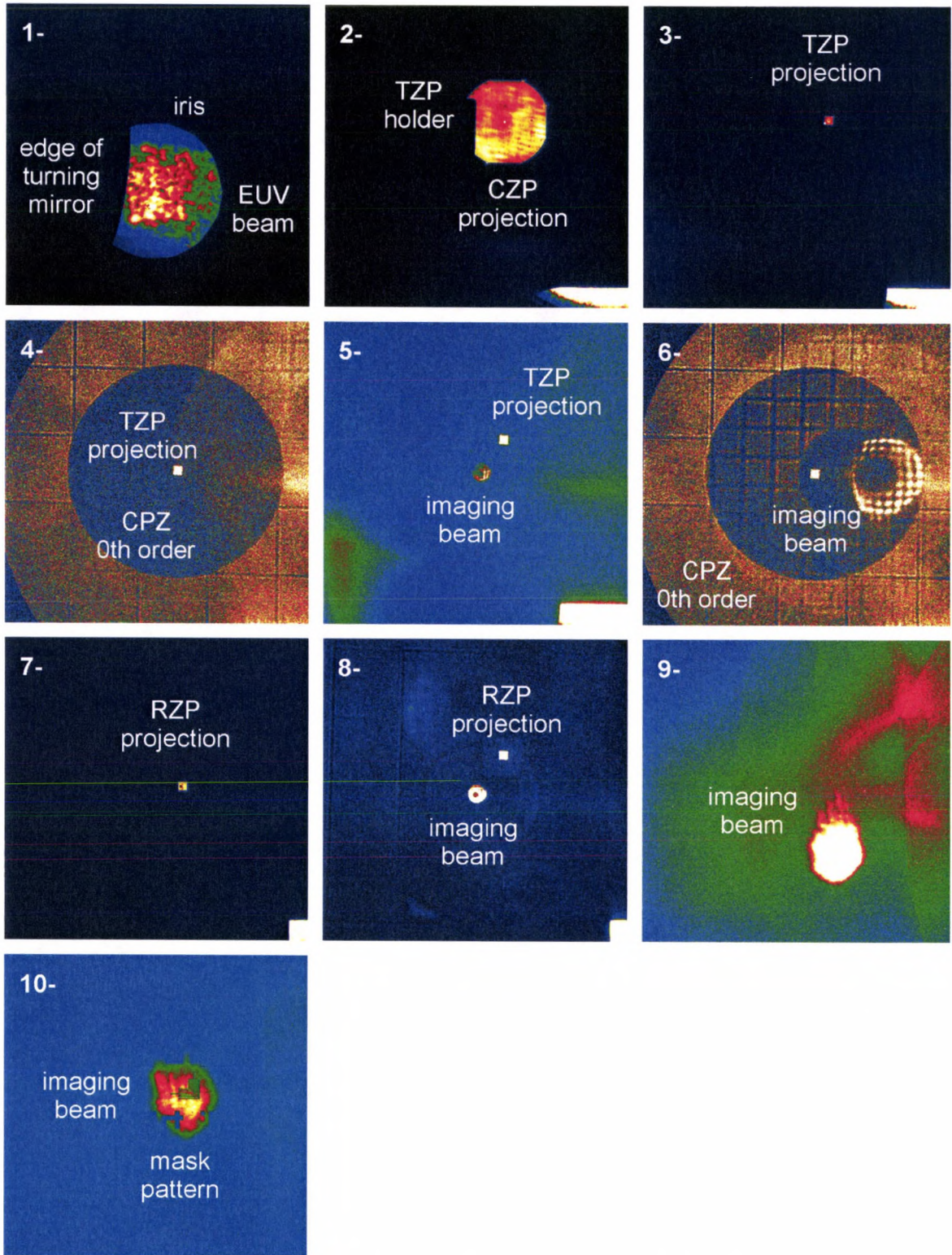


Figure 3.13: EUV images showing the different stages of the alignment procedure, starting from EUV beam location to EUVL mask imaging. The use of the transmission mode zone plate is crucial in simplifying the alignment of the system.

CHAPTER 4: Results

4.1. Introduction

The experimental results are presented in two sections. The first section is dedicated to the characterization of the microscope. The microscope was characterized by evaluating its spatial resolution as well as its illumination characteristics through uniformity and the illumination's partial coherence. Since the microscope was designed to mimic the imaging conditions of a 0.25 NA, 4 \times -demagnification, EUVL stepper, the results obtained are compared to the expected performance of this tool.

The second section presents the characterization of patterns on an EUVL mask from GLOBALFOUNDRIES, Inc. Parameters such as line-edge-roughness and normalized-intensity-line-slope were measured on different gratings structures to illustrate the ability of the microscope to evaluate EUVL masks.

The results presented in this chapter have resulted in the publication of two articles in peer-reviewed journals, as well as several conference presentations and proceedings which are listed in Chapter 7.

4.2. Characterization of the microscope

4.2.1. Resolution measurements

The resolution of the EUV AIM microscope was evaluated during the first imaging campaign using a combination of different measurements.

The techniques described in Chapter 1 were used to evaluate the spatial coherence of the system. First, the modulation in intensity of EUV images of grating patterns of decreasing half-pitch was analyzed. The sample containing elbow patterns as small as 80 nm half-pitch, described in the previous chapter was used. Figure 4.1 shows EUV images of the 140 nm, 120 nm, 100 nm, and 80 nm half-pitch elbow structures along with their respective intensity cross-sections (lineouts). These images were obtained using exposure times of 20 seconds with the laser operating at a repetition rate of 5 Hz. The images have a field of view of $\sim 5 \times 5 \mu\text{m}^2$, limited by the size of the illumination beam. They were taken with a magnification of $\sim 610\times$ at which each pixel on the CCD corresponds to 22 nm in the sample plane. This magnification was selected to allow approximately 8 pixels per period in the smallest structures available.

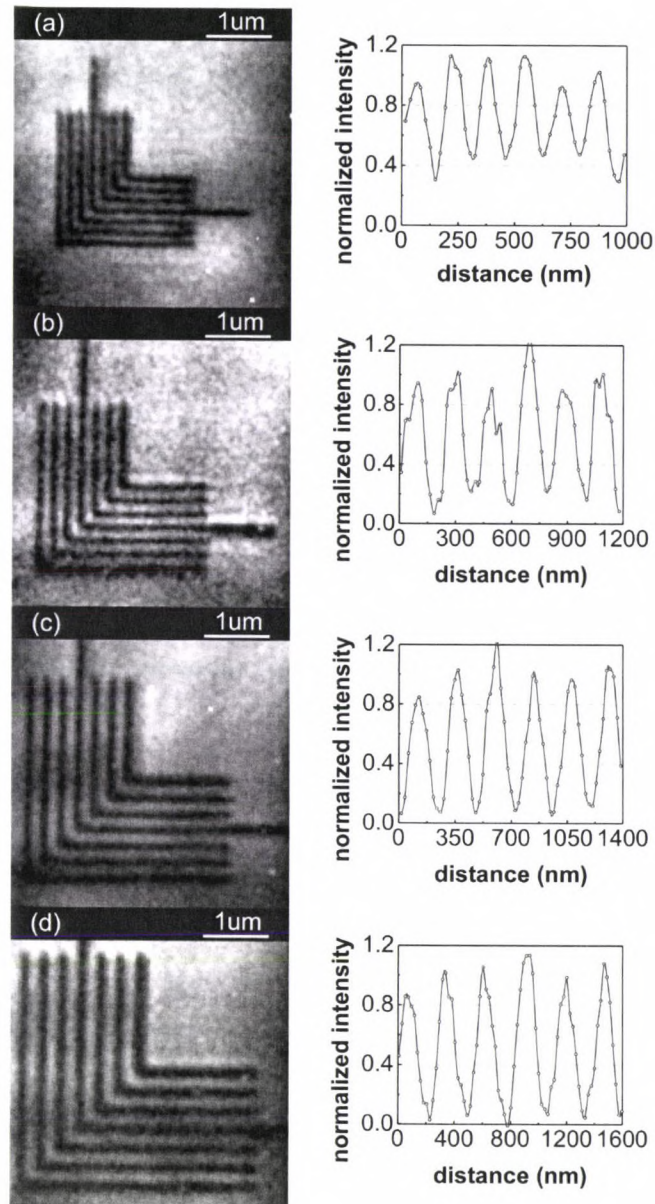


Figure 4.1: Actinic image and corresponding intensity cross section for elbow patterns of a) 80 nm half-pitch, b) 100 nm half-pitch, c) 120 nm half-pitch, and d) 140 nm half-pitch on the mask. The images were obtained with an exposure time of 20 seconds and a magnification at the CCD plane of $\sim 610\times$. The lineouts indicate that the features are fully resolved.

The intensity cross-sections of each image were evaluated in the two orthogonal directions. To obtain the lineouts, five rows of pixels, perpendicular to the gratings were averaged. This process was repeated several times along the vertical and horizontal lines of each image. Figure 4.2 shows six different cuts taken on the horizontal lines of the 140 nm half-pitch elbow. The different lineouts show very small variation.

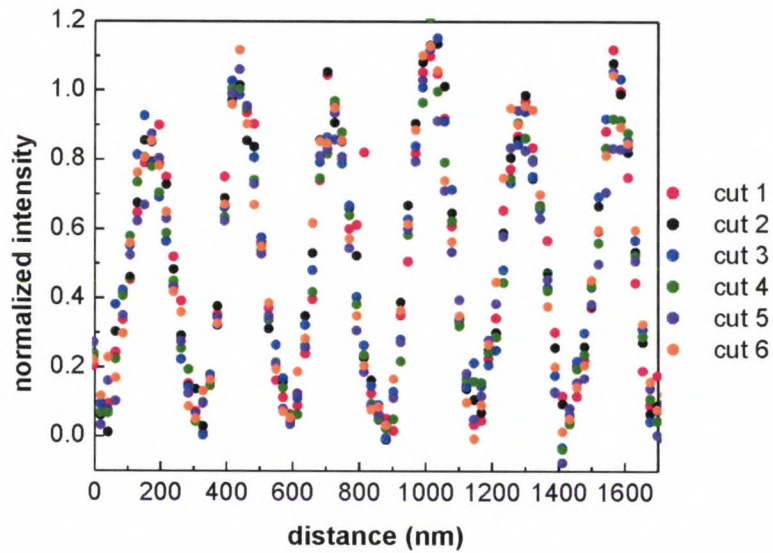


Figure 4.2: Intensity lineouts obtained from the horizontal grating of the 140 nm elbow pattern of Fig. 4.1.d.

The modulation of the lineouts was obtained using:

$$M = \frac{I_{\max} - I_{\min}}{I_{\max} - I_{\text{bg}}} \quad (\text{Eq. 4.1})$$

where I_{\max} , I_{\min} , and I_{bg} are the intensity values, or CCD counts of the peaks, the valleys and the background, respectively. The modulation value was obtained for each of the intensity lineouts of the vertical and horizontal lines for the four elbow patterns. The average modulation values found for each pattern are listed in Table 4.1.

Half-pitch (nm)	Modulation
140	0.96 ± 0.02
120	0.93 ± 0.04
100	0.87 ± 0.04
80	0.66 ± 0.08

Table 4.1: Intensity modulation values for half-pitch structures of 140 nm, 120 nm, 100 nm and 80 nm.

Recalling that the Rayleigh criterion states that the features are spatially resolved if the modulation is above 26.5%, all gratings imaged are fully resolved. This indicates that the spatial resolution of the microscope is well below 80 nm half-pitch.

To estimate the spatial resolution of the system in the absence of smaller grating structures, a knife-edge test was performed across a large absorber feature. Figure 4.3 shows the intensity lineouts across the EUV image shown in the insert. The image was obtained under the same conditions as the images shown in Fig. 4.1. As before, the lineouts were obtained by averaging five consecutive rows of pixels. Four lineouts were obtained at different positions of the image. The measurements yielded a 10% to 90% transition of $\sim 110 \pm 5$ nm.

Because the illumination of the source is partially coherent, the knife edge test could not be directly correlated to the results obtained using the grating structures. To overcome this limitation, the spatial resolution of the microscope was independently measured by analyzing the EUV images of Fig. 4.1 with a correlation method that performs a global assessment of an EUV image and returns a spatial resolution value for the image [87]. This method, developed in our group by P. Wachulak, estimates the

spatial resolution by evaluating the correlation between a raw EUV image and a series of computer generated templates with decreasing resolution. These templates are constructed applying different Gaussian filters to a master binary template constructed from the original image. The only required input parameter to the analysis is the microscope's magnification which determines the size of the pixel in the image.

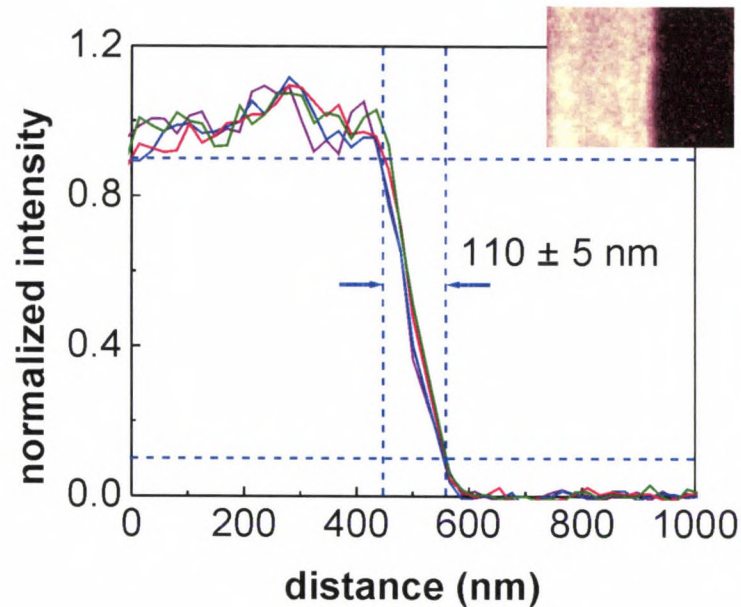


Figure 4.3: Intensity cross-section along the EUV image shown in the insert. The 10% to 90% intensity transition is 110 ± 5 nm.

Figure 4.4 shows the resulting correlation map obtained by applying this method to the EUV image of the 120 nm half-pitch elbow structure shown in Fig. 4.1. The color map indicates the correlation level of a specific template with the original image. The spatial resolution is given by the highest correlation for the specific feature size. Applying this correlation method to the EUV images of Fig. 4.1, a half-pitch resolution of 53 ± 10 nm was obtained.

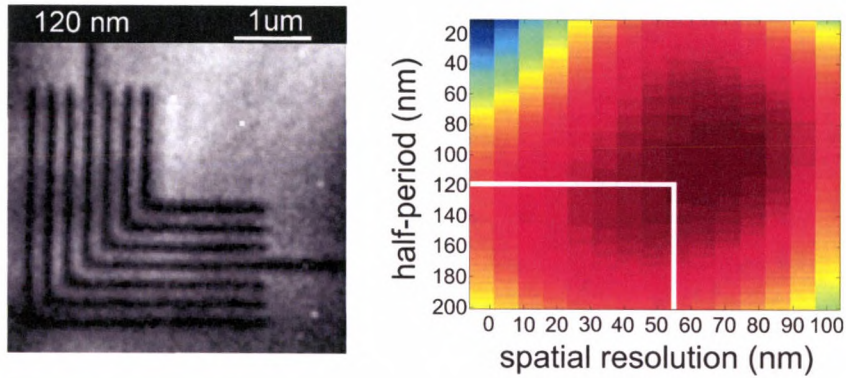


Figure 4.4: EUV image of a 120 nm half-pitch elbow structure and correlation map indicating that the resolution of the microscope is approximately 55 nm.

The Modulation Transfer Function (MTF) of the microscope, which gives a measure of the ability of the microscope for transferring different spatial frequencies, was constructed using the intensity modulation data obtained from the images of Fig. 4.1 along with the results correlation test. These two results could be combined because the correlation method provides a resolution value that is independent of the coherence of microscope.

As shown in Fig. 4.5, the modulation starts to roll off for structures smaller than 120 nm, in agreement with simulations for a 0.0625 NA objective under partially coherent illumination. The dashed line was added to guide the eye.

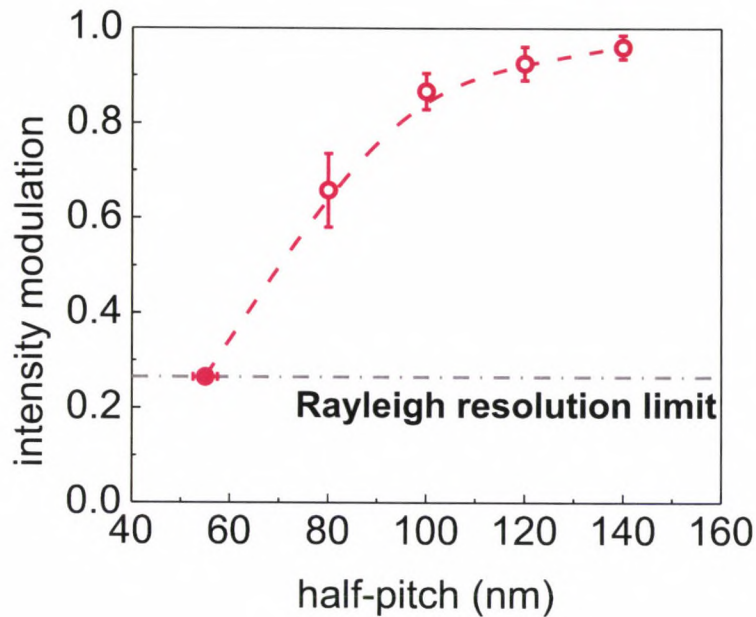


Figure 4.5: Modulation Transfer Function for the 13.2 nm microscope. The MTF was constructed using the line-outs from the images of Fig. 4.1 (open circles) and the results of the correlation method (full circles).

4.2.2. Illumination and coherence characterization of the microscope

The images shown in Fig 4.1 have high non-uniformities in intensity. These variations in intensity are detrimental to image analysis. This limitation was overcome by replacing the condenser zone plate with one featuring a smaller central stop, as described in the previous chapter. Also, an XY piezoelectric stage was added to the condenser to slightly scan the illumination during image acquisition. Figure 4.6 shows a comparison between images of the beam before and after the improvements to the system. As seen in Fig. 4.6.a, using a zone plate condenser with central stop creates an annulus, limiting the area of illumination. The grid-like structure present in the image is due to alignment

mismatch during the electron beam writing process of the condenser zone plate. By contrast, as shown in Fig. 4.6.b, the condenser zone plate with no central stop forms a circular illumination area. Also, in this particular case, better overlap in the e-beam writing of the lens reduced significantly the appearance of the grid pattern shown in Fig. 4.6.a. Variations in the beam intensity distribution are further reduced by scanning the condenser during the acquisition of the image.

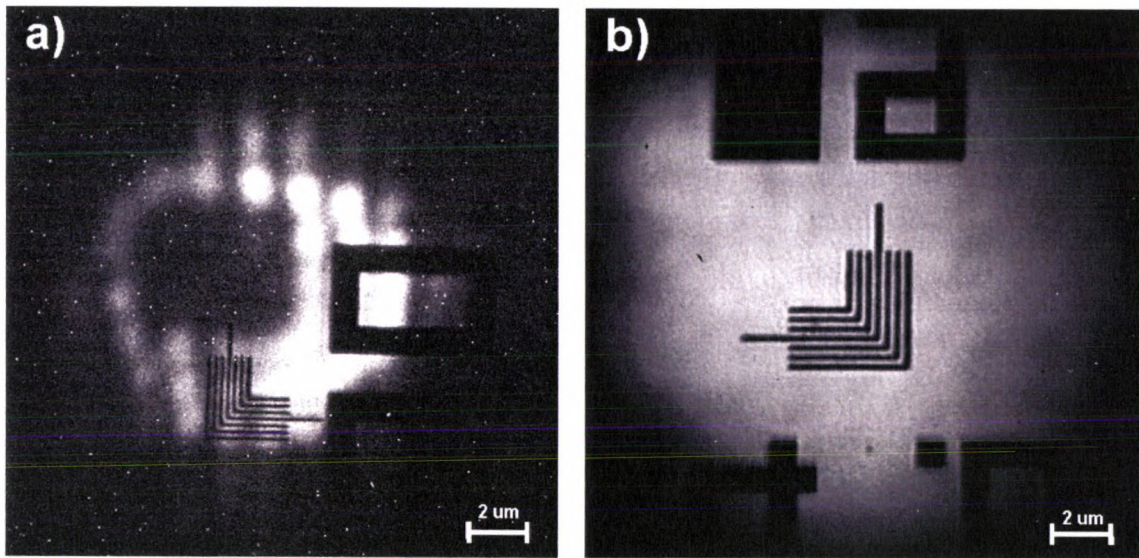


Figure 4.6: a) EUV image of the illumination during the first imaging campaign. b) EUV image of the illumination after the upgrades to the condenser.

Figure 4.7 shows in detail the 180 nm half-pitch elbow absorption pattern of Fig. 4.6.b. The image was obtained with an exposure time of 90 seconds with the laser operating at a repetition rate of 1 Hz. A slightly larger magnification of 660 \times was used, resulting in an equivalent pixel size of approximately 20 nm. The image shows a \sim 10% variation in intensity in the central 4 \times 4 μm^2 region of the field of view. The speckle features seen in the bright areas of the image arise from the roughness of the Mo/Si

coating on the mask [88]. Although an exposure time of 90 seconds is necessary to achieve the high quality images necessary for mask pattern analysis, exposure times as short as 5 seconds are used for feature location.

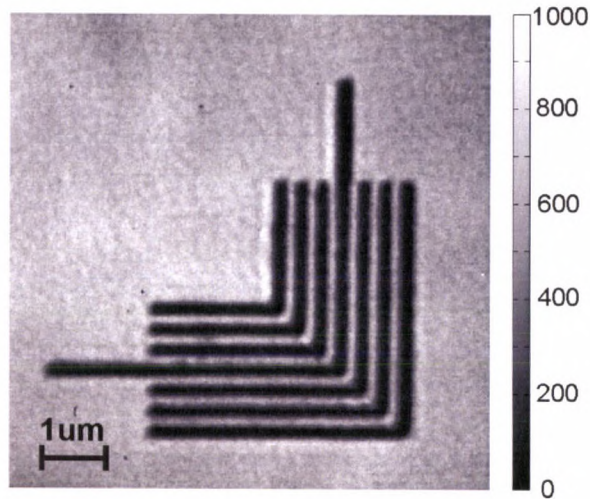


Figure 4.7: EUV image of a 180 nm half-pitch absorption elbow pattern in a bright field obtained with an exposure of 90 seconds. The color bar indicates the number of counts per pixel.

The degree of coherence, evaluated through the coherence parameter, m , of the table-top actinic microscope was evaluated by analyzing the through-focus performance of a 200 nm half-pitch grating as described in Chapter 1. The defocused images were obtained by moving the objective zone plates in steps of $\sim 2.5 \mu\text{m}$ through the focal plane of the system. Figure 4.8 shows five images obtained at different positions from the best focus. These images were obtained with the same exposure and magnification as the one shown in Fig. 4.7.

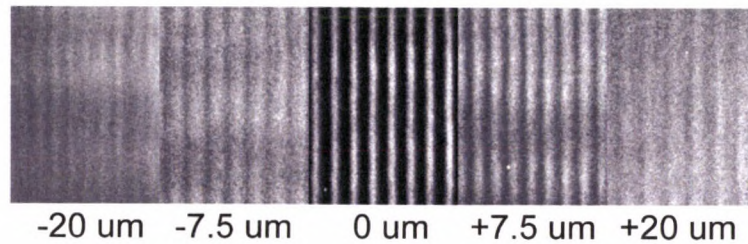


Figure 4.8: EUV images of a 200 nm half-pitch grating pattern in a dark field obtained with an exposure of 90 seconds. The central image was obtained at best focus. The numbers in the bottom indicate the distance from best focus.

For each image, intensity lineouts were obtained by averaging 5 rows of pixels, in a similar fashion to the measurements of resolution described above. From these lineouts the modulation of the intensity for each image was obtained. The through-focus analysis was performed twice and the results for each position were averaged. As shown in Fig. 4.9, the appearance of secondary maxima as far as 25 μm away from the focal plane reveals the system's partial spatial coherence. A comparison with simulations using SPLAT [89] indicates that the coherence parameter for the microscope is $m \sim 0.25$. This value is lower than the value of 0.5 of a 4 \times EUVL stepper [70], but higher than that of current synchrotron-based microscopes for mask inspection that operate in a higher coherence regime ($m = 0.1\text{--}0.2$) [71, 90].

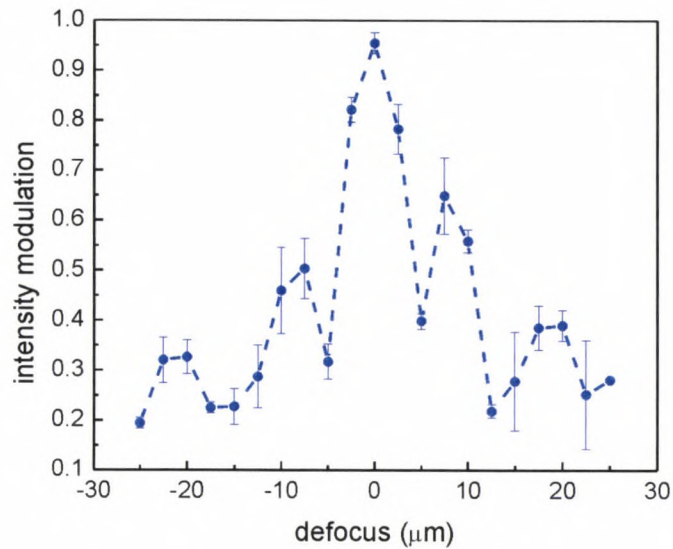


Figure 4.9: Normalized modulation intensity of a bright-field EUV image of a 200 nm half-pitch grating at different positions from the focal plane. The intensity of the secondary maxima reveals a partial spatial coherence of approximately $m \sim 0.25$, as simulated using SPLAT.

4.3. EUV image analysis for the characterization of patterns

EUV images from the GLOBALFOUNDRIES EUVL mask were used for pattern characterization. Figure 4.10 shows an EUV image of horizontal and vertical 175 nm half-pitch 1:1 gratings located in one of the mask dark-field subfields. The image was obtained under the same conditions as the image of Fig. 4.7. The image clearly shows that both sets of lines are fully resolved and no discernable astigmatism is present.

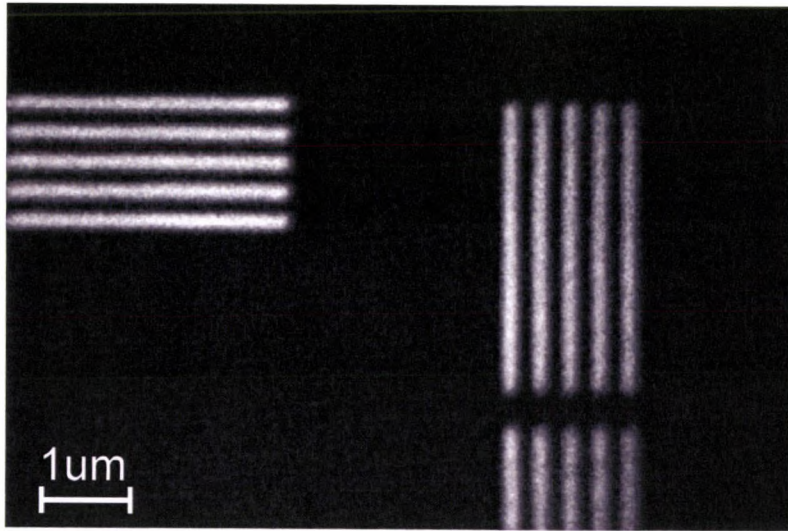


Figure 4.10: EUV image of 175 nm half-pitch gratings in a dark field.

The EUV image of Fig. 4.10, along with one of 225 nm half-pitch gratings were used to measure NILS and LER. To obtain these parameters, the images (Fig 4.11.a and 4.11.d) were normalized in intensity and for each an intensity threshold corresponding to the normalized intensity value for which the lines and spaces have a 1:1 ratio was obtained. These thresholds are 0.40 and 0.42 for the 175 nm and the 225 nm half-pitch gratings respectively. The averaged normalized intensity plots and intensity thresholds, for both images are shown in Fig. 4.11.b and 4.11.e. NILS values were measured at the intensity threshold for each slope of the averaged cross-sections. LER for each line was measured by evaluating the magnification-corrected location of the occurrence of the intensity threshold for each pixel row of the images. The standard deviation of these values was subsequently calculated for each edge. The measurements were performed across the central 1 μm region of the gratings. Figures 4.11.c and 4.11.f show the resulting plots. In each case, the LER value is below 10% of CD ($LER/CD < 0.1$). The results of the NILS and LER analysis are summarized in Table 4.1.

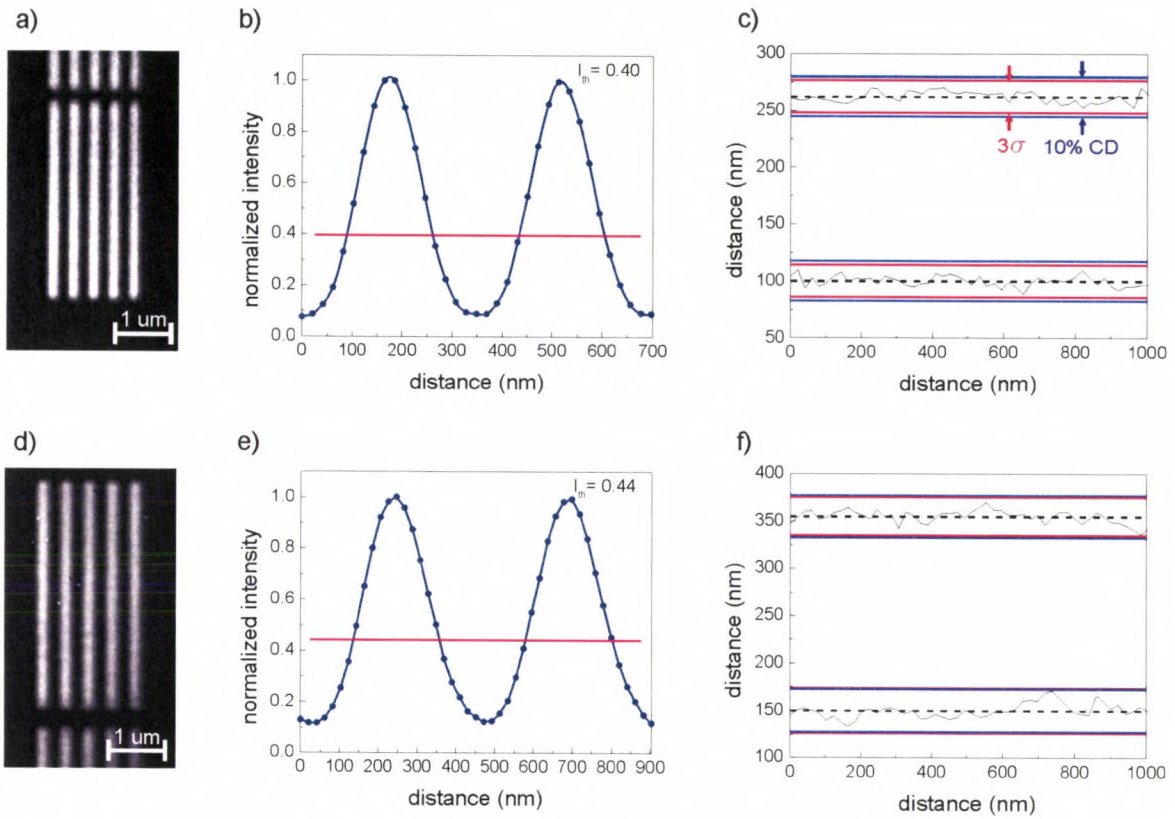


Figure 4.11: LER analysis of a) 175 nm and d) 225 nm half-pitch gratings. Normalized intensity versus position plots are given in b) and c). e) and f) provide a graphical representation of the variation of the edge position along the features. The analysis shows that the 3σ variation is below 10% of the CD value.

CD (nm)	I_{th}	NILS	LER (nm)	LER/CD
175	0.395	3.58	13.55	0.078
225	0.442	3.32	20.86	0.093

Table 4.1: NILS and LER measurements of two gratings with indicated CD values.

CHAPTER 5: Summary and future work

For the last decade the semiconductor industry has been developing extreme ultraviolet lithography to replace current lithographic techniques as these reach their limit in minimum printing size. The absorptive nature of EUV light has required a novel approach to the development of the printing systems, and has resulted in a number of technological challenges from the development of sufficiently high output power sources to the availability of high quality multilayer-coated mirrors and mask with high reflectivity at the printing wavelength. Although most of these issues have been successfully resolved, as insertion of extreme ultraviolet lithography for high-volume manufacturing of semiconductor chips approaches, the need for reliable and convenient imaging tools for mask characterization has risen to one of the main concerns for the industry.

Current full-field microscopes devoted to the characterization of EUVL masks are few in number and are based on synchrotron radiation, making them not suited for industrial settings. To address this critical need, we have developed the first laser-based, compact, actinic aerial image microscope for EUVL mask characterization.

The full-field microscope, developed at Colorado State University, uses as its illumination the output of a table-top EUV laser that emits at a wavelength of 13.2 nm, well within the reflectivity bandwidth of the Mo/Si coatings of EUVL masks. A set of zone plate optics are used to mimic the printing conditions of a 0.25 NA 4×

demagnification EUVL stepper. The microscope can handle standard 6×6 in² EUVL masks and is housed in a $70 \times 45 \times 40$ cm³ vacuum chamber. The entire system, including the illumination source occupies 4 optical tables.

The spatial resolution of the microscope, 55 nm, was evaluated according to the Rayleigh criterion. Images with this resolution were obtained using exposure times as short as 5 seconds. The measured modulation transfer function of the microscope corresponds to that of a system operating under partially coherent illumination. A partial coherence parameter, m , of 0.25 was obtained by comparing the through-focus response of a grating sample to simulated data. This value is lower than that expected for a 0.25 NA stepper ($m=0.5$) but comparable to the coherence of synchrotron based microscopes ($m=0.2$).

The actinic characterization of EUVL masks relies on the uniformity of the illumination of the microscope. Great efforts were taken to obtain uniform illumination of the masks, with variations below 10% in the central region of the image. This, along with the intensity in the image plane, has enabled the measurement of key parameters of mask pattern printability such as line-edge roughness and intensity log-slope on an EUVL mask from GLOBALFOUNDRIES in which values of LER of less than 10% CD were obtained.

Several upgrades can be made to the system to improve the illumination conditions and the spatial resolution. Although the results presented in this dissertation were obtained with an objective zone plate with a numerical aperture of 0.0625 that mimics a 0.25 NA EUVL stepper, off-axis objectives with higher numerical apertures can

be used to mimic higher resolution steppers. Off-axis zone plates that mimic 0.35 NA steppers can be readily made using conventional e-beam lithographic techniques [90].

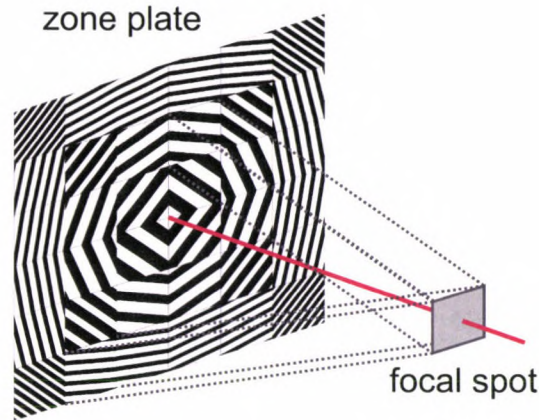


Figure 5.1: Beam-shaping condenser lens. The size of the areas on the zone plate define the area of the beam at the focal spot.

Regarding the illumination uniformity, it can be further improved by replacing the condenser zone plate for a focusing mirror or a beam-shaping condenser. A mirror has the advantage of increased efficiency compared to zone plates, but would require a second turning mirror located after the objective to collect the image due to the size of the substrate. Replacing the condenser for a beam-shaping one would require no additional changes to the layout of the microscope. A beam-shaping condenser produces uniform illumination at the focal distance by tiling the zone plate with regions of constant-pitch gratings [91, 92]. A diagram of a beam shaping zone plate that produces a square illumination spot is shown in Fig. 5.1.

For the EUV microscope we have designed a zone plate following this approach. This zone plate, composed of 15 μm wide concentric rings with gratings of constant pitch

is designed to produce a 15 μm diameter flat-top beam at a distance of 38 mm, while maintaining the numerical aperture of the original condenser

To design the zone plate, a simple algorithm based on the diffraction equation for a constant period grating (Eq. 5.1), was written to calculate zones of the grating given the initial parameters of diameter of the zone plate, diameter of the central stop, desired working distance, size of the spot at the sample plane, and wavelength of illumination.

$$d(\sin \theta_m + \sin \theta_i) = m\lambda \quad (\text{Eq. 5.1})$$

In this equation, d is the period of the grating, θ_m is the diffraction angle relative to normal for the m^{th} diffraction order, θ_i is the incidence angle on the grating, and λ is the illumination wavelength. If normal incidence light is considered the equation for the first diffraction order can be written as:

$$d(\sin \theta) = \lambda \quad (\text{Eq. 5.2})$$

This equation along with the desired geometry of the zone plate is used in the algorithm that calculates the grating period for each ring in the zone plate. The output of the algorithm is used to simulate the performance of the lens and as the input for the e-beam nanowriter in the production stage. For example, the 5 mm \times 5 mm zone plate proposed, with a central stop of 200 μm , a working distance of 38 mm, designed for 13.2 nm wavelength to produce a spot size of 15 μm at the sample plane will consist of 164 concentric rings patterned with constant pitch gratings ranging from 1.4 μm in the inner ring to 100 nm in the outer ring.

Apart from improving the uniformity of the light, the transmission of a zone plate can be greatly improved by replacing the opaque zones by phase shifting ones. This was proposed by Rayleigh in 1964 and implemented by Woods in 1898 [93]. In these phase

plates, a phase shifting material is used in place of the absorbing rings in order to retard the phase of the incidence light by π radians. The shift between different zones causes the undiffracted light to interfere destructively, increasing the amount of energy in each of the diffracted orders. Because at EUV wavelengths all materials present high imaginary components of the index of refraction, and a real part of the index of refraction $(1-\delta)$, which gives rise to the phase shift, approaching unity; it is not possible to build a genuine Rayleigh-Wood zone plate. Nevertheless, by carefully selecting materials with low imaginary component of the index of refraction and high δ component to the real part, zone plates with higher efficiency in the first diffraction order can be made. Using this concept, zone plates based on molybdenum with an efficiency of approximately 20% in first order can be realized. By implementing this new zone plate and forecasting improvements in the laser output following improvements to the source, exposure times as short as single shots could be expected.

Although these changes will significantly improve the performance of the microscope, its current stage allows for routine evaluation of EUVL masks. One evaluation that is commonly carried out using synchrotron-based systems is that of printability of programmed phase defects.

As mentioned in Chapter 2, a main concern in EUVL mask production is the appearance of phase defects arising from thickness variations in the multilayer coating that can be imaged onto the silicon wafers. Because the phase defects arise from the interaction of the EUV light with the multilayer coating, non-actinic techniques cannot be used for these measurements. . Test masks that are made by deliberately adding defects of a known size to the sample substrate at known positions before the multilayer

deposition are used to assess levels of defect printability. To control the height of the defect, each layer of the mirror is smoothed before the next one is deposited. The defects can thus be arranged in a matrix in which their size is varied. Alternatively they can be located below absorber patterns to study their influence on the imaging process of different features such as in a study performed with the AIT at Berkeley (Fig 5.2) [49]. Similar studies can be performed using the microscope at Colorado State University. Furthermore, comparisons between images obtained with different actinic microscopes could be carried out to further investigate the effects of printability as a function of tool performance.

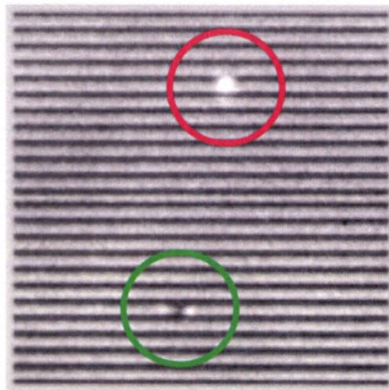


Figure 5.2: Actinic inspection tool image of a programmed embedded defect on a 160 nm half-pitch grating. Red circle: absorber marker used to locate the phase defect. Green circle: embedded 11.9 nm high phase defect. From [49].

In summary, the microscope presented in this dissertation constitutes the first stand-alone actinic EUVL mask metrology system. To exploit the capabilities of the microscope, partnerships with mask, tools, and chip manufacturers will be critical. It is foreseen that initial collaborations with key industrial partners will spark interest in this microscope, opening the path for the development of practical full-field metrology

systems that can be implemented on-site at printing facilities. Furthermore, the optical design presented can be readily adapted to EUV laser sources at other wavelengths to study other systems of technological and scientific interest.

CHAPTER 6: Papers and presentations

The work presented in this dissertation was possible due to the efforts in EUV imaging using compact laser undertaken at Colorado State University within the efforts of the NSF Center For Extreme Ultraviolet Science and Technology. The work presented here and the research that led up to these developments has resulted in a large number of publications in peer-reviewed journals as well as numerous presentations in conferences and meetings detailed next.

Since 2003, our group has pioneered the implementation of full-field microscopes that use EUV lasers as their illumination source. These wavelength-scalable microscopes operate between 47 and 13 nm wavelength. One of these microscopes that can image nanostructures with a single laser shot was identified by R&D Magazine as one of the most significant technological developments in 2008, and received an R&D100 award.

Peer-reviewed publications

1. **F. Brizuela**, S. Carbajo, A. Sakdinawat, D. Alessi, D. H. Martz, Y. Wang, B. Luther, K. A. Godberg, I. Mochi, D. T. Attwood, B. La Fontaine, J. J. Rocca, C. S. Menoni, “Extreme Ultraviolet laser-based table-top aerial image metrology of lithographic masks”, *Optics Express*, **18**, No. 14, 14467-14473 (2010).
2. **F. Brizuela**, Y. Wang, C. A. Brewer, F. Pedaci, W. Chao, E. H. Anderson, Y. Liu, K. A. Goldberg, P. Naulleau, P. Wachulak, M. C. Marconi, D. T. Attwood, J. J. Rocca, and C. S. Menoni, “Microscopy of extreme ultraviolet lithography masks with 13.2 nm table-top laser illumination”, *Optics Letters*, **34**, No. 3, 271-273, (2009).

3. P. W. Wachulak, C. A. Brewer, **F. Brizuela**, C. S. Menoni, W. Chao, E. H. Anderson, R. A. Bartels, J. J. Rocca, and M. C. Marconi, "Analysis of extreme ultraviolet microscopy images of patterned nanostructures based on a correlation method," *Journal of the Optical Society of America B*, **25**, Issue 7, pp. B20-B26.
4. C.A. Brewer, **F. Brizuela**, P. Wachulak, D.H. Martz, W. Chao, E.H. Anderson, D.T. Attwood, A.V. Vinogradov, I.A. Artyukov, A.G. Ponomareko, V.V. Kondratenko, M.C. Marconi, J.J. Rocca, and C.S. Menoni, "Single shot extreme ultraviolet laser imaging of nanostructures with wavelength resolution," *Optics Letters* **33**, 518 (2008).
5. G. Vaschenko, **F. Brizuela**, C. Brewer, Y. Wang, M.A. Larotonda, B.M. Luther, M.C. Marconi, J.J. Rocca, C.S. Menoni, E.H. Anderson, W. Chao, B.D. Harteneck, J.A. Liddle, Y. Liu, and D.T. Attwood, "Sub-38 nm resolution tabletop microscopy with 13 nm wavelength laser light", *Optics Letters* **31**, 1214, (2006).
6. G. Vaschenko, **F. Brizuela**, C. Brewer, M. Grisham, H. Mancini, C.S. Menoni, M. Marconi, J.J. Rocca, W. Chao, A. Liddle, E. Anderson, D. Attwood, A.V. Vinogradov, I.A. Artioukov, Y.P. Pershyn, and V.V. Kondratenko, "Nano-imaging with a compact extreme ultraviolet laser", *Optics Letters* **30**, 2095, (2005). (This article has been selected for publication in the *Virtual Journal of Nanoscale Science & Technology* 2005.)
7. **F. Brizuela**, G. Vaschenko, C. Brewer, M. Grisham, C.S. Menoni, M. Marconi, J.J. Rocca, W. Chao, A. Liddle, E. Anderson, D. Attwood, A.V. Vinogradov, I.A. Artioukov, Y.P. Pershyn and V.V. Kondratenko, "Reflection mode microscope using a compact extreme ultraviolet laser light source", *Optics Express* **13**, 3983-3989, (2005).

Science news articles

1. C. Brewer, **F. Brizuela**, G. Vaschenko, Y. Wang, M.A. Larotonda, B.M. Luther, M.C. Marconi, J.J. Rocca, C.S. Menoni, E.H. Anderson, W. Chao, Y. Liu, and D.T. Attwood, "Light-Based Microscopy Reaches Sub-38nm Resolution with Extreme UV Laser", *Optics & Photonics News*, "Optics in 2006", **17**, No. 12, 45, (2006).
2. G. Vaschenko, **F. Brizuela**, C. Brewer, M. Grisham, C.S. Menoni, M.C. Marconi, J.J. Rocca, W. Chao, J.A. Liddle, E.H. Anderson, D.T. Attwood, A.V. Vinogradov, I.A. Artioukov, Y.P. Persyn, V.V. Kondratenko, "Nano-Imaging with Compact Extreme Ultraviolet Lasers", "Optics in 2005", **16**, No 12, p. 25, (2005).

Press release articles

- EUV microscope inspects masks on-site
(<http://optics.org/cws/article/research/37914>), March 2009

- “Engineering Professor Wins 'Invention Oscar”, Colorado State University, <http://www.colostate.edu/features/carmen-menoni.aspx>, 2008
- “EUVM-1, Nanoscale resolution 46.9 nm wavelength microscope”, R&D 100 Magazine, 2009
- TECHNOLOGY REVIEW 2006: The exotic and the everyday spur innovation - “Imaging on the edge” Laser Focus World, vol. 42, No. 12, 2006.
- J.R. Minkel, “A Table-top EUV microscope”, IEEE Spectrum, Sept. 2006.
- “38 nm Spatial resolution EUV microscope”, Highlights of CLEO 2006 – AIP- 1 of 6 papers selected for General News Release from ~1700 submissions
- G. Overton, ‘Compact EUV laser enables nanoimaging,’ Laser Focus World, v. 41, p. 32 (2005).
- J.T. Abiade, ‘Nanoscale Features Imaged Using Compact Extreme Ultra-Violet Laser,’ Materials Research Society, Materials Connections (online at http://www.mrs.org/connections/matl_news.html) (2005).
- J. Tyrrell, ‘EUV microscope explores nanoscale,’ in Optics.org (2005).

Conference abstracts or proceedings

1. **F. Brizuela**, S. Carbajo, A. E. Sakdinawat, Y. Wong, D. Alessi, B. M. Luther, W. Chao, Y. Liu, K. A. Goldberg, P. Naulleau, E. H. Anderson, M. C. Marconi, D. T. Attwood, J. J. Rocca, and C. S. Menoni, “Improved performance of a table-top actinic full-field microscope with EUV laser illumination,” Oral, SPIE Advanced Lithography, San Jose, CA, USA (2010)
2. **F. Brizuela**, Y. Wang, C.A. Brewer, F. Pedaci, W. Chao, E. H. Anderson, Y. Liu, K. A. Goldberg, P. Naulleau, P. Wachulak, M. C. Marconi, D. T. Attwood, J. J. Rocca, and C. S. Menoni, “13.2 nm Table-Top Inspection Microscope for Extreme Ultraviolet Lithography Mask Defect Characterization,” Oral, Conference on Lasers and Electro-Optics (CLEO), Conference on Lasers and Electro-Optics (CLEO) (2009) paper: JFA5, Baltimore, MD, USA (2009)
3. **F. Brizuela**; Y. Wang, C. A. Brewer, F. Pedaci, W. Chao, E. H. Anderson, Y. Liu, K. A. Goldberg, P. P. Naulleau, P. W. Wachulak, M. C. Marconi, D. T. Attwood, J. J. Rocca, and C. S. Menoni, “Inspection 13.2-nm table-top full-field microscope,” Poster, SPIE – Alternative Lithographic Techniques, **Proc. SPIE, Vol. 7271, 72713F (2009)**, San Jose, CA, USA (2009)
4. C. Menoni, **F. Brizuela**, et al., “EUV microscopy opens the door to the nanoworld,” Oral (**invited**), Frontiers in Optics, San Jose, CA, USA (2009)

5. C. Menoni, **F. Brizuela**, et al., “Advances in EUV microscopy with table-top lasers,” Oral (**invited**), SPIE Annual Meeting, San Jose, CA, USA (2009)
6. C.S. Menoni, **F. Brizuela**, C. Brewer, Y. Wang, F. Pedacci, B. Luther, M. C. Marconi, J. J. Rocca, W. Chao, E. H. Anderson, K. Goldberg, Y.W. Liu, D. T. Attwood, A. V. Vinogradov, I. A. Artioukov, A. G. Ponomareko, and V. V. Kondratenko, “Nanometer Scale Imaging with Extreme Ultraviolet Lasers,” Oral (**invited**), 39th Progress in Quantum Electronics Symposium, Snowbird, UT, USA (2009)
7. C.S. Menoni, **F. Brizuela**, C. Brewer, Y. Wang, F. Pedacci, B. Luther, M.C. Marconi and J. J. Rocca, W. Chao, E. H. Anderson, K. Goldberg, Y.W. Liu and D. T. Attwood, A. V. Vinogradov and I. A. Artioukov, A.G. Ponomareko and V. V. Kondratenko, “Advances in nanoscale resolution soft x-ray laser microscopy,” Oral (**Invited**), International Conference on Soft X-Ray Lasers, Belfast, Ireland (2008)
8. **F. Brizuela**, C. Brewer, D. Martz, M. C. Marconi, J. J. Rocca, C. S. Menoni, W. Chao, E. H. Anderson, D. T. Attwood, A. V. Vinogradov, I. A. Artioukov, A. G. Ponomareko, and V. V. Kondratenko, “Single-shot Extreme Ultraviolet Microscopy with 54 nm Resolution using a Desktop size Capillary Discharge Laser,” Oral, IEEE Lasers and Electro-Optics Society Annual Meeting, Newport Beach, CA, USA (2008)
9. M. Marconi, P. Wachulak, C. Brewer, **F. Brizuela**, R. Bartels, C. S. Menoni, J. J. Rocca, E. Anderson, and W. Chao, “Analysis of Resolution and Feature Size in Extreme Ultraviolet Microscopy Images,” Oral, IEEE Lasers and Electro-Optics Society Annual Meeting, Newport Beach, CA, USA (2008)
10. **F. Brizuela**, Y. Wang, F. Pedaci, C. A. Brewer, P. Wachulak, W. Chao, Y. Liu, K. Goldberg, P. Naulleau, E. H. Anderson, D. T. Attwood, M. C. Marconi, J. J. Rocca, and C. S. Menoni, “High resolution 13.2 nm reflection microscopy on a table top,” Poster, SPIE Microlithography, Lake Tahoe, NV, USA (2008)
11. C. S. Menoni, **F. Brizuela**, C. Brewer, Y. Wang, D. Alessi, P. Wachulak, B. M. Luther, M. C. Marconi, J. J. Rocca, W. Chao, E. H. Anderson, D. T. Attwood, A. V. Vinogradov, I. A. Artioukov, Y. P. Pershyn, and V. V. Kondratenko, “Full Field Imaging With Extreme Ultraviolet Lasers At Near Wavelength Resolution,” Oral, International Conference on Nonlinear Near Field Optics (NFO-10), Buenos Aires, Argentina (2008)
12. M. C. Marconi, P. W. Wachulak, C. Brewer, **F. Brizuela**, R. Bartels, C. S. Menoni, J. J. Rocca, E. Anderson, and W. Chao, “Resolution and Feature Size Assessments in Soft X ray Microscopy Images,” Oral, 11th International Conference On X-Ray Lasers, Belfast, Ireland (2008)

13. **F. Brizuela**, P. W. Wachulak, C. A. Brewer, C. S. Menoni, W. Chao, E. H. Anderson, R. A. Bartels, J. J. Rocca, and M. C. Marconi, "Simultaneous determination by correlation of feature size and spatial resolution in EUV images of patterned nanostructures," Poster, 9th International Conference on X-Ray Microscopy - XRM2008, J. Phys.: Conf. Ser. **186**, 012026, Zurich, Switzerland (2008)
14. **F. Brizuela**, C. A. Brewer, D. Martz, P. Wachulak, M. C. Marconi, J. J. Rocca, E.H. Anderson, W. L. Chao, D. T. Attwood, I. Artioukov, A. Vinogradov, A. Ponomareko, V. Kondratenko, and C.S. Menoni, "50 nm spatial resolution single shot microscopy with a 46.9 nm laser," Poster, 9th International Conference on X-Ray Microscopy - XRM2008, J. Phys.: Conf. Ser. **186**, 012026, Zurich, Switzerland (2008)
15. C. A. Brewer, **F. Brizuela**, D. Martz, P. Wachulak, M. C. Marconi, J. J. Rocca, and C. S. Menoni, "50 nm Resolution Extreme Ultraviolet Imaging with a Desktop-size Laser," Oral, 52nd International Electron, Ion and Photon Beam Technology and Nanofabrication (EIPBN) Conference, Portland, OR, USA (2008)
16. **F. Brizuela**, C. A. Brewer, D. Martz, M. Marconi, J. J. Rocca, C. S. Menoni, W. Chao, E. H. Anderson, D. T. Attwood, A. Vinogradov, I. Artioukov, A. Ponomareko, and V. Kondratenko, "Near-Wavelength Resolution Extreme Ultraviolet Imaging with a Desktop-Size Laser," Oral, Conference on Lasers and Electro-Optics (CLEO), Conference on Lasers and Electro-Optics (CLEO) 2008 paper: CMCC7, San Jose, CA, USA (2008)
17. M. Marconi, P. Wachulak, C. A. Brewer, **F. Brizuela**, R. Bartels, C. S. Menoni, J. J. Rocca, E. H. Anderson, and W. Chao, "Analysis of Resolution and Feature Size in Extreme Ultraviolet Microscopy Images," Oral, Conference on Lasers and Electro-Optics (CLEO), Conference on Lasers and Electro-Optics (CLEO) (2008) paper: JWA80, San Jose, CA, USA (2008)
18. C. S. Menoni, **F. Brizuela**, C. A. Brewer, G. Vaschenko, M. C. Marconi, J. J. Rocca, W. Chao, E. H. Anderson, D. T. Attwood, A. V. Vinogradov, I. A. Artioukov, Y. P. Pershyn, and V. V. Kondratenko, "70 nm Spatial Resolution Microscope using Desktop-size Extreme Ultraviolet Laser illumination," Oral, Ultrafast Optics-High Fields and Short Wavelength Conference (UFO-HFSW), Santa Fe, NM, USA (2008)
19. C. A. Brewer, **F. Brizuela**, D. H. Martz, M. C. Marconi, J. J. Rocca, C. S. Menoni, W. Chao, E. H. Anderson, D. T. Attwood, A. V. Vinogradov, I. A. Artioukov, Y. P. Pershyn, and V. Kondratenko, "High spatial resolution full-field microscopy using a desktop-size soft x-ray laser," Oral, SPIE - Conference on Soft X-Ray Lasers and Applications VII, Proc.SPIE, Vol.**6702**, 6702M (2007), San Diego, CA, USA (2007)

20. **F. Brizuela**, C. Brewer, G. Vaschenko, Y. Wang, M. Larotonda, B. Luther, M. Marconi, J. Rocca, C. S. Menoni, W. Chao, Y. Liu, E. Anderson, D. Attwood, A. Vinogradov, I. Artioukov, Y. Pershyn, and V. Kondratenko, "Nano-scale resolution full-field microscopy using tabletop extreme ultraviolet lasers," Conference on Lasers and Electro-Optics (CLEO) (2007) paper: CThCC2 (2007)
21. C.S. Menoni, G. Vaschenko, **F. Brizuela**, C. Brewer, Y. Wang, M.A. Larotonda, B.M. Luther, M.C. Marconi, J.J. Rocca, W. Chao, J.A. Liddle, Y. Liu, E.H. Anderson, D.T. Attwood, A.V. Vinogradov, I.A. Artioukov, Y.P. Pershyn and V.V. Kondratenko, "Nano-scale imaging with table-top soft x-ray lasers," Oral (**invited**), 10th International Conference on X-Ray Lasers, Berlin, Germany (2006)
22. C.S. Menoni, G. Vaschenko, **F. Brizuela**, C. Brewer, Y. Wang, M. A. Larotonda, B. M. Luther, M. C. Marconi, J. J. Rocca, W. Chao, J. A. Liddle, Y. Liu, E. H. Anderson, D. T. Attwood, A. V. Vinogradov, I. A. Artioukov, Y. P. Pershyn, and V. V. Kondratenko, "Nano-scale imaging with table-top extreme ultraviolet lasers," Oral, Materials Research Society Symposium, Boston, MA, USA (2006)
23. C. S. Menoni, G. O. Vaschenko, **F. Brizuela**, C. Brewer, Y. Wang, M. A. Larotonda, B. M. Luther, M. C. Marconi, J. J. Rocca, W. Chao, J. Liddle, Y. W. Liu, E. H. Anderson, D. Attwood, A. V. Vinogradov, I. A. Artioukov, Y. P. Pershyn, and V. V. Kondratenko, "Nanometer-scale Resolution Microscopy with Compact Extreme Ultraviolet Lasers," Oral, IEEE LEOS Annual Meeting 2006, 19th Annual Meeting of the IEEE , pp. 895-896, Montreal, Quebec, Canada (2006)
24. J. J. Rocca, Y. Wang, M. Larotonda, B. Luther, D. Alessi, M. Berrill, M. Marconi, G. Vaschenko, C. Brewer, **F. Brizuela**, C. S. Menoni, Y. Liu, W. Chao, E. Anderson, and D. T. Attwood, "Table-Top EUV Lasers for Metrology," Poster, 2006 International Symposium on EUV Lithography, Barcelona, Spain (2006)
25. **F. Brizuela**, C. Brewer, G. Vaschenko, Y. Wang, M. Larotonda, B. Luther, M. C. Marconi, J. J. Rocca, C. S. Menoni, W. Chao, J.A. Liddle, Y. Liu, E. H. Anderson, and D. T. Attwood, "Imaging with Sub-38nm Spatial Resolution Using a Tabletop 13nm Wavelength Laser," Oral, Frontiers in Optics, Laser Science (LS) (2006) paper: JTUB5, Rochester, NY, USA (2006)
26. **F. Brizuela**, H. Bravo, G. Vaschenko, C. S. Menoni, J. J. Rocca, O. Hemberg, B. Frazer, S. Bloom, W. Chao, E. H. Anderson, and D. T. Attwood, "Ablation of Nanometer-Scale Features Using a Table-Top Soft X-ray Laser," Oral, Frontiers in Optics, Frontiers in Optics (FiO) (2006) paper: JSuA21, Rochester, NY, USA (2006)

27. C. Brewer, G. Vaschenko, **F. Brizuela**, Y. Wang, M. A. Larotonda, B. M. Luther, M. C. Marconi, J. J. Rocca, C. S. Menoni, W. Chao, J. A. Liddle, Y. Liu, E. H. Anderson, and D.T. Attwood, "Sub-38 nm resolution microscopy with a tabletop 13 nm wavelength laser," Oral, Conference on Lasers and Electro-Optics (CLEO), Conference on Lasers and Electro-Optics (CLEO) 2006 paper: CME4, Long Beach, CA, USA (2006)
28. A. Artiukov, **F. Brizuela**, G. Vaschenko, C. Brewer, M. Grisham, C. S. Menoni, M. C. Marconi, J. J. Rocca, W. L. Chao, J. A. Liddle, E. Anderson, D. T. Attwood, Yu. P. Pershyn, A. G. Ponomarenko, D. L. Voronov, V. V. Kondratenko, R. M. Fechtchenko, Yu. S. Kasianov, Yu. A. Uspenskii, and A.V. Vinogradov, "Towards laboratory soft x-ray microscopes based on reflective and diffractive optics and compact x-ray sources," Oral, The 8th International Conference on the Physics of X-ray Multiplayer Structures, Sapporo, Japan (2006)
29. G. Vaschenko, **F. Brizuela**, C. Brewer, M. A. Larotonda, Y. Wang, B. M. Luther, M. C. Marconi, C. S. Menoni, J. J. Rocca, W. Chao, E. H. Anderson, Y. Liu, and D. T. Attwood, "EUV imaging with a 13 nm tabletop laser reaches sub-38 nm spatial resolution," Poster, SPIE - Emerging Lithographic Technologies X, Proc. SPIE, Vol. **6151**, 61510X (2006), San Jose, CA, USA (2006)
30. G. Vaschenko, **F. Brizuela**, C. Brewer, M. Grisham, Y. Wang, M. A. Larotonda, B. M. Luther, M. Marconi, C. S. Menoni, J. J. Rocca, W. Chao, J. A. Liddle, E. H. Anderson, D. T. Attwood, Y. P. Pershyn, V. V. Kondratenko, A. V. Vinogradov, and I. A. Artiukov, "Nano-imaging with compact extreme ultraviolet laser sources," Oral, SPIE - Metrology, Inspection, and Process Control for Microlithography XIX, Proc. SPIE 5752, 375 (2005), San Jose, CA, USA (2005)
31. **F. Brizuela**, G. Vaschenko, C. Brewer, M. E. Grisham, C. S. Menoni, H. Mancini, M. C. Marconi, J. J. Rocca, W. Chao, A. Liddle, E. H. Anderson, D. T. Attwood, A. V. Vinogradov, I. A. Artiukov, Y. P. Pershin, and V. V. Kondratenko, "Demonstration of nanometer scale imaging with a compact soft x-ray laser," Oral, Soft X-ray lasers and Applications VI, SPIE Annual Meeting, San Diego, CA, USA (2005)
32. G. Vaschenko, C. Brewer, **F. Brizuela**, Y. Wang, M. A. Larotonda, B. M. Luther, C. S. Menoni, M. Marconi, J. J. Rocca, W. Chao, J. A. Liddle, E. H. Anderson, Y. Liu, and D. T. Attwood, "Sub-40 nm spatial resolution imaging with 13.2 nm wavelength illumination from a table-top laser," Oral, 4th International Extreme Ultraviolet Lithography Symposium, San Diego, CA, USA (2005)
33. **F. Brizuela**, G. O. Vaschenko, C. Brewer, M. Grisham, C. S. Menoni, H. Mancini, M. C. Marconi, J. J. Rocca, W. Chao, A. Liddle, E. H. Anderson, D. T. Attwood, A. V. Vinogradov, I.A. Artiukov, Y. P. Pershyn, and V. V. Kondratenko, "Nanometer-scale imaging with a compact soft x-ray laser," Oral,

SPIE Conference on Soft X-ray lasers and Applications IV, Proc. SPIE, Vol. **5919**, 59190N (2005), San Diego, CA, USA (2005)

34. G. Vaschenko, **F. Brizuela**, C. Brewer, M. Grisham, H. Mancini, C. S. Menoni, M. Marconi, J. J. Rocca, W. Chao, A. Liddle, E. Anderson, D. Attwood, A. V. Vinogradov, I. A. Artioukov, Yu. P. Pershyn, and V. V. Kondratenko, "Nano-scale imaging with a compact EUV laser, Conference on Lasers and Electro-Optics (CLEO) (2005) paper: JThG4, Baltimore, MD, USA (2005)
35. G. Vaschenko, **F. Brizuela**, C. Brewer, M. Grisham, Y. Wang, M. A. Larotonda, B. M. Luther, M. Marconi, C. S. Carmen, J. J. Rocca, W. L. Chao, J. A. Liddle, E. H. Anderson, D. T. Attwood, Y. P. Pershyn, V. V. Kondratenko, A. V. Vinogradov, and I. A. Artioukov, "Nano-imaging with compact extreme ultraviolet laser sources," Poster, SPIE Microlithography, San Jose, CA, USA (2005)

CHAPTER 7: References

1. D. T. Attwood, *Soft x-ray and extreme ultraviolet radiation: principles and applications* (2000).
2. P. Fischer, T. Eimuller, G. Schutz, and G. Denbeaux, "Imaging Magnetic Domain Structures with Soft X-Ray Microscopy," *Structural Chemistry* **14**, 39-47 (2003).
3. M. Berglund, L. Rymell, M. Peuker, T. Wilhein, and H. M. Hertz, "Compact water-window transmission X-ray microscopy," *Journal of Microscopy* **197**, 268-273 (2000).
4. P. A. C. Takman, H. Stollberg, G. A. Johansson, A. Holmberg, M. Lindblom, and H. M. Hertz, "High-resolution compact X-ray microscopy," *Journal of Microscopy* **226**, 175 (2007).
5. O. Mosendz, G. Mihajlovic, J. E. Pearson, P. Fischer, M.-Y. Im, S. D. Bader, and A. Hoffmann, "Imaging of lateral spin valves with soft x-ray microscopy," *Physical Review B* **80**, 104439 (2009).
6. P. Fischer, D.-H. Kim, B. L. Mesler, W. Chao, and E. H. Anderson, "Magnetic soft X-ray microscopy: Imaging spin dynamics at the nanoscale," *Journal of Magnetism and Magnetic Materials* **310**, 2689-2692 (2007).
7. M. C. G. Juenger, V. H. R. Lamour, P. J. M. Monteiro, E. M. Gartner, and G. P. Denbeaux, "Direct observation of cement hydration by soft X-ray transmission microscopy," *Journal of Materials Science Letters* **22**, 1335-1337 (2003).
8. M. A. Le Gros, G. McDermott, and C. A. Larabell, "X-ray tomography of whole cells," *Current Opinion in Structural Biology* **15**, 593-600 (2005).
9. D. Y. Parkinson, G. McDermott, L. D. Etkin, M. A. Le Gros, and C. A. Larabell, "Quantitative 3-D imaging of eukaryotic cells using soft X-ray tomography," *Journal of Structural Biology* **162**, 380-386 (2008).
10. G. McDermott, M. A. Le Gros, C. G. Knoechel, M. Uchida, and C. A. Larabell, "Soft X-ray tomography and cryogenic light microscopy: the cool combination in cellular imaging," *Trends in Cell Biology* **19**, 587-595 (2009).
11. B. Niemann, D. Rudolph, and G. Schmahl, "X-ray microscopy with synchrotron radiation," *Applied Optics* **15**, 1883-1884 (1976).
12. G. Schmahl, D. Rudolph, B. Niemann, and O. Christ, "Zone-plate X-ray microscopy," *Quarterly Reviews of Biophysics* **13**, 297-315 (1980).
13. W. Chao, J. Kim, S. B. Rekawa, P. Fischer, and E. H. Anderson, "Demonstration of 12 nm Resolution Fresnel Zone Plate Lens based Soft X-ray Microscopy," *Optics Express* **17**, 17669-17677 (2009).
14. W. Chao, "Resolution Characterization and Nanofabrication for Soft X-ray Zone Plate Microscopy," (University of California, Berkeley, Berkeley, 2005).

15. C. S. M. Weiland, U. Kleineberg, Th. Westerwalbesloh, U. Heinzmann and T. Wilhein, "Toward time-resolved soft X-ray microscopy using pulsed fs-high - harmonic radiation," *Ultramicroscopy* **102**, 93-100 (2005).
16. X. Z. A. R. Libertun, A. Paul, D. Raymondson, E. Greshgoren, E. Gagnon, S. Backus, M. M. Murnane, H. C. Kapteyn, R. A. Bartles, Y. Liu and D. T. Attwood, "High-resolution EUV imaging using high harmonic generation.," in *Conference on Lasers and Electro-Optics Technical Digest.*, 2004),
17. J. A. T. a. R. L. Byer, "Compact scanning soft x-ray microscope using a laser-produced plasma source and normal-incidence multilayer mirrors," *Optics Letters* **14**, 539-541 (1989).
18. H. H. G. A. Johansson, H. M. Hertz and M. Berglund, "Design and performance of a laser-plasma-based compact soft x-ray microscope," *Review of Scientific Instruments* **73**, 11931197 (2002).
19. J. E. T. L. B. Da Silva, S. Mrowka, T. W. Barbee, Jr., J. Brase, J. A. Koch, R. A. London, B. J. MacGowan, D. L. Matthews, D. Minyard, G. Stone, T. Yorkey, E. Anderson, D. T. Attwood and D. Kern, "Demonstration of x-ray microscopy with an x-ray laser operating near the carbon K edge.," *Optics Letters* **17**, 754-756 (1992).
20. L. R. M. Berglund, M Peuker, T. Wilhein and H. M. Hertz, "Compact water-window transmission X-ray microscopy.," *Journal of Microscopy* **197**, 268-273 (2000).
21. M. T. M. Kishimoto, R. Tai, K. Sukegawa, M. Kado, N. Hasegawa, H. Tang, T. Kawachi, P. Lu, K. Nagashima, H. Daido. Y. Kato, K. Nagai and H. Takenaka, "Developement of soft X-ray microscopy system using X-ray laser in JAERI Kansai," *J. Phys. IV France* **104**, 141-143 (2003).
22. R. F. M. Weiland, T. Wilhein, Ch. Spielmann, M. Pohl and U. Kleineberg, "Submicron extreme ultraviolet imaging using high-harmonic radiation.," *Applied Physics Letters* **81**, 2520-2522 (2002).
23. D. S. Kim, J. J. Park, K. H. Lee, J. Park, and C. H. Nam, "Soft X-ray Microscope Constructed with 130-nm Spatial Resolution Using a High Harmonic X-ray Source," *Japanese Journal of Applied Physics* **48**, 026506 (2009).
24. A. V. V. I. A. Artioukov, V. E. Asadchikov, Yu. S Kas'yanov, R. V. Serov, A. I. Fedorenko, V. V. Kondratenko and S. A. Yulin, "Schwarzschild soft x-ray microscope for imaging of nonradiating objects.," *Optics Letters* **20**, 2451-2453 (1995).
25. O. von Hofsten, M. Bertilson, J. Reinspach, A. Holmberg, H. M. Hertz, and U. Vogt, "Sub-25-nm laboratory x-ray microscopy using a compound Fresnel zone plate," *Optics Letters* **34**, 2631-2633 (2009).
26. Y. Liu, M. Seminario, F. G. Tomasel, C. Chang, J. J. Rocca, and D. T. Attwood, "Achievement of essentially full spatial coherence in a high-average-power soft-x-ray laser," *Physical Review A* **6303**, 033802 (2001).
27. D. K. D. S. DiCicco, R. Rosser and S. Suckewer, "First stage in the developement of a soft x-ray reflection imaging microscope in the Scharzschild configuration using a soft-x-ray laser at 18.2 nm.," *Optics Letters* **17**, 157-159 (1992).
28. X-Ray Optics Tools - Center for X-Ray Optics (CXRO) - Laurence Berkeley National Laboratory (LBNL).

29. C. A. Brewer, F. Brizuela, P. Wachulak, D. H. Martz, W. Chao, E. H. Anderson, D. T. Attwood, A. V. Vinogradov, I. A. Artyukov, A. G. Ponomareko, V. V. Kondratenko, M. C. Marconi, J. J. Rocca, and C. S. Menoni, "Single-shot extreme ultraviolet laser imaging of nanostructures with wavelength resolution," *Optics Letters* **33**, 518-520 (2008).
30. F. Brizuela, G. Vaschenko, C. Brewer, M. Grisham, C. S. Menoni, M. C. Marconi, J. J. Rocca, W. Chao, J. A. Liddle, E. H. Anderson, D. T. Attwood, A. V. Vinogradov, I. A. Artioukov, Y. P. Pershyn, and V. V. Kondratenko, "Reflection mode imaging with nanoscale resolution using a compact extreme ultraviolet laser," *Optics Express* **13**, 3983-3988 (2005).
31. G. Vaschenko, C. Brewer, E. Brizuela, Y. Wang, M. A. Larotonda, B. M. Luther, M. C. Marconi, J. J. Rocca, and C. S. Menoni, "Sub-38 nm resolution tabletop microscopy with 13 nm wavelength laser light," *Optics Letters* **31**, 1214-1216 (2006).
32. G. Vaschenko, F. Brizuela, C. Brewer, M. Grisham, H. Mancini, C. S. Menoni, M. C. Marconi, J. J. Rocca, W. Chao, J. A. Liddle, E. H. Anderson, D. T. Attwood, A. V. Vinogradov, I. A. Artioukov, Y. P. Pershyn, and V. V. Kondratenko, "Nanoimaging with a compact extreme-ultraviolet laser," *Optics Letters* **30**, 2095-2097 (2005).
33. H. H. Hopkins, "On the diffraction theory of optical images," *Proc. Royal Soc. Series A* **217**, 408-432 (1953).
34. J. W. Goodman, *Statistical Optics*, Wiley series in pure and applied optics (John Wiley & Sons, 1985), p. 550.
35. M. Born, E. Wolf, *Principles of Optics* (Cambridge University Press, 1999).
36. K. H. Toh, "Two-Dimensional Images with Effects of Lens Aberrations in Optical Lithography," (University of California, Berkeley, 1988).
37. D. T. Atwood, *Soft x-ray and extreme ultraviolet radiation: principles and applications* (2000).
38. D. T. Attwood, J. M. Heck, W. Meyer-Ilse and H Anderson, "Resolution determination in X-ray microscopy: an analysis of the effects of partial coherence and illumination spectrum.," *Journal of X-Ray Science and Technology* **8**, 95-104 (1998).
39. M. Mansuripur, *Classical Optics and its Applications* (Cambridge University Press, 2002).
40. A. Isoyan, F. Jiang, Y. C. Cheng, F. Cerrina, P. Wachulak, L. Urbanski, J. J. Rocca, C. S. Menoni, and M. C. Marconi, "Talbot lithography: Self-imaging of complex structures," *Journal of Vacuum Science and Technology B* **27**, 2931-2937 (2009).
41. <http://cuervo.eecs.berkeley.edu/>.
42. Semiconductor Industry Association, retrieved www.sia-online.org.
43. International Technology Roadmap for Semiconductors.
44. V. Banine and R. Moors, "Plasma sources for EUV lithography exposure tools," *Journal of Physics D: Applied Physics* **37**, 3207-3212 (2004).
45. V. Bakshi, *EUV Lithography* (SPIE & Wiley-Interscience, 2009).
46. S. Wurm and K. Kemp, "SEMATECH pushes extreme UV lithography forward," SPIE Newsroom, 2006-04-10, 2006.

47. "IMEC, ASML: Another step closer to production-worthy EUV," Solid State Technology, 2008-09-01, 2008.
48. "EUV Litho, Inc. Workshop," (Hawaii, 2009).
49. W. Cho, S.-H. Han, K. A. Goldberg, P. A. Kearney, and C.-U. Jeon, "Detectability and printability of EUVL mask bank defects for the 32 HP node," in *Photomask Technology*, (Proc. of SPIE, 2007), 673013-673011.
50. M. Yi, T. Haga, C. Walton, and J. Bokor, "High sensitivity actinic detection of native defects on extreme ultraviolet lithography mask blanks," *Journal of Vacuum Science and Technology B* **129**, 2401-2405 (2001).
51. I. Mochi, K. A. Goldberg, B. La Fontaine, A. Tchikoulaeva, and C. Holfeld, "Actinic imaging of native and programmed defects on a full-field mask," in (2010), 7636-7645.
52. K. A. Goldberg, A. Barty, P. Seidel, K. Edinger, R. Fettig, P. A. Kearney, H.-S. Han, and O. R. I. Wood, "EUV and non-EUV inspection of reticle defect repair sites," in *Emerging Lithographic Technologies XI, SPIE Advanced Lighthography*, (Proc. SPIE, 2007), 6517-6511.
53. Lasertec.
54. K. A. Goldberg, A. Barty, Y. Liu, P. A. Kearney, Y. Tezuka, T. Terasawa, J. S. Taylor, H.-S. Han, and O. R. I. Wood, "Actinic inspection of extreme ultraviolet programmed multilayer defects and cross-comparison measurements," *Journal of Vacuum Science and Technology B* **24**, 2824-2828 (2006).
55. S. Wurm, H.-S. Han, P. A. Kearney, W. Cho, C.-U. Jeon, and E. M. Gullikson, "EUV mask blank defect inspection strategies for the 32 nm half-pitch and beyond," in *Photomask and Next-Generation Lithography Mask Technology XIV*, (Proc. of SPIE, 2007), 66073A.
56. A. Barty, Y. Liu, E. M. Gullikson, J. S. Taylor, and O. R. I. Wood, "Actinic inspection of multilayer defects on EUV masks," in *Emerging Lithographic Technologies IX*, (Proceedings of SPIE, 2005), 651-659.
57. S. Jeong, M. Idir, Y. Lin, L. Johnson, S. Rekawa, M. Jones, P. Denham, P. Batson, R. Levesque, P. A. Kearney, P.-Y. Yan, E. M. Gullikson, J. H. Underwood, and J. Bokor, "At-wavelength detection of extreme ultraviolet lithography mask blank defects," *J. Vac. Sci. Technol. B* **16**, 3430-3434 (1998).
58. S. Jeong, L. Johnson, S. Rekawa, C. C. Walton, S. T. Prsbrey, E. Tejnil, J. H. Underwood, and J. Bokor, "Actinic detection of sub-100 nm defects on extreme ultraviolet lithography mask blanks," *J. Vac. Sci. Technol. B* **17**, 3009-3013 (1999).
59. M. Park, M. Yi, P. Mirkarimi, C. Larson, and J. Bokor, "Characterization of extreme ultraviolet lithography mask defects by actinic inspection with broadband extreme ultraviolet illumination," *J. Vac. Sci. Technol. B* **20**, 3000-3005 (2002).
60. Y. Tezuka, M. Ito, T. Terasawa, and T. Tomie, "Design and development of a novel actinic insoection tool for EUV multilayer-coated mask blanks," in *Metrology, Inspection and Process Control for Microlithography XVII*, (Proceedings of SPIE, 2003), 866-876.
61. Y. Tezuka, M. Ito, T. Terasawa, and T. Tomie, "Actinic detection of multilayer defects on EUV mask blanks using LPP light source and dark-field imaging," in *Emerging Lighthographic Technologies VIII*, (Proc. SPIE, 2004), 0277-0786X.

62. Y. Tezuka, T. Tanaka, T. Terasawa, and T. Tomie, "Sensitivity-limiting Factors of at-Wavelength Extreme Ultraviolet Lithography Mask Blank Inspection," *Japanese Journal of Applied Physics* **45**, 5359-5372 (2006).
63. T. Haga, H. Kinoshita, K. Hamamoto, S. Takada, N. Kazui, S. Kakunai, H. Tsubakino, and T. Watanabe, "Evaluation of Finished Extreme Ultraviolet Lithography (EUVL) Masks Using a EUV Microscope," *Japanese Journal of Applied Physics* **42**, 3771-3775 (2003).
64. T. Haga, H. Takenaka, and M. Fukuda, "At-wavelength extreme ultraviolet lithography mask inspection using a Mirau interferometric microscope," *J. Vac. Sci. Technol. B* **18**, 2916-2920 (2000).
65. K. Hamamoto, Y. Tanaka, H. Kawashima, S. Y. Lee, N. Hosokawa, N. Sakaya, M. Hosoya, T. Shoki, T. Watanabe, and H. Kinoshita, "Actinic Mask Inspection Using an EUV Microscope - Preparation of a Mirau Interferometer for Phase-Defect Detection -," *Japanese Journal of Applied Physics* **44**, 5474-5478 (2005).
66. K. Hamamoto, Y. Tanaka, S. Y. Lee, N. Hosokawa, N. Sakaya, M. Hosoya, T. Shoki, T. Watanabe, and H. Kinoshita, "Mask defect inspection using an extreme ultraviolet microscope," *J. Vac. Sci. Technol. B* **23**, 2852-2855 (2005).
67. H. Kinoshita, T. Haga, K. Hamamoto, S. Takada, N. Kazui, S. Kakunai, H. Tsubakino, T. Shoki, M. Endo, and T. Watanabe, "Actinic mask metrology for extreme ultraviolet lithography," *J. Vac. Sci. Technol. B* **22**, 264-267 (2004).
68. H. Kinoshita, K. Hamamoto, N. Sakaya, M. Hosoya, and T. Watanabe, "Aerial Image Mask Inspection System for Extreme Ultraviolet Lithography," *Japanese Journal of Applied Physics* **46**, 6113-6117 (2007).
69. M. Osugi, K. Takana, N. Sakaya, K. Hamamoto, T. Watanabe, and H. Kinoshita, "Resolution Enhancement of Extreme Ultraviolet Microscope Using an Extreme Ultraviolet Beam Splitter," *Japanese Journal of Applied Physics* **47**, 4872-4977 (2008).
70. A. Barty, J. S. Taylor, R. Hudima, E. Spiller, D. W. Sweeney, G. Shelden, and J.-P. Urbach, "Aerial Image Microscopes for the inspection of defects in EUV masks," in *22nd Annual BACUS Symposium on Photomask Technology*, (proceedings of SPIE, 2002), 0277-0786X/0202.
71. K. A. Goldberg, P. P. Naulleau, A. Barty, S. B. Rekawa, C. D. Kemp, R. F. Gunion, F. Salmassi, E. M. Gullikson, E. H. Anderson, and H.-S. Han, "Performance of actinic EUVL mask imaging using a zoneplate microscope," in *Photomask Technology 2007*, (Proc. of SPIE, 2007), 67305E.
72. P. P. Naulleau, "Relevance of mask-roughness-induced printed line-edge roughness in recent and future extreme-ultraviolet lithography tests," *Applied Optics* **43**, 4025-4032 (2004).
73. P. P. Naulleau, "Correlation method for the measure of mask-induced line-edge roughness in extreme ultraviolet lithography," *Applied Optics* **48**, 3302-3307 (2009).
74. H. Feldmann, J. Ruoff, W. Harnisch, and W. Kaiser, "Actinic Review of EUV Masks," in *SPIE Advanced Lithography*, 2010).
75. Y. Wang, M. A. Larotonda, B. M. Luther, D. Alessi, M. Berrill, V. N. Shyaptsev, and J. J. Rocca, "Demonstration of high-repetition-rate tabletop soft-x-ray lasers

- with saturated output at wavelengths down to 13.9 nm and gain down to 10.9 nm," *Physical Review A* **72**(2005).
76. Y. Wang, M. A. Larotonda, B. M. Luther, D. Alessi, M. Berrill, V. N. Shlyaptsev, and J. J. Rocca, "Demonstration of high-repetition-rate tabletop soft-x-ray lasers with saturated output at wavelengths down to 13.9 nm and gain down to 10.9 nm," *Physical Review A* **72**(2005).
 77. J. J. Rocca, Y. Wang, M. A. Larotonda, B. M. Luther, M. Berrill, and D. Alessi, "Saturated 13.2 nm high-repetition-rate laser in nickellike cadmium," *Optics Letters* **30**, 2581-2583 (2005).
 78. Y. Liu, Y. Wang, M. A. Larotonda, B. M. Luther, J. J. Rocca, and D. T. Attwood, "Spatial coherence measurements of a 13.2 transient nickel-like cadmium soft x-ray laser pumped at grazing incidence," *Optics Express* **14**, 12872-12879 (2006).
 79. D. Martz, D. Alessi, B. M. Luther, Y. Wang, D. Kemp, M. Berrill, and J. J. Rocca, "High Energy 13.9 nm Table-top Soft X-ray Laser at 2.5 Hz Repetition Rate Excited by a Slab-pumped Ti:sapphire Laser.," *Optics Letters* **35**, 1632-1634 (2010).
 80. J. M. Heck, D. T. Attwood, W. Meyer-Ilse, and E. Anderson, "Resolution determination in X-ray microscopy: an analysis of the effects of partial coherence and illumination spectrum," *Journal of X-Ray Science and Technology* **8**, 95-104 (1998).
 81. Y. A. Uspenskii, V. E. Levashov, A. V. Vinogradov, A. I. Fedorenko, V. V. Kondratenko, Y. P. Pershin, E. N. Zubarev, and V. Y. Fedotov, "High-reflectivity multilayer mirrors for a vacuum-ultraviolet interval of 35-50 nm," *Optics Letters* **23**, 771-773 (1998).
 82. S. Bajt, D. G. Stearns, and P. A. Kearney, "Investigation of the amorphous-to-crystalline transition in Mo/Si multilayers," *Journal of Applied Physics* **90**, 1017-1025 (2001).
 83. K. N. Kaiser, S. Yulin, and T. Feigl, "Si-based multilayers with high thermal stability.," in *Soft X-Ray and EUV Imaging Systems, SPIE*, 2000), 91-100.
 84. R. Soufli, M. J. Pivovarov, S. L. Baker, J. C. Robinson, E. M. Gullikson, T. J. McCarville, P. M. Stefan, A. L. Aquila, J. Ayers, M. A. McKernan, and R. M. Bionta, "Development, characterization and experimental performance of x-ray optics for the LCLS free-electron laser," in *3rd Conference on Advances in X-ray/EUV Optics and Components*, 2008), 7716-7716.
 85. D. L. Voronov, E. N. Zubarev, V. V. Kondratenko, A. V. Penkov, Y. P. Pershin, A. G. Ponomarenko, I. A. Artioukov, A. V. Vinogradov, Y. A. Uspenskii, and J. F. Seely, "Termoresistive multilayer mirrors with antidiffusion barriers for work at the wavelengths 40-50 nm," in *8th International Conference on X-Ray Lasers*, 2002),
 86. A. E. Yakshin, E. Louis, P. C. Gorts, E. L. G. Maas, and F. Bijkerk, "Determination of the layered structure on Mo/Si multilayers by grazing incidence X-ray reflectometry," *Physica B* **283**, 143-148 (2000).
 87. P. W. Wachulak, C. A. Brewer, F. Brizuela, C. S. Menoni, W. Chao, E. H. Anderson, R. A. Bartels, J. J. Rocca, and M. C. Marconi, "Analysis of extreme ultraviolet microscopy images of patterned nanostructures based on a correlation method," *Journal of the Optical Society of America B* **25**, B20-B26 (2008).

88. P. P. Naulleau, C. N. Anderson, J. Chiu, P. Denham, S. George, K. A. Goldberg, M. Goldstain, B. Hoef, R. Hudyma, G. Jones, C. Koh, B. La Fontaine, A. Ma, W. Montgomery, D. Niakoula, J.-o. Park, T. Wallow, and S. Wurm, "22-nm Half-pitch extreme ultraviolet node development at the SEMATECH Berkeley microfield exposure tool," *Microelectronics Engineering* **86**, 448-455 (2009).
89. SPLAT <http://cuervo2.eecs.berkeley.edu/>.
90. K. A. Goldberg, I. Mochi, P. P. Naulleau, H.-S. Han, and S. Huh, "Benchmarking EUV mask inspection beyond 0.25 NA," in *Photomask Technology 2008*, (Proc. of SPIE, 2008), 71222E-71221.
91. K. Jefimovs, J. Vila-Comamala, M. Stampanoni, B. Kaulich, and C. David, "Beam-shaping condenser lenses for full-field transmission X-ray microscopy," *Journal of Synchrotron Radiation* **15**, 106-108 (2008).
92. U. Vogt, M. Lindblom, P. Charalambous, B. Kaulich, and T. Wilhein, "Condenser for Koehler-like illumination in transmission x-ray microscopes at undulator sources," *Optics Letters* **31**, 1465-1467 (2006).
93. J. Kirz, "Phase zone plates for x rays and extreme uv," *Journal of the optical Society of America* **64**, 301-309 (1973).